РОССИЙСКИЙ ГОСУДАРСТВЕННЫЙ ПЕДАГОГИЧЕСКИЙ УНИВЕРСИТЕТ им. А. И. ГЕРЦЕНА
HERZEN STATE PEDAGOGICAL UNIVERSITY of RUSSIA

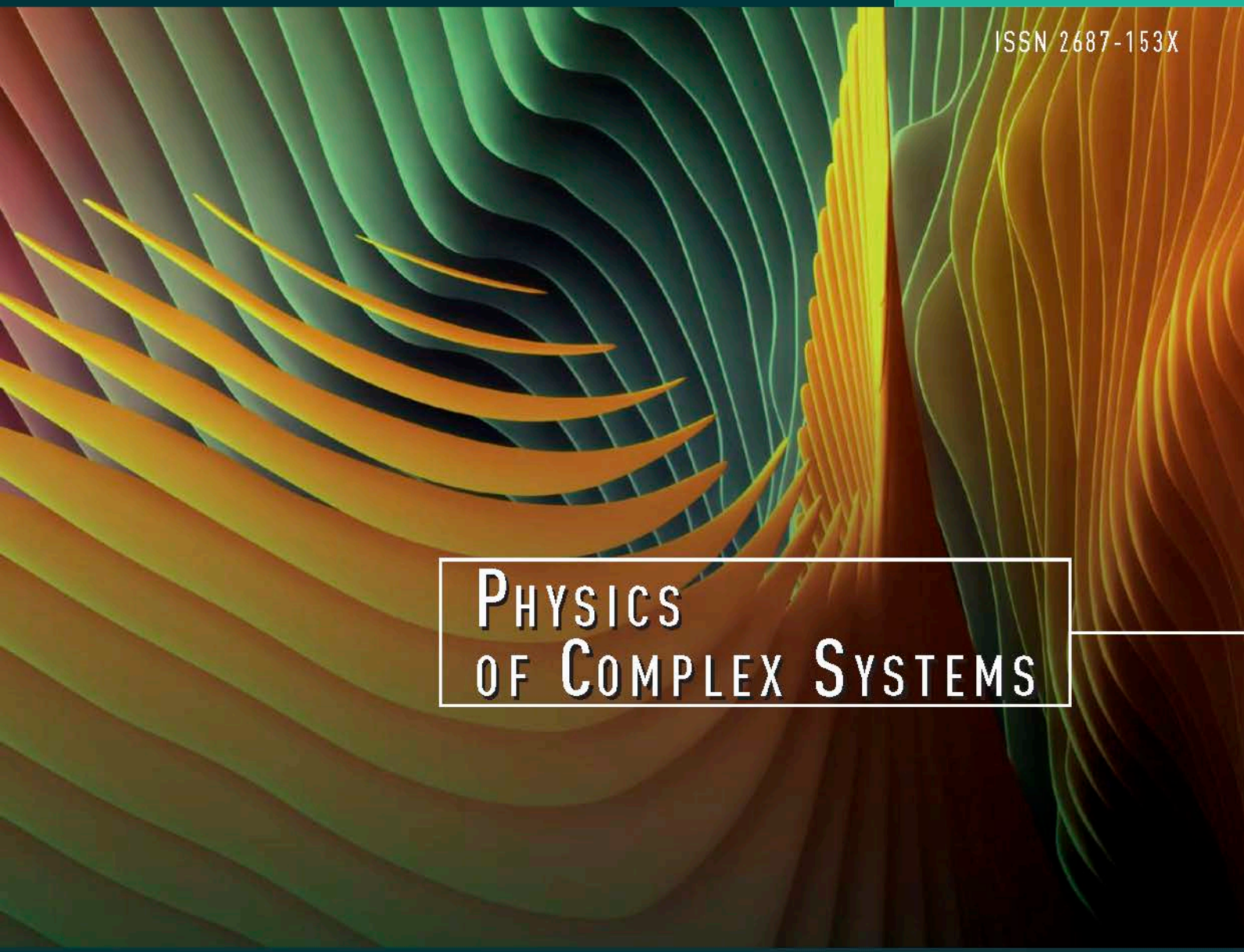

ISSN 2687-153X

Physics of Complex Systems

Т. 6 № 2 2025

Vol. 6 No. 2 2025

Herzen State Pedagogical University of Russia

ISSN 2687-153X (online)
physcomsys.ru
https://www.doi.org/10.33910/2687-153X-2025-6-2
2025. Vol. 6, no. 2

PHYSICS OF COMPLEX SYSTEMS

Mass Media Registration Certificate El No. FS77-77889, issued by Roskomnadzor on 10 February 2020
Peer-reviewed journal
Open Access
Published since 2020
4 issues per year

Publishing house of Herzen State Pedagogical University of Russia
48 Moika Emb., Saint Petersburg 191186, Russia
E-mail: izdat@herzen.spb.ru
Phone: +7 (812) 312-17-41

Data size 10,7 Mbyte
Published at 23.06.2025

Editors of the English text *I. A. Nagovitsyna, K. Yu. Rybachuk*
Corrector *M. L. Kurakina*
Cover design by *O. V. Rudneva*
Layout by *D. V. Romanova*

Saint Petersburg, 2025

CONTENTS

Condensed Matter Physics.
Electronic structure of solids

UDC 538.935

EDN VPUHLM
https://www.doi.org/10.33910/2687-153X-2025-6-2-59-68

Calcium effect on the Nernst coefficient in double-substituted $Y_{1-x}Ca_xBa_2Cu_{2.8}Zn_{0.2}O_y$

Zh. Xunpeng [1], V. E. Gasumyants ✉[1, 2]

[1] Peter the Great St. Petersburg Polytechnic University, 29 Polytechnicheskaya Str., Saint Petersburg 195251, Russia
[2] Herzen State Pedagogical University of Russia, 48 Moika Emb., Saint Petersburg 191186, Russia

Authors

Zhang Xunpeng, ORCID: 0009-0009-7721-5425, e-mail: zhangxunpeng@yandex.com

Vitaliy E. Gasumyants, ORCID: 0000-0002-5306-6738, e-mail: vgasum@yandex.ru

For citation: Xunpeng, Zh., Gasumyants, V. E. (2025) Calcium effect on the Nernst coefficient in double-substituted $Y_{1-x}Ca_xBa_2Cu_{2.8}Zn_{0.2}O_y$. *Physics of Complex Systems*, 6 (2), 59–68. https://www.doi.org/10.33910/2687-153X-2025-6-2-59-68 EDN VPUHLM

Received 28 January 2025; reviewed 7 March 2025; accepted 12 March 2025.

Funding: The study did not receive any external funding.

Abstract. We present experimental results on the temperature dependence of the Nernst coefficient in the normal state of the system $Y_{1-x}Ca_xBa_2Cu_{2.8}Zn_{0.2}O_y$, analyzed quantitatively using a narrow-band model jointly with temperature dependences of the thermopower. From this analysis, we determine the charge carrier mobility across all studied samples and then analyze its variation with increasing calcium content. It is shown that all experimental and calculated results can be explained if we take into account that both calcium and zinc directly affect the structure of the band responsible for the conduction process in the $YBa_2Cu_3O_y$ system. Calcium introduced into the lattice compensates for local disturbances in the electronic structure created by zinc, as a result of which the values of all parameters of the normal state at $x \geq 0.125$ become close to the ones characteristic of undoped $YBa_2Cu_3O_y$.

Keywords: Y-based HTSC, doping, Nernst coefficient, narrow-band model, energy spectrum, charge carrier mobility

Introduction

The unique properties of high-temperature superconductors (HTSCs) have been a major focus of experimental and theoretical research since their discovery in 1987. However, despite extensive studies, the mechanism of electron pairing responsible for the superconductivity phenomenon in these materials remains unclear.

The physics of HTSCs encompasses numerous aspects, many of each offering insights into the unique properties of these materials. In our opinion, the transport properties of HTSC are of undoubted interest for research. As is known, the transport coefficients in the normal state of HTSC exhibit very unusual behavior compared to conventional materials (Gasumyants 2001; Iye 1992; Kaiser, Ucher 1991; Ong 1990), which reflect the unconventional energy spectrum of charge carriers. Although a complete theory of high-temperature superconductivity is still lacking, it is evident that the normal-state parameters of the charge carrier system influence the critical temperature (T_c). For this reason, the information on the nature and the parameters of the normal state is needed for developing the theory that can explain this phenomenon. Such an information can be obtained by studying and analyzing the transport coefficients. The reliable data on the structure of the energy spectrum and the changes in its parameters

under varied sample composition should help to better understand the nature of the normal state in HTSC. Moreover, identifying correlations between the values of these parameters and T_c could indirectly help to verify theoretical models aiming to explain the mechanism of electron pairing in HTSC. This requires determining fundamental HTSC parameters, such as the energy parameters of the band responsible for the conduction process; the charge carrier concentration, mobility, and effective mass, as well as obtaining general knowledge about the peculiarities of the energy spectrum structure in these materials and its transformation when varying the composition of the samples. However, there are not many works devoted to this topic among the numerous studies of HTSC. The most likely reason for this situation is the lack of a holistic approach, which should include not only experimental studies of various transport coefficients for samples of different HTSC systems and various compositions, but also their quantitative analysis within the framework of a unified model, which makes it possible to explain the entire set of experimental data. To substantiate the validity of such a model, it is necessary to carry out systematic studies and analysis of the behavior of transport coefficients in HTSC samples with different types and levels of doping. At the same time, it is important that the model used for such an analysis contains a limited number of physically reasonable parameters and allows one not only to describe the behavior of all the main transport coefficients in HTSC, but also to reliably determine the values of these parameters for samples of different compositions.

In our earlier work, we proposed a phenomenological narrow-band model (Gasumyants et al. 1995) that has since been successfully applied to analyze the thermopower, *S*, in different HTSCs (Gasumyants 2001; Gasumyants, Martynova 2012; Gasumyants et al. 1995; Elizarova, Gasumyants 2000; Martynova, Gasumyants 2013). This approach enabled us to identify the main characteristics of the energy spectrum in HTSCs, as well as a character and mechanisms of its modification under doping. Subsequent studies (Ageev, Gasumyants 2001; Gasumyants et al. 2005) expanded the model's applicability, demonstrating the possibility of its use for quantitative analysis of temperature dependences of the Nernst coefficient, *Q*. Unlike other transport coefficients, the Nernst coefficient has received far less attention in HTSCs. Moreover, while numerous studies have examined *Q* in the vortex phase (e. g., Calzona et al. 1995; Huebener et al. 1991; Qussena et al. 1992), its normal-state behavior remains understudied. A few exceptions explore $Q(T)$ dependences in a narrow temperature range above T_c, where anomalously high values in underdoped cuprates suggest the possible formation of electron pairs at $T > T_c$ (Alexandrov, Zavaritsky 2004; Capan et al. 2002; Tan, Levin 2004; Wang et al. 2001; Xu et al. 2000).

The scarcity of data on Nernst coefficient temperature dependence $Q(T)$ at temperatures well above T_c primarily stems from the lack of suitable analytical methods for studying this behavior in a wide temperature range. Our narrow-band model effectively addresses this challenge. Importantly, this approach enables simultaneous description of four main transport coefficients — resistivity, thermopower, Hall coefficient, and Nernst coefficient (Ageev, Gasumyants 2001; Gasumyants, Martynova 2012). It also allows for joint quantitative analysis of both $S(T)$ and $Q(T)$ dependences (Ageev, Gasumyants 2001; Gasumyants et al. 2005). As shown in (Gasumyants et al. 2005; Gasumyants, Martynova 2018), this methodology additionally provides determination of real charge carrier mobility values.

To study the nature of the normal state, it is necessary to use doped samples with sequentially changing composition and analyze the changes in the found values of model parameters depending on the type and content of the introduced impurity. While numerous cations can substitute into the $YBa_2Cu_3O_y$ lattice (Felner 1991), most impurities exhibit qualitatively similar effects on both superconducting and normal-state transport properties. The most interesting impurity for research in the case of the $YBa_2Cu_3O_y$ system is undoubtedly calcium. Calcium doping produces unusual modifications to transport coefficient temperature dependences and can also enhance superconducting properties if they were previously suppressed by other impurities or oxygen deficiency (Awana et al. 1996; Gasumyants et al. 1994; 2000; Gasumyants, Martynova 2017; Martynova et al. 2011; Suard et al. 1992). In systems like $Y_{1-x}Ca_xBa_2Cu_{2.75}Co_{0.25}O_y$ and $Y_{1-x}Ca_xBa_{1.5}La_{0.5}Cu_3O_y$, the observed T_c enhancement under calcium doping appears linked to its influence on the oxygen subsystem and consequent modifications to the energy spectrum (Gasumyants et al. 1994; 2000; Gasumyants, Martynova 2017). Higher-valence impurities (Co or La) increase oxygen content causing the conductive band broadening, while subsequent calcium doping restores near-stoichiometric oxygen levels, improving subsystem ordering. This influence the energy spectrum parameters in the opposite direction, bringing them closer to those of undoped $YBa_2Cu_3O_y$ and consequently increasing T_c. Interestingly, calcium doping in $Y_{1-x}Ca_xBa_2Cu_{2.8}Zn_{0.2}O_y$ also elevates T_c (Martynova et al. 2011), despite zinc being an isovalent impurity that neither affects oxygen content and suppresses T_c through pair-breaking effect (Bonn et al. 1994; Wang et al. 1998).

 https://www.doi.org/10.33910/2687-153X-2025-6-2-59-68

Zinc does, however, also modify the normal-state energy spectrum (Gupta, Gupta 1999; Martin, Gasumyants 2021). This circumstance makes the $Y_{1-x}Ca_xBa_2Cu_{2.8}Zn_{0.2}O_y$ system particularly compelling for detailed investigation of calcium's role.

Motivated by these considerations, we present the results of a systematic study of the normal-state Nernst coefficient in the double-substituted $Y_{1-x}Ca_xBa_2Cu_{2.8}Zn_{0.2}O_y$ system across varying calcium concentrations, as well as their quantitative analysis within the narrow-band model framework using previously obtained data for the thermopower behavior in the same samples.

Samples and experimental details

Single-phase ceramic samples of $Y_{1-x}Ca_xBa_2Cu_{2.8}Zn_{0.2}O_y$ (x = 0.05, 0.1, 0.125, 0.15, 0.175, and 0.2) were synthesized via standard solid-state reaction using high-purity oxide and carbonate precursors. Previous studies (Gasumyants 2001; Gasumyants, Martynova 2017; Martynova et al. 2011) show that oxygen-rich calcium- and zinc-doped samples exhibit transport coefficients with extremely small absolute values, making accurate analysis of their temperature dependences within our model framework challenging. To address this, we performed controlled oxygen reduction through additional vacuum annealing at 460 °C for 2 hours. The temperature-dependent resistivity and thermopower data for these samples, along with their thermopower analysis, have been previously reported (Martynova et al. 2011). These datasets will be incorporated in our current analysis and discussion of the Nernst coefficient results. To confirm sample stability over time, we re-measured the thermopower temperature dependences $S(T)$ for two representative samples, obtaining excellent agreement with earlier measurements.

The Nernst coefficient measurements were performed under a constant reversible magnetic field of B = 1.8 T. For each temperature, the Nernst signal was measured twice in opposite magnetic field directions and then calculated as the half-difference of the corresponding voltages. This approach effectively eliminates even magnetic effects and significantly improves measurement precision. To increase the signal-to-noise ratio, the sample geometry was optimized to be long (about l = 10 mm) in the Nernst signal, U, direction, and thin (about d = 1 mm) in the temperature gradient direction. The temperature difference applied to the samples was about ΔT = 10 K. Our measurement protocol was validated through extensive test measurements confirming the linear response regime for HTSCs. The Nernst signal (U) maintains linear dependence on temperature gradient (ΔT) up to ΔT = 30–35 K, as established in (Gasumyants, Martynova 2018). The Nernst coefficient values were calculated as $Q = U{\cdot}d/B{\cdot}\Delta T{\cdot}l$. The temperature range of measurements was from 100 K to 320 K.

Experimental results

Figure 1 presents the temperature dependences of the Nernst coefficient $Q(T)$ for the investigated samples, excluding the x = 0.05 and x = 0.15 compositions, the results for which are very close to other experimental curves. As for other doped samples of the $YBa_2Cu_3O_y$ (Gasumyants et al. 2005; Gasumyants, Martynova 2018), the Nernst coefficient has very small values and shows typical changes with temperature. The Nernst coefficient is extremely small near T = 100 K, increases sharply with increasing temperature, reaching maximum values in the normal state, and then decreases slightly at temperatures above T > 150–200 K (with the exact transition temperature varying by composition). This conventional behavior shows notable deviations in samples with lower calcium content (x =0.05–0.125), where the Q values exhibit a pronounced decrease at elevated temperatures beyond the maximum point, as clearly illustrated by the x = 0.1 data in Figure 1. This anomalous effect displays a strong calcium concentration dependence, appearing most distinctly in the sample with lowest calcium content and progressively diminishing with its increase until it vanishes completely at calcium content of $x \geq 0.15$.

Figure 2 displays the room-temperature Nernst coefficient ($Q_{300\,K}$) as a function of calcium content, compared with corresponding thermopower values ($S_{300\,K}$) from previous work (Martynova et al. 2011). While most substitutions in $YBa_2Cu_3O_y$ yield qualitatively similar changes in all transport coefficients (Gasumyants, Martynova 2018), the $Y_{1-x}Ca_xBa_2Cu_{2.8}Zn_{0.2}O_y$ system exhibits distinct behavior. The thermopower shows a consistent monotonic decrease with increasing x, whereas the Nernst coefficient displays a more complex dependence: $Q_{300\,K}$ decreases for x = 0–0.125, but rises at higher calcium concentrations. This contrasts with the monotonic $Q_{300\,K}$ variation observed in the case of single calcium doping (Gasumyants, Martynova 2018).

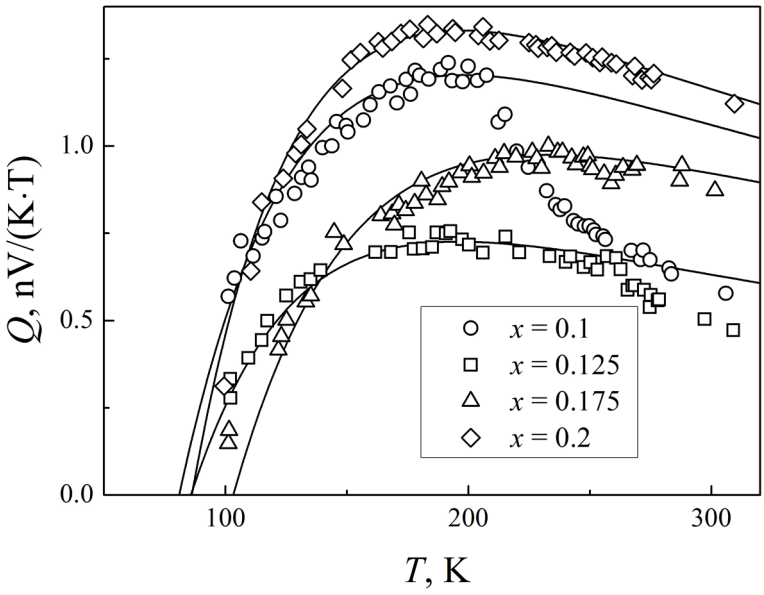

Fig. 1. Temperature dependences of the Nernst coefficient in $Y_{1-x}Ca_xBa_2Cu_{2.8}Zn_{0.2}O_y$.
Symbols indicate experimental resuls; lines indicate the results of calculation within the narrow-band model

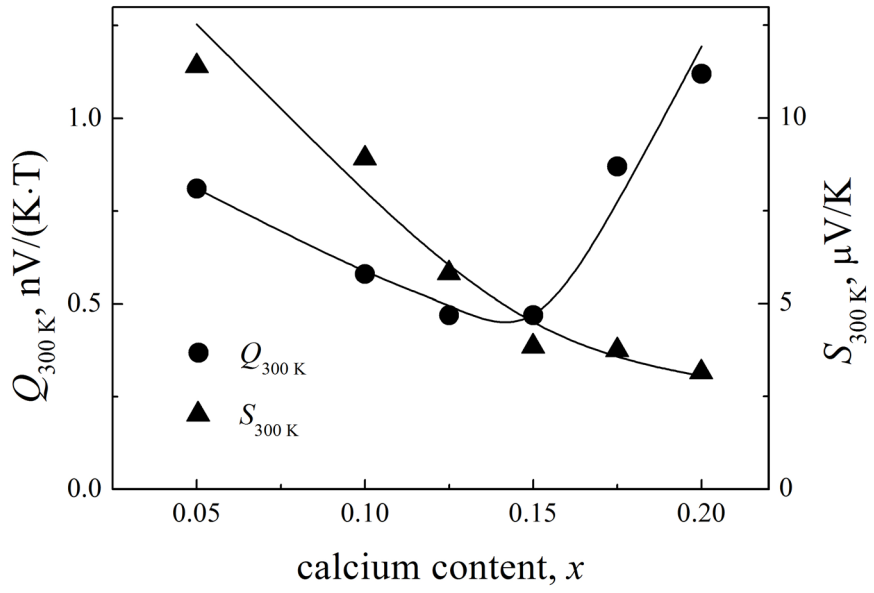

Fig. 2. Room-temperature Nernst coefficient and thermopower in $Y_{1-x}Ca_xBa_2Cu_{2.8}Zn_{0.2}O_y$

The observed evolution of $Q(T)$ behavior with increasing calcium content in $Y_{1-x}Ca_xBa_2Cu_{2.8}Zn_{0.2}O_y$ likely stems from the influences of zinc and calcium on the conduction band structure. Zinc substitutes for plane copper, which participates directly in conduction band formation, and according to the results presented in (Gupta, Gupta 1999), removes electronic states from this band destroying its structure, as confirmed by our thermopower analysis in $YBa_2Cu_{3-x}Zn_xO_y$ (Martin, Gasumyants 2021). This substitution also significantly perturbs the system's electronic structure (Gupta, Gupta 1999), particularly affecting charge carrier scattering. The Nernst coefficient's enhanced sensitivity to scattering processes explains why the $YBa_2Cu_{3-x}Zn_xO_y$ system with substantial zinc content maintains conventional $S(T)$ behavior while developing anomalous features in $Q(T)$, as observed in our measurements. Conversely, calcium doping introduces additional states into the conduction band (Gasumyants, Martynova 2017), effectively counteracting zinc-induced modifications in the $Y_{1-x}Ca_xBa_2Cu_{2.8}Zn_{0.2}O_y$ system. This compensation mechanism accounts for the monotonic decrease in $S_{300\ K}$ with increasing x (Fig. 2) and the systematic evolution

 https://www.doi.org/10.33910/2687-153X-2025-6-2-59-68

of energy spectrum parameters, the values of which at calcium content $x \geq 0.15$ approach those characteristic of undoped $YBa_2Cu_3O_y$ as revealed by our $S(T)$ analysis (Martynova et al. 2011).

Contrary to the thermopower, the Nernst coefficient behavior is affected by disruptions of the electronic structure induced by zinc. At low calcium contents in the $Y_{1-x}Ca_xBa_2Cu_{2.8}Zn_{0.2}O_y$ system ($x < 0.15$), it gradually compensates for the effect of zinc on the energy spectrum structure. This results in a drop in the $Q_{300\,K}$ value and a decrease in the degree of deviation of the $Q(T)$ dependences from the typical form. This compensation becomes nearly complete at $x \geq 0.15$. As a result, the $Q(T)$ dependences take on a typical form, and the $Q_{300\,K}$ value increases with increasing x, as in the case of single calcium doping in the $YBa_2Cu_3O_y$ system.

Note that our conclusion regarding calcium's compensating effect on zinc-induced modifications in the normal-state energy spectrum in $YBa_2Cu_3O_y$ is further supported by recent studies of the $Y_{1-x}Ca_xBa_2Cu_{3-x}Zn_xO_y$ system with equal content of two dopants (Funtikova, Gasumyants 2023), which revealed very slight changes in the energy spectrum parameters over a wide range of doping levels. Thus, it is the compensating effect of calcium that causes the modification of the $Q(T)$ dependences described above, as well as the observed $Q_{300\,K}(x)$ dependence in the $Y_{1-x}Ca_xBa_2Cu_{2.8}Zn_{0.2}O_y$ system.

Analysis of experimental results within the narrow-band model and discussion

Our analysis is based on a narrow-band model that assumes the band responsible for the conduction process in HTSCs has a half-width comparable in order of magnitude to the Fermi smearing, with the Fermi level located within this band. Under these conditions, we can approximate density-of-states, $D(E)$, conductivity, $\sigma(E)$, and Hall conductivity, $\sigma_H(E)$, functions by rectangles of different widths (Gasumyants 2001; Gasumyants et al. 1995). This simplification allows us to derive analytical expressions for the thermopower and Nernst coefficient by solving the Boltzmann transport equation within the relaxation time approximation (Ageev, Gasumyants 2001; Gasumyants et al. 1995):

$$S = -\frac{k_B}{e}\left\{\frac{W_\sigma^*}{\sinh W_\sigma^*}\left[\exp(-\mu^*) + \cosh W_\sigma^* - \frac{1}{W_\sigma^*}(\cosh\mu^* + \cosh W_\sigma^*) \times \right.\right.$$
$$\left.\left. \times \ln\frac{\exp(\mu^*) + \exp(W_\sigma^*)}{\exp(\mu^*) + \exp(-W_\sigma^*)}\right] - \mu^*\right\}, \quad (1)$$

$$Q = \frac{1}{eT}u\left(\frac{I_{H_1}}{I_0} - \frac{I_{H_0}I_1}{I_0^2}\right), \quad (2)$$

where

$$I_i = \int_{-W_\sigma/2+bW_D}^{W_\sigma/2+bW_D}\left(-\frac{\partial f_0}{\partial E}\right)E^i dE, \quad I_{H_i} = \int_{-W_\sigma/2+kW_D}^{W_\sigma/2+kW_D}\left(-\frac{\partial f_0}{\partial E}\right)\mathrm{sign}(E - kW_D)E^i dE,$$

k_B is the Boltzmann constant, e is the elementary charge, f_0 is the equilibrium Fermi-Dirac distribution function, $\mu^* \equiv \mu/k_BT = \ln\frac{\sinh(FW_D^*)}{\sinh[(1-F)W_D^*)]} - 2bW_D^*$, $W_\sigma^* \equiv W_\sigma/2k_BT$, $W_D^* \equiv W_D/2k_BT$, μ is the electrochemical potential measured from the middle of the band. As is seen, the $S(T)$ dependence is determined by four physically significant model parameters, namely, the degree of band filling with electrons F, representing the ratio of the total number of electrons to the total number of states in the band; the total effective bandwidth W_D; the effective width of the delocalized state interval W_σ; and the band asymmetry degree b. The latter three parameters are introduced into the model as describing the approximations we use. The W_D and W_σ values are the widths of rectangles approximating the functions $D(E)$ or $\sigma(E)$ and $\sigma_H(E)$, respectively, as a result their ratio $C \equiv W_\sigma/W_D$ characterizes the degree of delocalization of charge carriers at the band edges. The b value determines the energy shift bW_D between the centers of these rectangles, which arises due to the possible asymmetry of the density-of-state function.

The calculation of the Nernst coefficient's temperature dependence $Q(T)$ requires the introduction of two additional parameters. They are the band-averaged electron mobility u, and the dispersion law asymmetry parameter k, which determines the energy shift kW_D of the sign-change point in the Hall conductivity $\sigma_H(E)$ function relative to the band center. Since Eq. (2) shows that $Q(T)$ depends

collectively on all six model parameters, its independent analysis is not feasible. To apply the described approach, it is necessary to measure both the $S(T)$ and $Q(T)$ dependences on the same samples and then analyze them together. In such a case, the four primary parameters are first determined through thermopower analysis using Eq. (1). These values are then used in Eq. (2) to extract the two remaining parameters from Nernst coefficient analysis (Ageev, Gasumyants 2001; Gasumyants et al. 2005). As demonstrated in previous studies (Gasumyants et al. 2005; Gasumyants, Martynova 2018), this joint analysis of thermopower and Nernst coefficient data enables unambiguous determination of all model parameters in doped $YBa_2Cu_3O_y$ systems.

Figure 3 presents the experimental thermopower data $S(T)$ for the $Y_{1-x}Ca_xBa_2Cu_{2.8}Zn_{0.2}O_y$ system (Martynova et al. 2011), along with best-fitted curves calculated using Eq. (1). The corresponding calculated $Q(T)$ dependences from Eq. (2) are shown in Figure 1. One can see that the narrow-band model allows us to well describe the temperature dependences of both transport coefficients using a single set of model parameters. Two aspects of the fitting procedure deserve mention. First, for samples with low calcium content, we restricted the $Q(T)$ fitting to the low-temperature regime, intentionally excluding the high-temperature region where zinc-induced perturbations of the electronic structure cause anomalous suppression of the Nernst coefficient (as discussed previously). Second, since in the case of an asymmetric band we need to use four parameters to calculate the $S(T)$ dependence, their values can be determined with some errors. The simultaneous fitting of both $S(T)$ and $Q(T)$ data not only determines the u and k parameters, but also enables refinement of the initial parameter estimates, yielding optimal agreement between the experimental and calculated curves for the two studied coefficients.

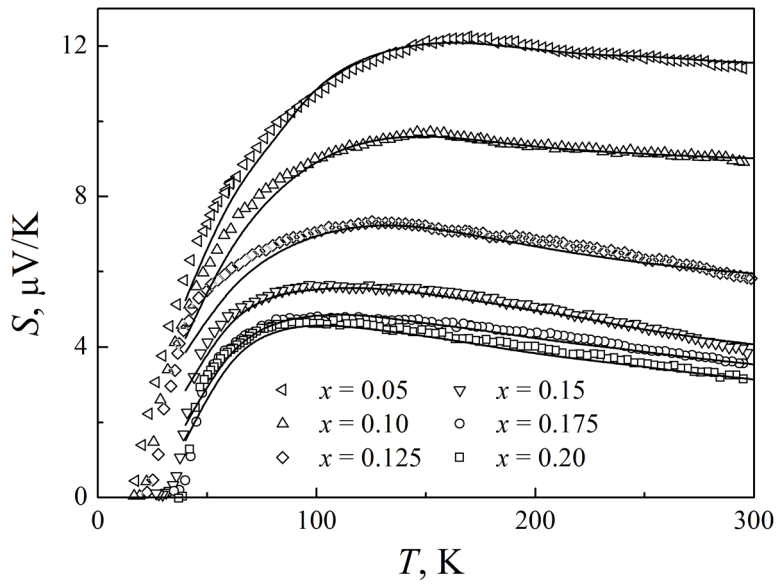

Fig. 3. Temperature dependences of the thermopower in $Y_{1-x}Ca_xBa_2Cu_{2.8}Zn_{0.2}O_y$. Symbols indicate experimental resuls; lines indicate results of calculation within the narrow-band model

The complete set of model parameters characterizing calcium's influence on the electronic structure and charge carrier system in $Y_{1-x}Ca_xBa_2Cu_{2.8}Zn_{0.2}O_y$ is presented in Table 1. The detailed discussion of calcium-induced changes in the F, W_D, W_σ, and b parameters, as well as the physical reasons for these changes, can be found elsewhere (Martynova et al. 2011). Here we would only like to emphasize that the energy parameters of the band (W_D and W_σ), which are little affected by zinc introduction, remain almost constant for all the studied samples. The band filling degree F and asymmetry parameter b exhibit systematic evolution with calcium content, progressively approaching the characteristic values of an undoped sample ($F \approx 0.5$, $b \approx 0$), while in calcium-free $YBa_2Cu_{2.8}Zn_{0.2}O_y$ they differ significantly from these values due to the zinc effect. This behavior quantitatively confirms calcium's compensating effect on zinc-induced electronic structure modifications, as discussed above.

Figure 4 presents the calculated charge carrier mobility values, which represent the band-averaged mobility determined through our narrow-band model rather than the conventional Nernst mobility defined as $Q/(k_B/e)$. This explains why the $u(x)$ dependence differs from the $Q_{300\,K}(x)$ behavior shown in Figure 2. The obtained mobility values are characteristically small, less than 1 $cm^2/(V\times s)$, which

 https://www.doi.org/10.33910/2687-153X-2025-6-2-59-68

Table 1. The values of model papameters determined from the joint analysis of the $S(T)$ and $Q(T)$ dependences in the $Y_{1-x}Ca_xBa_2Cu_{2.8}Zn_{0.2}O_y$ system

x	F	W_D, meV	$C \equiv W_\sigma / W_D$	b	u, cm²/(V·s)	k	$k \cdot W_D$, meV
0.05	0.535	102	0.37	0.017	0.48	–0.11	–11.2
0.1	0.524	96	0.36	0.011	0.45	–0.12	–11.5
0.125	0.520	103	0.39	0.007	0.29	–0.13	–13.4
0.15	0.517	97	0.33	0.004	0.36	–0.12	–11.6
0.175	0.513	95	0.35	0.000	0.47	–0.15	–14.3
0.2	0.509	90	0.41	–0.002	0.52	–0.15	–13.5

is consistent with previous results obtained for samples of the $YBa_2Cu_3O_y$ system with various types and levels of substitutions (Gasumyants, Martynova 2018). The mobility exhibits a non-monotonic dependence on calcium content, initially decreasing before showing an increase beyond $x = 0.125$. Note that to explain the variations in the mobility value under increasing doping level in various Y-based HTSC systems, we usually considered corresponding changes in the W_D and $C \equiv W_\sigma / W_D$ values (Gasumyants, Martynova 2018). As shown earlier (Gasumyants 2001), in most doped $YBa_2Cu_3O_y$ systems, non-isovalent impurities typically cause band broadening (increased W_D) and enhanced state localization at band edges (decreased $C \equiv W_\sigma / W_D$) via Anderson localization mechanism (Anderson 1958). Calcium doping in pre-doped systems produces the opposite effect on both these parameters (Gasumyants et al. 2000; Gasumyants, Martynova 2017).

The charge carrier mobility, defined as $u = e\langle\tau\rangle/m^*$, where $\langle\tau\rangle$ is the averaged relaxation time and m^* is the effective mass of electrons, exhibits doping-dependent behavior governed by two competing factors. Band broadening typically reduces the effective mass, which would enhance mobility, while impurity-induced disorder increases charge carrier scattering, reducing the relaxation time and consequently decreasing mobility. By analyzing these competing effects, we can consistently explain the doping-dependent mobility evolution observed in various doped systems (Gasumyants, Martynova 2018).

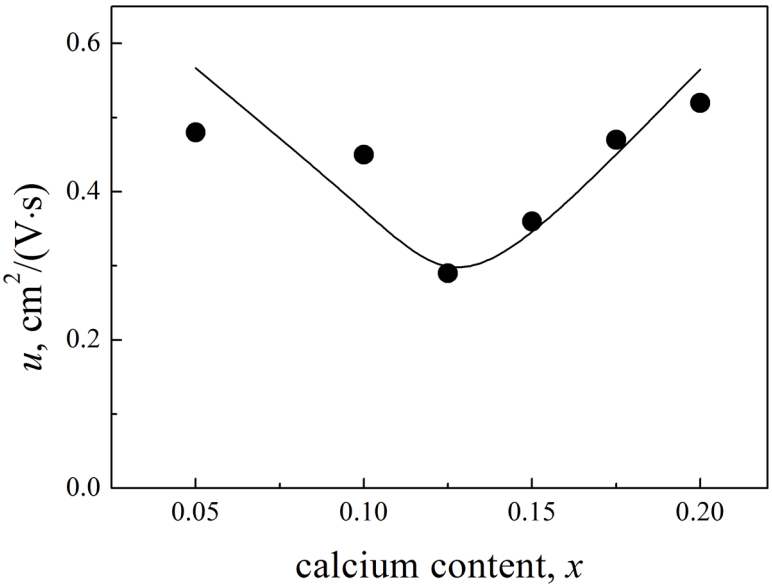

Fig. 4. Calculated charge-carrier mobility for $Y_{1-x}Ca_xBa_2Cu_{2.8}Zn_{0.2}O_y$ samples

Clearly, this approach cannot be applied to analyze the $u(x)$ dependence in the studied $Y_{1-x}Ca_xBa_2Cu_{2.8}Zn_{0.2}O_y$ system. As Table 1 shows, both the W_D and C values exhibit only minimal variation with increasing calcium content. However, it is important to note that W_D and W_σ represent effective widths of their respective energy intervals, namely the widths of rectangles approximating the $D(E)$ and $\sigma(E)$ functions. Most

substitutions in the $YBa_2Cu_3O_y$ system affect the energy spectrum indirectly through band broadening caused by the Anderson localization mechanism (Gasumyants 2001). In such cases, changes in W_D and W_σ accurately reflect the actual modifications of the $D(E)$ and $\sigma(E)$ functions under doping. In contrast, both calcium and zinc directly modify the energy spectrum — either through the formation of an additional Ca-induced peak in the $D(E)$ function or via Zn-induced state removal from the band. Under these circumstances, the rectangular approximation becomes too crude to quantitatively explain mobility variations by considering changes in the above two parameters. Qualitatively, the observed $u(x)$ dependence in $Y_{1-x}Ca_xBa_2Cu_{2.8}Zn_{0.2}O_y$ can be understood as follows. At low doping levels, calcium partially compensates for zinc's effect on the energy spectrum while simultaneously introducing additional disorder to the electronic structure established by zinc incorporation, ultimately reducing mobility. Near $x \approx 0.125$, zinc's influence becomes nearly compensated, as evidenced by the shape of the $Q(T)$ dependence for samples with $x \geq 0.15$ (discussed earlier). Further calcium doping, once zinc compensation is complete, increases mobility, which is consistent with previous observations in oxygen-deficient $Y_{1-x}Ca_xBa_2Cu_3O_y$ systems (Gasumyants, Martynova 2018). Thus, the change in the charge-carrier mobility in $Y_{1-x}Ca_xBa_2Cu_{2.8}Zn_{0.2}O_y$ with increasing calcium content can be explained by taking into account the compensating effect of calcium, similar to the explanation of the experimental results on the behavior of the Nernst coefficient.

As shown in Table 1, the dispersion law asymmetry parameter k remains negative and varies only slightly with changes of calcium content x in the $Y_{1-x}Ca_xBa_2Cu_{2.8}Zn_{0.2}O_y$ system. The kW_D value, representing the energy shift of the Hall conductivity sign-change point relative to the band center, also changes slightly between 11 and 14 meV. Note that this dispersion law asymmetry is not directly related to the asymmetry of the $D(E)$ function (parameter b in Table 1), which changes quite strongly in the studied system due to calcium-induced states appearing within the band. Our earlier studies (Gasumyants, Martynova 2018) established that such dispersion law asymmetry constitutes an intrinsic feature of the $YBa_2Cu_3O_y$ electronic structure, whereas the band asymmetry b emerges only under specific types of doping. Notably, despite the W_D value changes quite strongly with certain types of doping, the kW_D value in all cases varies in a relatively narrow range (Gasumyants, Martynova 2018). In particular, this value changes by 3 or 5 meV in cases of single doping with calcium or zinc, respectively, when the content of corresponding dopant changes from $x = 0$ to $x = 0.2$. The present results for double-substituted $Y_{1-x}Ca_xBa_2Cu_{2.8}Zn_{0.2}O_y$ system thus align well with this established pattern.

Conclusions

We have experimentally studied the Nernst coefficient in the $Y_{1-x}Ca_xBa_2Cu_{2.8}Zn_{0.2}O_y$ system with varying calcium content in the normal state and analyzed the $Q(T)$ dependences together with the thermopower data. The main results are as follows.

For samples with low calcium content ($x \leq 0.125$), the Nernst coefficient at high temperatures deviates from the temperature dependence characteristic of doped $YBa_2Cu_3O_y$ samples. This deviation gradually diminishes with increasing calcium content and vanishes completely for $x \geq 0.15$. Across all compositions, the room-temperature Nernst coefficient remains below 1 nV/(K·T), showing slight but non-monotonic variation with doping level. The behavior of both thermopower and Nernst coefficient in $Y_{1-x}Ca_xBa_2Cu_{2.8}Zn_{0.2}O_y$ can be satisfactorily described and quantitatively analyzed using the narrow-band model. This joint analysis allows one to determine, besides the fundamental energy spectrum parameters, the values of the charge-carrier mobility and the degree of dispersion law asymmetry. Despite calcium doping systematically modifies the density-of-states asymmetry, the dispersion law asymmetry remains essentially constant. This demonstrates that the latter represents an intrinsic feature of the $YBa_2Cu_3O_y$ energy spectrum rather than being doping-specific. The charge carrier mobility, which is notably low in all samples, decreases with an increase in calcium content at low doping levels, but increases for $x \geq 0.125$. These mobility variations, along with the Nernst coefficient behavior and changes in the calculated parameters of the energy spectrum structure, can be qualitatively explained by the compensating effect of calcium on zinc-induced disturbances in the electronic structure of the conductive band. Consequently, calcium doping enhances both superconducting properties and normal-state charge carrier characteristics in the $Y_{1-x}Ca_xBa_2Cu_{2.8}Zn_{0.2}O_y$ system.

Conflict of Interest

The authors declare that there is no conflict of interest, either existing or potential.

 https://www.doi.org/10.33910/2687-153X-2025-6-2-59-68

Author Contributions

Zh. Xunpeng performed measurements and simulations of Nernst coefficient temperature dependences and wrote the manuscript; V. E. Gasumyants analyzed the results and wrote the manuscript.

References

Ageev, N. V., Gasumyants, V. E. (2001) The Nernst-Ettingshausen coefficient in conductors with a narrow conduction band: Analysis and application of its results to HTSC materials. *Physics of the Solid State*, 43, 1834–1844. https://doi.org/10.1134/1.1410619 (In English)

Alexandrov, A. S., Zavaritsky, N. V. (2004) Nernst effect in poor conductors and in the cuprate superconductors. *Physical Review Letters*, 93, article 217002. https://doi.org/10.1103/PhysRevLett.93.217002 (In English)

Anderson, P. W. (1958) Absence of diffusion in certain random lattices. *Physical Review*, 109, 1492–1505. https://doi.org/10.1103/PhysRev.109.1492 (In English)

Awana, V. P. S., Malik, S. K., Yelon, W. B. (1996) Structural aspects and superconductivity in oxygen-deficient $Y_{1-x}Ca_xBa_2Cu_3O_{7-y}$ ($y \approx 0.3$) systems: A neutron-diffraction study. *Physica C: Superconductivity*, 262 (3–4), 272–278. https://doi.org/10.1016/0921-4534(96)00213-4 (In English)

Bonn, D. A., Kamal, S., Zhang, K., et al. (1994) Comparison of the influence of Ni and Zn impurities on the electromagnetic properties of $YBa_2Cu_3O_{6.95}$. *Physical Review B*, 50, 4051–4063. https://doi.org/10.1103/PhysRevB.50.4051 (In English)

Calzona, V., Cimberle, M. R., Ferdeghini, C. et al. (1995) Thermoelectric and thermomagnetic effects in the mixed state analysis of the thermal angle. *Physica C: Superconductivity*, 246, 169–176. https://doi.org/10.1016/0921-4534(95)00124-7 (In English)

Capan, C., Behnia, K., Hinderer, J. et al. (2002) Entropy of vortex cores near the superconductor-insulator transition in an underdoped cuprate. *Physical Review Letters*, 88, article 056601. https://doi.org/10.1103/PhysRevLett.88.056601 (In English)

Elizarova, M. V., Gasumyants, V. E. (2000) Band spectrum transformation and T_c variation in the $La_{2-x}Sr_xCuO_y$ system in the underdoped and overdoped regimes. *Physical Review B*, 62, 5989–5996. https://doi.org/10.1103/PhysRevB.62.5989 (in English)

Felner, I. (1991) The effect of chemical substitution on superconductivity in $YBa_2Cu_3O_7$. *Thermochimica Acta*, 174, 41–69. https://doi.org/10.1016/0040-6031(91)80152-9 (In English)

Funtikova, A., Gasumyants, V. (2023) Experimental study and analysis of the thermopower in the $Y_{1-x}Ca_xBa_2Cu_{3-x}Zn_xO_y$ system. In: *Proceedings of the 2023 International Conference on Electrical Engineering and Photonics (EExPolytech)*. [S. l.]: IEEE Publ., pp. 300–303. https://doi.org/10.1109/EExPolytech58658.2023.10318628 (In English)

Gasumyants, V. E. (2001) Analysis of the electron transport phenomena in HTSC-materials as the method of studying the band spectrum and its transformation under doping by different impurities. In: F. Gerard (ed.). *Advances in Condensed Matter and Materials Research. Vol. 1*. New York: Nova Science Publ., pp. 135–200. (In English)

Gasumyants, V. E., Elizarova, M. V., Vladimirskaya, E. V., Patrina, I. B. (2000) Ca effect on the normal-state and superconducting properties of Y-based HTS. *Physica C: Superconductivity*, 341–348, 585–588. https://doi.org/10.1016/S0921-4534(00)00604-3 (In English)

Gasumyants, V. E., Ageev, N. V., Elizarova, M. V. (2005) The Nernst-Ettingshausen coefficient in the normal phase of doped HTSCs of the $YBa_2Cu_3O_y$ system. *Physics of the Solid State*, 47, 202–213. https://doi.org/10.1134/1.1866394 (In English)

Gasumyants, V. E., Kaidanov, V. I., Vladimirskaya, E. V. (1995) The electron transport phenomena in Y-based HTSC`s and their analysis on the basis of phenomenological narrow-band theory. The band structure transformation with oxygen content and substitution for Cu. *Physica C: Superconductivity*, 248, 255–275. https://doi.org/10.1016/0921-4534(95)00173-5 (In English)

Gasumyants, V. E., Martynova, O. A. (2012) Normal-state band spectrum in chain-free high-temperature superconductors: mechanisms of modification under changing sample composition and influence of the normal-state parameters on the critical temperature. In: V. Rem Romanovskii (ed.). *Superconductivity: Theory, Materials and Applications*. New York: Nova Science Publ., pp. 285–326. (In English)

Gasumyants, V. E., Martynova, O. A. (2017) Specific features of the thermopower behavior of calcium-containing Y-based high-temperature superconductors: Experimental investigation and interpretation. In: A. Reimer (ed.). *Horizons in World Physics. Vol. 291*. New York: Nova Science Publ., pp. 129–216. (In English)

Gasumyants, V. E., Martynova, O. A. (2018) Experimental investigation and quantitative analysis of the normal-state Nernst coefficient in doped high-temperature superconductors of the $YBa_2Cu_3O_y$ system. In: M. Miryala, M. R. Koblishka (eds.). *High-Temperature Superconductors: Occurrence, Synthesis and Applications*. New York: Nova Science Publ., pp. 95–152. (In English)

Gasumyants, V. E., Vladimirskaya, E. V., Patrina, I. B. (1994) Transport properties, band spectrum, and superconductivity in the $Y_{1-x}Ca_xBa_2Cu_{3-z}Co_zO_y$ system. *Physica C: Superconductivity*, 235–240, 1467–1468. https://doi.org/10.1016/0921-4534(94)91958-5 (In English)

Gupta, R. P., Gupta, M. (1999) Effect of nickel and zinc substitutions on the electronic charge-density redistribution in a $YBa_2Cu_3O_7$ superconductor. *Physical Review B*, 59, 3381–3384. https://doi.org/10.1103/PhysRevB.59.3381 (In English)

Huebener, R. P., Kober, F., Ri, H.-C. et al. (1991) Seebeck and Nernst effect in the mixed state of slightly oxygen deficient YBaCuO. *Physica C: Superconductivity*, 181, 345–354. https://doi.org/10.1016/0921-4534(91)90122-F (In English)

Iye, Y. (1992) Transport properties of high T_c cuprates. In: D. M. Ginsberg (ed.). *Physical Properties of High Temperature Superconductors III*. Singapore: World Scientific Publ., pp. 285–361. (In English)

Kaiser, A. B., Ucher, C. (1991) Thermoelectricity of high-temperature superconductors. In: A. V. Narlikar (ed.). *Studies of High Temperature Superconductors. Vol. 7*. New York: Nova Science Publ., pp. 353–392. (In English)

Martin, E., Gasumyants, V. (2021) Zinc doping effect on the thermopower behavior and the modification of the normal-state energy spectrum in the $YBa_2Cu_3O_y$ system. In: *Proceedings of the 2021 International Conference on Electrical Engineering and Photonics (EExPolytech)*. [S. l.]: IEEE Publ., pp. 153–156. https://doi.org/10.1109/EExPolytech53083.2021.9614800 (In English)

Martynova, O. A., Potapov, D. V., Gasumyants, V. E., Vladimirskaya, E. V. (2011) Mechanism of a strong rise of T_c due to the calcium doping in $Y_{1-x}Ca_xBa_2Cu_{2.8}Zn_{0.2}O_y$. *Physica C: Superconductivity*, 471, 308–313. https://doi.org/10.1016/j.physc.2011.02.011 (In English)

Martynova, O. A., Gasumyants, V. E. (2013) Mechanism of cerium doping-induced formation and modification of the energy spectrum in the $Nd_{2-x}Ce_xCuO_y$ system. *Physics of the Solid State*, 55, 254–261. https://doi.org/10.1134/S1063783413020200 (In English)

Ong, N. P. (1990) The Hall effect and its relation to other transport phenomena in the normal state of the high-temperature superconductors. In: D. M. Ginsberg (ed.). *Physical Properties of High Temperature Superconductors II*. Singapore: World Scientific Publ., pp. 459–507. (In English)

Qussena, M., Gagnon, R., Wang, Y., Aubin, M. (1992) Magneto-Seebeck and Nernst-effect measurements on $YBa_2Cu_3O_{7-x}$ single crystals. *Physical Review B*, 46, 528–531. https://doi.org/10.1103/PhysRevB.46.528 (In English)

Suard, E., Maignan, A., Caignaert, V., Raveau, B. (1992) Effect of Y-Ca substitution upon superconductivity in the oxide $YBa_2Cu_{3-x}Co_xO_{7-\delta}$. *Physica C: Superconductivity*, 200, 43–49. https://doi.org/10.1016/0921-4534(92)90320-C (In English)

Tan, S., Levin, K. (2004) Nernst effect and anomalous transport in cuprates: A preformed-pair alternative to the vortex scenario. *Physical Review B*, 69, article 064510. https://doi.org/10.1103/PhysRevB.69.064510 (In English)

Wang, N. L., Tajima, S., Rykov, A. I., Tomimoto, K. (1998) Zn-substitution effects on the optical conductivity in $YBa_2Cu_3O_{7-\delta}$ crystals: Strong pair breaking and reduction of in-plane anisotropy. *Physical Review B*, 57, R11081–R11084. https://doi.org/10.1103/PhysRevB.57.R11081 (In English)

Wang, Y., Xu, Z. A., Kakeshita, T. et al. (2001) Onset of the vortex-like Nernst signal above T_c in $La_{2-x}Sr_xCuO_4$ and $Bi_2Sr_{2-y}La_yCuO_6$. *Physical Review B*, 64, article 224519. https://doi.org/10.1103/PhysRevB.64.224519 (In English)

Xu, Z. A., Ong, N. P., Wang, Y. et al. (2000) Vortex-like excitations and the onset of superconducting phase fluctuation in underdoped $La_{2-x}Sr_xCuO_4$. *Nature*, 406, 486–488. https://doi.org/10.1038/35020016 (In English)

Condensed Matter Physics.
Dielectrics

UDC 538.956

EDN VSUTSU
https://www.doi.org/10.33910/2687-153X-2025-6-2-69-86

Dielectric spectroscopy of a 10% solution of human immunoglobulin G at physiological temperatures. Part 1

Zh. A. Salnikova ✉[1], A. P. Smirnov [1], R. A. Castro Arata [1]

[1] Herzen State Pedagogical University of Russia, 48 Moika Emb., Saint Petersburg 191186, Russia

Authors

Zhanna A. Salnikova, ORCID: 0000-0002-8244-7513, e-mail: jannete90@mail.ru

Alexander P. Smirnov, ORCID: 0000-0003-2463-2056, e-mail: Smirnov_Alexander_hspu@mail.ru

Rene Alejandro Castro Arata, ORCID: 0000-0002-1902-5801, e-mail: recastro@mail.ru

For citation: Salnikova, Zh. A., Smirnov, A. P., Castro Arata, R. A. (2025) Dielectric spectroscopy of a 10% solution of human immunoglobulin G at physiological temperatures. Part 1. *Physics of Complex Systems*, 6 (2), 69–86. https://www.doi.org/10.33910/2687-153X-2025-6-2-69-86 EDN VSUTSU

Received 14 March 2025; reviewed 31 March 2025; accepted 31 March 2025.

Funding: The study did not receive any external funding.

Abstract. In this paper, the dielectric and relaxation properties of a 10% water solution of human immunoglobulin are investigated in the frequency range of 0.1 Hz to 15 MHz at temperatures between 35 and 39.7 °C. The frequency dependences of the dielectric loss factor ε" were obtained, revealing three maxima in the dispersion regions ε'. These maxima were approximated by the Havriliak–Negami equation. For each relaxation process, the parameters α, β, and τ_0 were calculated at different temperatures, and the time distribution functions of the relaxers, G(t), were derived. The paper proposes possible interpretations of the kinetic units responsible for these processes and discusses potential phase transitions within the system.

Keywords: dielectric constant of immunoglobulin G, dielectric losses of IgG, relaxation parameters of IgG, Havriliak–Negami equation, phase transitions, globule–tangle, immunoglobulins

Introduction

In the physics of dielectrics, the method of dielectric spectroscopy is widely used for comprehensive studies of the frequency dependences of the dielectric constant $\varepsilon'(f)$ and the dielectric loss factor $\varepsilon''(f)$. The fundamental principles of this method are well-documented in both domestic and international educational and scientific literature. See, for example (Borisova, Koikov 1979; Gorokhovatskiy et al. 2013; Kremer, Schönhals 2003). This technique has been applied to investigate synthetic polymer dielectrics as well as biological objects (Blythe, Bloor 2005; Sazhin 1986; Annus, Min 2021; Raicu, Feldman 2015). The relaxation parameters of dielectrics are determined from the maxima observed in the frequency dependence of the dielectric loss factor and are typically analyzed using the Havriliak — Negami equation. From this analysis, the relaxation parameters α, β, and τ_0 are obtained at various temperatures, the time distribution functions of the relaxers, $G(\tau)$, are derived, and the activation energy E_a of the dipole polarization process is calculated.

In this work, the object of the study is a 10% aqueous solution of human immunoglobulin G (IgG). The purpose of this study is to investigate the dielectric characteristics and relaxation parameters of the sample across a broad frequency range at physiological temperatures, followed by comprehensive analysis of the obtained results.

Relaxation equations

To analyze the relaxation properties of dielectrics, we employ the concept of complex dielectric constant ε^*, defines as:

$$\varepsilon^*(\omega) = \varepsilon'(\omega) - i\cdot\varepsilon''(\omega), \tag{1}$$

where ω is the cyclic frequency of the applied electric field, $\varepsilon'(\omega)$ denotes the real part (permittivity of the medium) characterizing the medium's ability to shield an external electric field, $\varepsilon''(\omega)$ represents the imaginary part (dielectric loss factor) describing energy absorption and its conversion to thermal energy.

Relaxation phenomena are generally described by the Havriliak–Negami equation (H–N) (Kremer, Schönhals 2003, 62) (we used in the formula $1 - \alpha$, $1 - \beta$):

$$\varepsilon^*(\omega) = \varepsilon_\infty + \frac{\varepsilon_s - \varepsilon_\infty}{(1+(i\omega\tau_0)^{1-\alpha})^{1-\beta}}, \tag{2}$$

where ε_s, ε_∞ are the static and high–frequency dielectric constant $\varepsilon'(\omega)$ (ε_s – at $\omega \to 0$, ε_∞ – at $\omega \to \infty$), τ_0 is the most probable relaxation time of the sample molecules (or their individual kinetic units), α is the width of the relaxation time spectrum, β is the dissymmetry of this spectrum. These parameters vary within the following limits: $0 \le \alpha < 1$, $0 \le \beta < 1$. The greater the value α, the greater the spread of relaxation times of the sample molecules τ relative to τ_0, that is, the wider the relaxation spectrum (therefore, the value $1 - \alpha$ is used in the formula in this work); the greater β, the greater the degree of its dissymmetry (therefore, we use the value $1 - \beta$ in the formula). For such complex systems as aqueous solutions of biopolymers, the α parameter and, especially, the β parameter are significantly higher than for low molecular weight compounds.

When considering the sample molecules as independent dipoles with several discrete orientation states, it is concluded that there are molecules with different relaxation times τ (Fröhlich 1958). The distribution of molecules with different τ relative to τ_0 is described by the function $G(\tau)$ (Kremer, Schönhals 2003, 62):

$$G(\tau) = \frac{\left(\frac{\tau}{\tau_0}\right)^{\beta(1-\alpha)} \sin\left((1-\beta)\theta\right)}{\pi\tau\left[\left(\frac{\tau}{\tau_0}\right)^{2(1-\alpha)} + 2\left(\frac{\tau}{\tau_0}\right)^{(1-\alpha)} \cos(\pi(1-\alpha)) + 1\right]^{\frac{1-\beta}{2}}}, \tag{3}$$

where: $\theta = arctg\left[\frac{\sin\left(\pi(1-\alpha)\right)}{\left(\frac{\tau}{\tau_0}\right)^{(1-\alpha)} + \cos(\pi(1-\alpha))}\right]$ and $0 \le \theta \le \pi$.

At $\alpha = 0$ and $\beta = 0$, the H–N equation becomes the Debye equation (Kremer, Schönhals 2003, 62):

$$\varepsilon^*(\omega) = \varepsilon_\infty + \frac{\varepsilon_s - \varepsilon_\infty}{1+i\omega\tau_0}, \tag{4}$$

In this case, $G(\tau)$ is a delta function $\delta(\tau_0)$, which corresponds to the state when all kinetic units of the sample have the same relaxation time τ_0.

At $\alpha \neq 0$ and $\beta = 0$, the H–N equation becomes the Cole–Cole equation (Kremer, Schönhals 2003, 62):

$$\varepsilon^*(\omega) = \varepsilon_\infty + \frac{\varepsilon_s - \varepsilon_\infty}{1+(i\omega\tau_0)^{1-\alpha}}, \tag{5}$$

Here $G(\tau)$ is a symmetric function with respect to τ_0.

 https://www.doi.org/10.33910/2687-153X-2025-6-2-69-86

At $\alpha = 0$ and $\beta \neq 0$, the H–N equation becomes the Davidson–Cole equation (Kremer, Schönhals 2003, 62):

$$\varepsilon^*(\omega) = \varepsilon_\infty + \frac{\varepsilon_s - \varepsilon_\infty}{(1+i\omega\tau_0)^{1-\beta}}, \quad (6)$$

In this case, $G(\tau)$ is an asymmetric function with respect to τ_0.

The parameters α, β, and τ_0 are the main relaxation parameters of the object of study.

The parameter α characterizes how strongly the relaxation times τ of the kinetic units of a given relaxation process differ in frequency. The more kinetic units with different relaxation times, the greater the α. The parameter β determines the cooperative nature of the reorientation of kinetic units, considered as dipoles that make abrupt turns under the influence of an external field, in which the probability of reorientation of the kinetic unit and the activation energy depend on the orientation of the neighbors. The stronger the dependence on the orientation of the neighbors, the greater the β.

Method for determining relaxation parameters α, β, and τ_0

From equation H–N (2) and considering the aforementioned theoretical framework, we derive the equation for $\varepsilon''(\omega)$ (Salnikova, Kononov 2020):

$$\varepsilon''(\omega) = \frac{(\varepsilon_s - \varepsilon_\infty)\cdot \sin(1-\beta)\varphi}{[1 + 2(\omega\tau_0)^{1-\alpha}\sin\frac{\pi\alpha}{2} + (\omega\tau_0)^{2(1-\alpha)}]^{\frac{1-\beta}{2}}}, \quad (7)$$

where $\varphi = arctg[\frac{(\omega\tau_0)^{1-\alpha}\cos\frac{\pi\alpha}{2}}{1+(\omega\tau_0)^{1-\alpha}\sin\frac{\pi\alpha}{2}}]$.

Experimentally measured quantities are usually $\varepsilon'(\omega)$ and $\varepsilon''(\omega)$. At the same time, a dispersion is observed on the graph $\varepsilon'(\omega)$, and a maximum in the frequency band of the dispersion $\varepsilon'(\omega)$ is observed on the graph $\varepsilon''(\omega)$. The relaxation parameters α, β, and τ_0 are determined empirically at each temperature, from the principle of the best approximation of the experimental values $\varepsilon''(\omega)$ by the graph $\varepsilon''(\omega)$ according to formula (7). When constructing an approximating curve for the graph $\varepsilon''(\omega)$, the least squares method is used. Having obtained the values α, β and τ_0, the relaxation time distribution function of the molecules of the sample $G(\tau)$ is constructed according to formula (3).

In the presence of several relaxation processes, as well as in the presence of electrical conductivity of the sample, the H–N equation is used in a generalized form:

$$\varepsilon^*(\omega) = -i\left(\frac{\sigma_0}{\varepsilon_0\omega}\right)^s + \sum_{k=1}^{3}\left[\frac{\varepsilon_{sk} - \varepsilon_{\infty k}}{(1+(i\omega\tau_k)^{1-\alpha_k})^{1-\beta_k}} + \varepsilon_{\infty k}\right] \quad (8)$$

This formula takes into account three relaxation processes, with the first term accounting for electrical conductivity effects. The parameters are the same as in formula (2), σ_0 is the electrical conductivity at the minimum frequency under study, s is the exponent $0 \leq s \leq 1$, ε_0 is the dielectric constant ($\varepsilon_0 = 8.85\cdot10^{-12}$ F/m).

Proteins exhibit a broad spectrum of motional modes across multiple structural scales — including quaternary, tertiary, secondary, and primary structure rearrangements — each characterized by distinct activation barriers and characteristic timescales. Motional modes with comparable relaxation times may be collectively described as a single relaxation process (Gotlib et al. 1986, 156), though this aggregation typically results in a markedly asymmetric relaxation time distribution function $G(\tau)$ (Gotlib et al. 1986, 159). This behavior manifests experimentally as a broad and asymmetric relaxation spectrum on the graph $\varepsilon''(f)$.

Experiment

Samples

The experimental samples consisted of human normal immunoglobulin produced by NPO Microgen JSC (Moscow, Russia), obtained through standard pharmaceutical distribution channels in the Russian Federation. The preparation contained 100 mg of human plasma proteins per 1 mL solution, with IgG comprising at least 97% of the protein content. The formulation included 22.5 mg of glycine (aminoacetic acid) and up to 1 mL water for injection.

Measurement procedure

The complex dielectric permittivity was measured using a Novocontrol Concept 41 spectrometer at the interdisciplinary Resource Center for collective use of Herzen University (Modern Physical and Chemical Methods for the Research and Development of Materials for Industry, Science, and Education). The frequency range spanned from 0.1 Hz to 15 MHz, and measurements were conducted at controlled temperatures between 35 and 39.7 °C.

Data acquisition and analysis were performed using WinDETA software (Novocontrol Technologies GmbH, Germany).

For each temperature, the relaxation parameters (α, β, τ_0) and the relaxation time distribution function $G(\tau)$ were determined via WinFit software (Novocontrol Technologies GmbH & Co). This software employs an approximation algorithm for $\varepsilon''(\omega)$ based on formula (8) and the methodology described earlier.

The measuring cell was a flat capacitor with a 0.24 mm. distance between the plates. The sample volume for each measurement was 5 μL.

Results and discussion

The obtained results

The frequency-dependent dielectric properties $\varepsilon'(f)$, $\varepsilon''(f)$, and $tg\delta$ were measured across the frequency range of 0.1 Hz to 15 MHz at temperatures between 35 and 39.7 °C, with temperature increments of 0.3–0.4 °C.

Figure 1 presents the three-dimensional frequency-temperature dependence of $tg\delta$.

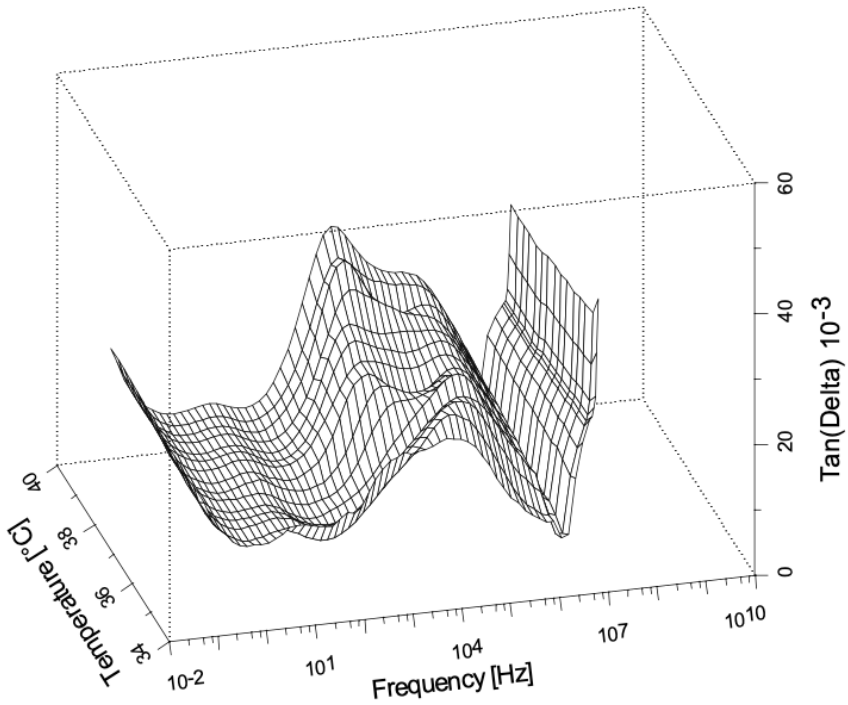

Fig. 1. The value of $tg\delta(f,T)$ at f = 0.1Hz–15 MHz, T = 35–39.7 °C

https://www.doi.org/10.33910/2687-153X-2025-6-2-69-86

Figure 2 shows the frequency dependences $\varepsilon'(f)$ for the temperature range of 35–39.7 ^{0}C. Similarly, Figure 3 shows the frequency dependences $\varepsilon''(f)$ across the same temperature range.

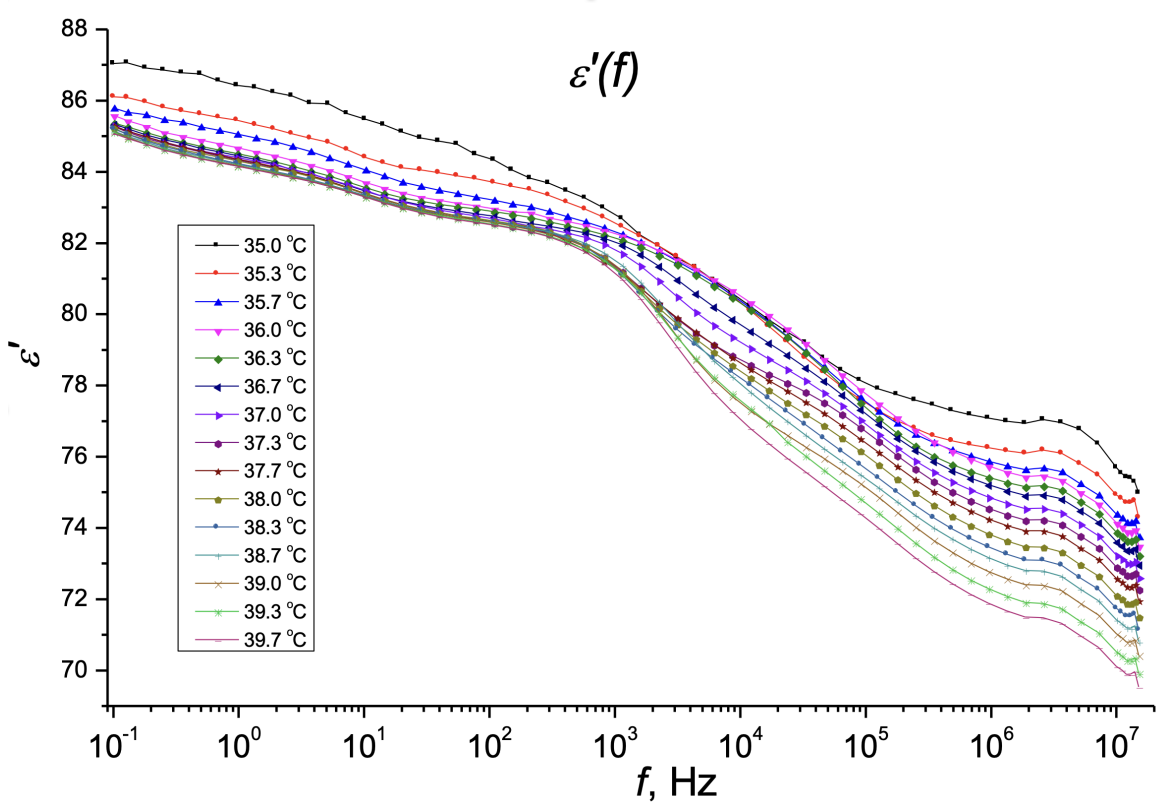

Fig. 2. Frequency dependence of $\varepsilon'(f)$ at T = 35–39.7 °C

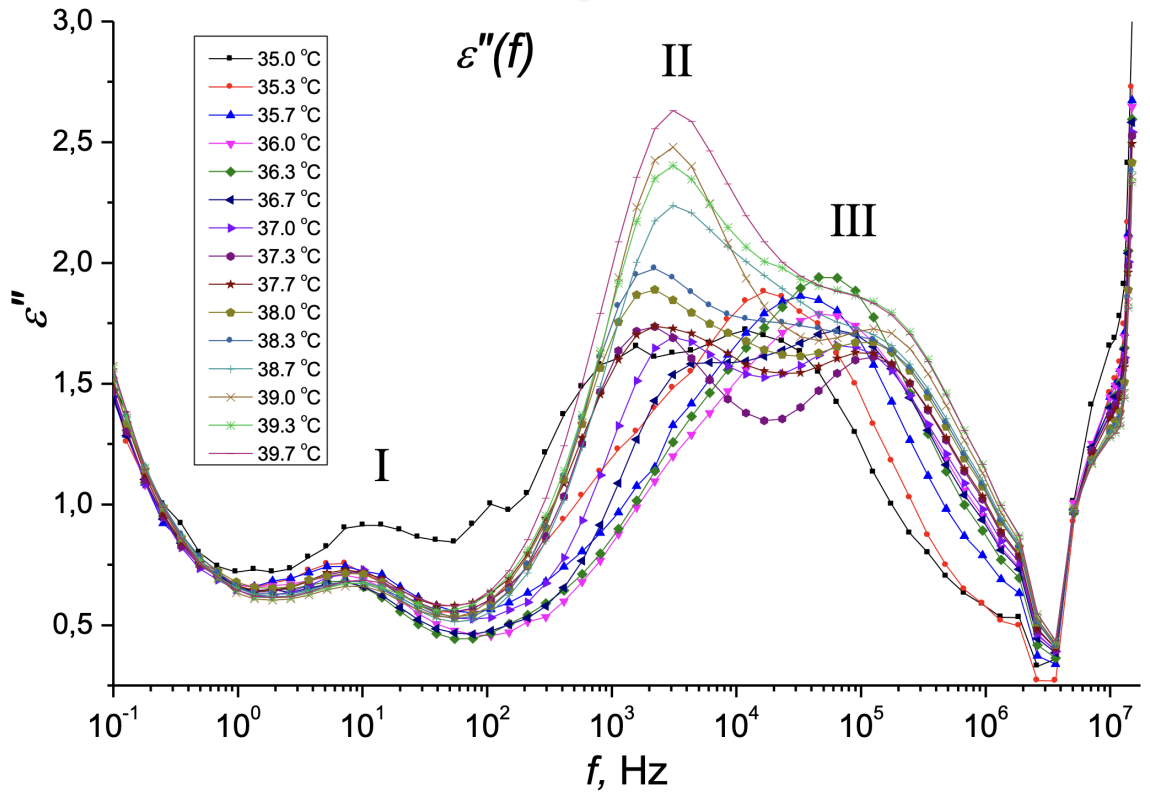

Fig. 3. Frequency dependence $\varepsilon''(f)$ at T = 35–39.7 °C

Figure 3 reveals three distinct relaxation maxima located at approximately $f \approx 10$ Hz, $f \approx 3 \times 10^3$ Hz, and $f \approx 5 \times 10^4$ Hz. Corresponding dispersion regions for $\varepsilon'(f)$ are evident in Figure 2 within these frequency ranges. The shift of the $\varepsilon''(f)$ maxima toward higher frequencies with increasing temperature confirms the relaxation nature of these processes. At the same time, all the three processes partially overlap. The first relaxation process terminates near $f \sim 10^2$Hz, however, $\varepsilon''(f)$ remains non-zero due to the onset of the second relaxation process. This second process subsequently transitions into the third relaxation process at higher frequencies. Notably, the overlap between the second and third processes is significantly more pronounced than between the first and second processes. At frequencies exceeding 10^7 Hz, an increase in $\varepsilon''(f)$ suggests the presence of an additional relaxation process. However, the absence of a maximum in this frequency range prevents reliable determination of its parameters.

In the low-frequency range of 0.1–1 Hz, an increase in $\varepsilon''(f)$ is also observed. This behavior is either due to significant changes in the sample's electrical conductivity at low frequencies or to the presence of an additional relaxation process.

Figures 4 and 5 show the detailed frequency dependence of $\varepsilon''(f)$ for the first relaxation process (I) across different temperature ranges. A broad, asymmetric maximum is observed at $f \sim 10$ Hz, which narrows with increasing temperature.

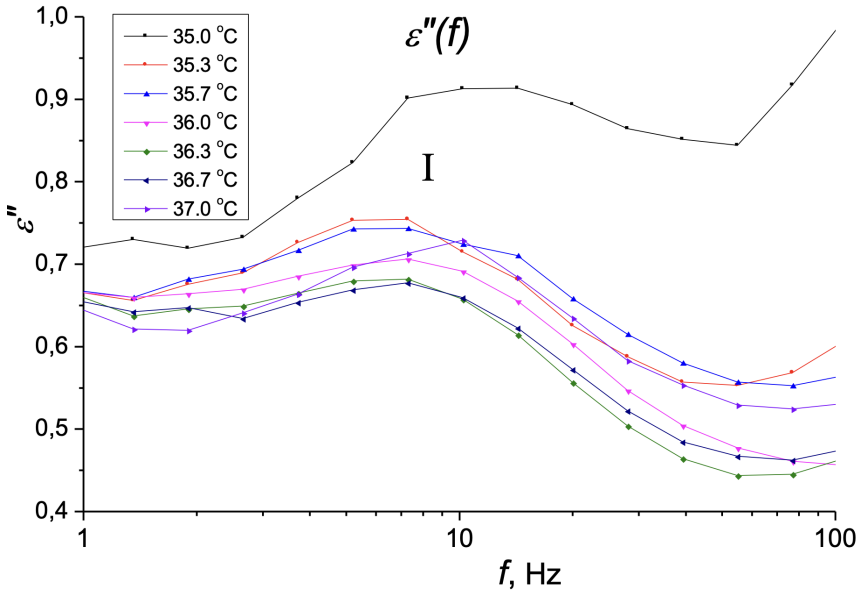

Fig. 4. Frequency dependence $\varepsilon''(f)$ for process I at T = 35.0–37.0 °C

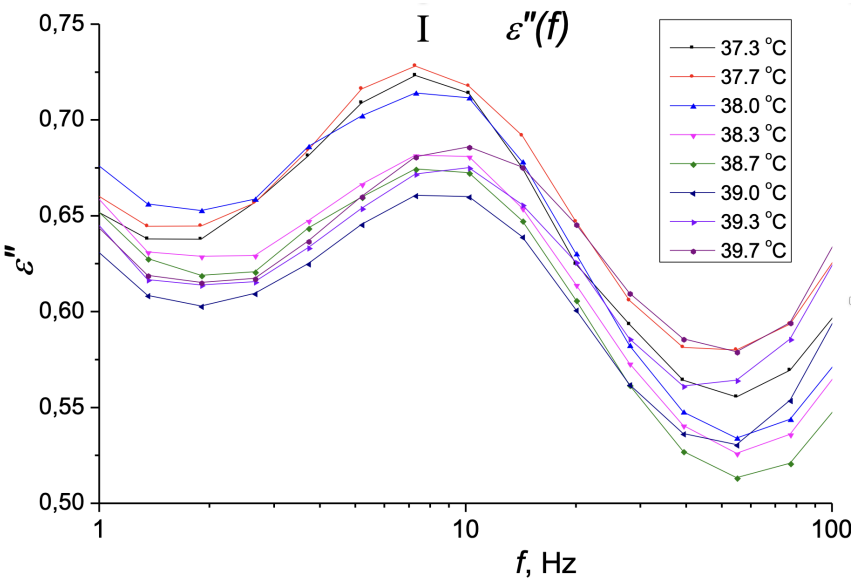

Fig. 5. Frequency dependence $\varepsilon''(f)$ for process I at T = 37.3–39.7 °C

https://www.doi.org/10.33910/2687-153X-2025-6-2-69-86

Figures 6 and 7 show the detailed frequency dependences of $\varepsilon''(f)$ in the range of 100 Hz to 2 MHz across different temperature ranges. Two partially overlapping relaxation processes (II and III) are observed: process II at $f \sim 3 \times 10^3$ Hz and process III at $f \sim 10^5$ Hz. The maximum values of both processes are three times larger than those of the first process. With increasing temperature, process II becomes more pronounced relative to process III.

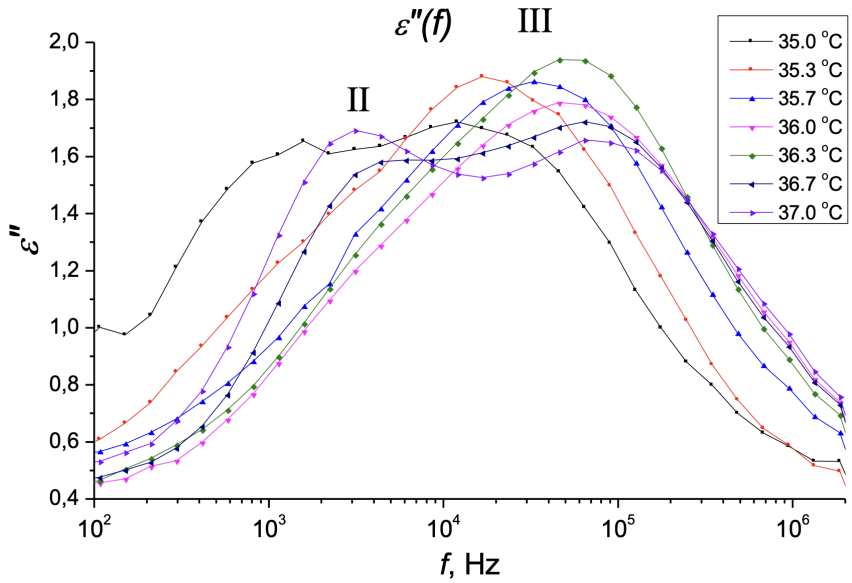

Fig. 6. Frequency dependence $\varepsilon''(f)$ for processes II, III at T = 35.0–37.0 °C

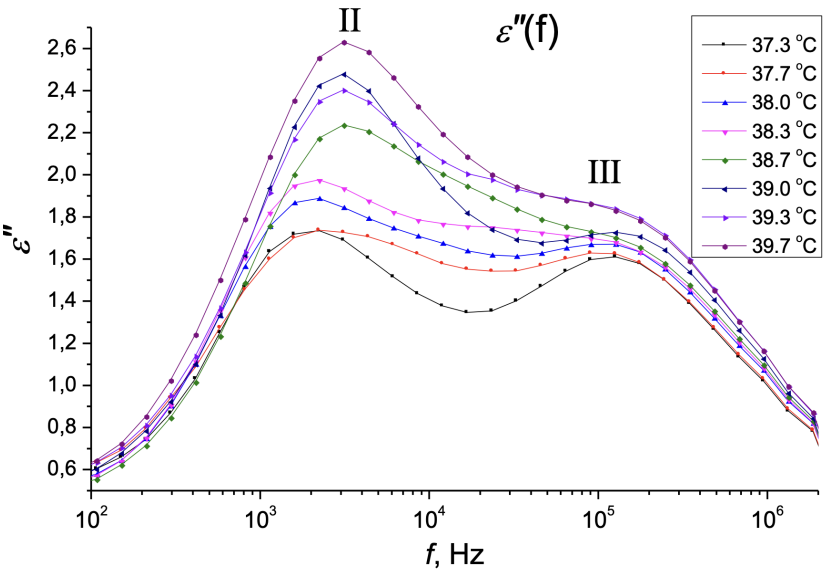

Fig. 7. Frequency dependence $\varepsilon''(f)$ for processes II, III at T = 37.3–39.7 °C

For all observed processes (I, II, III), the relaxation parameters α, β, and τ_0 were determined using the WinFit software following the previously described methodology. The analysis employed the H–N equation (8), which simultaneously accounts for three relaxation processes and electrical conductivity. Experimental data points at frequencies above 2×10^6 Hz were excluded. Figure 8 presents the analysis results for T = 37.3 °C, showing the experimental $\varepsilon''(f)$ data points along with the approximation curve, individual contributions from each relaxation process, and the electrical conductivity at low frequencies. The derived parameters α, β and τ_0 were used to construct the relaxation time distribution function $G(\tau)$, displayed in Figure 9. It shows an overlap between all three relaxation processes (I, II, III).

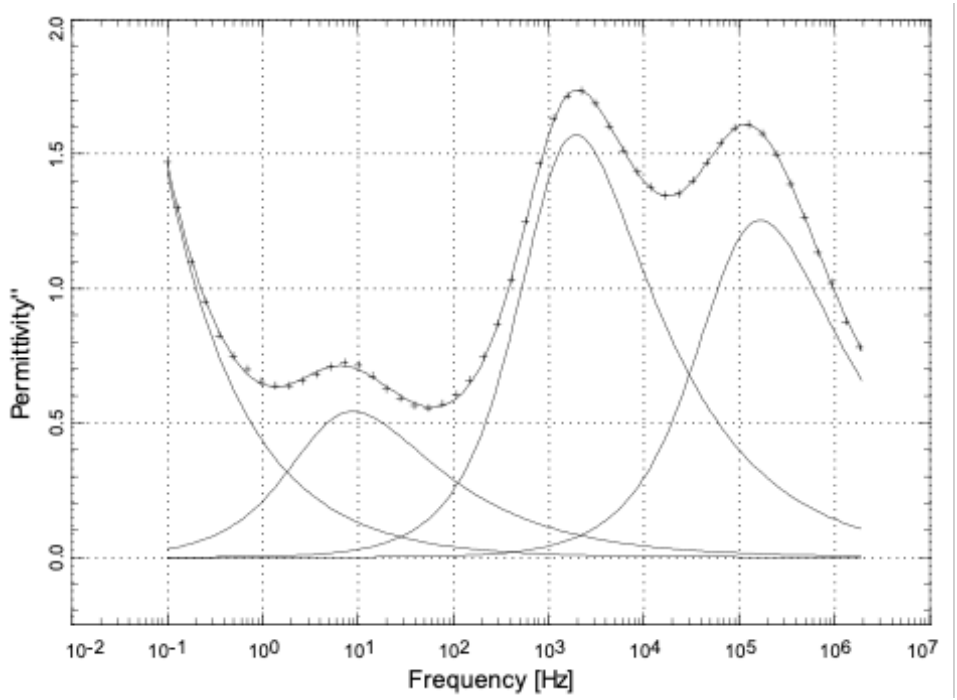

Fig. 8. *ε″(f)* at T = 37.3 °C

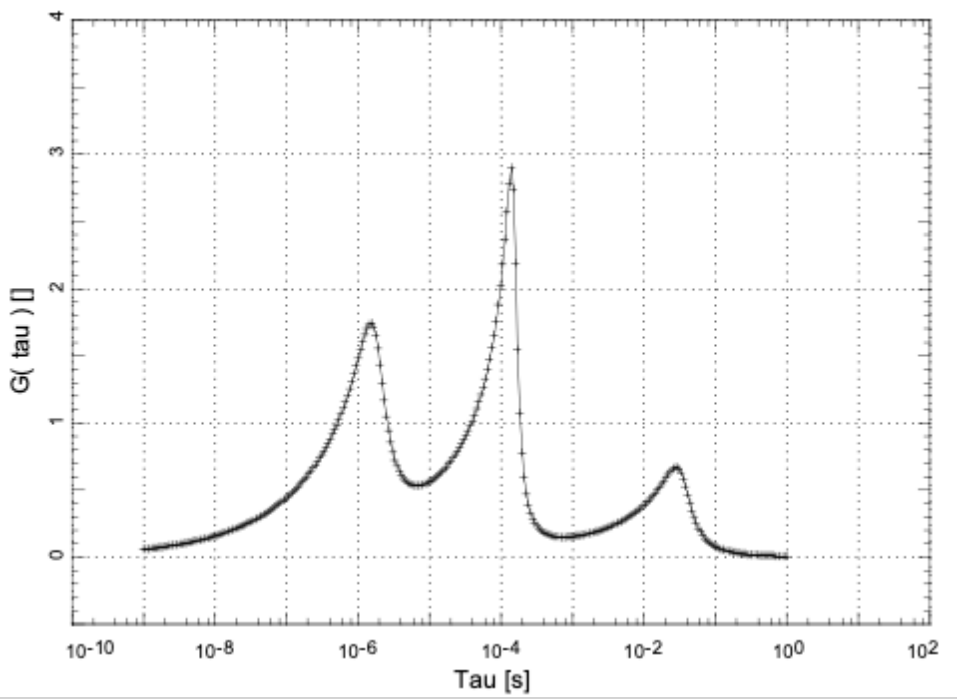

Fig. 9. *G(τ)* for Fig. 8

The calculated relaxation parameters (α, β, τ_o) for each process at all temperatures are presented in Table 1. The approximation error for α and β did not exceed 0.04, while for τ_o it remained below 15%. When α and β values approached 0.00, their error did not exceed 0.02.

Figure 10 shows the Cole-Cole diagrams for different temperatures. The diagrams are asymmetrical in shape, and their centers (if modeled as semicircular arcs) are located below the ε' axis. This graphically confirms the large values of the α and β parameters. At T = 35 °C, the diagram differs significantly from those at other temperatures. Studying this phenomenon requires additional data at lower temperatures, which will be presented in future work.

 https://www.doi.org/10.33910/2687-153X-2025-6-2-69-86

Table 1. Values of relaxation parameters α, β, τ_0 (according to equation 8)

T, °C	The first (I) relaxation process: f = 1–100 Hz			The second (II) relaxation process: f = 100 Hz–10 kHz			The third (III) relaxation process: f= 10 kHz–1 MHz		
	α_1	β_1	τ_{0_1} (s)	α_2	β_2	τ_{0_2} (s)	α_3	β_3	τ_{0_3} (s)
35.0	0.10	0.74	3.6×10^{-2}	0.00	0.77	3.7×10^{-4}	0.11	0.37	8.7×10^{-6}
35.3	0.13	0.08	2.4×10^{-2}	0.32	0.00	1.3×10^{-4}	0.22	0.43	1.1×10^{-5}
35.7	0.13	0.42	3.4×10^{-2}	0.38	0.08	6.3×10^{-5}	0.25	0.44	6.9×10^{-6}
36.0	0.15	0.42	3.6×10^{-2}	0.32	0.00	3.5×10^{-5}	0.26	0.44	3.6×10^{-6}
36.3	0.00	0.59	4.8×10^{-2}	0.34	0.20	3.7×10^{-5}	0.16	0.47	3.7×10^{-6}
36.7	0.10	0.59	4.2×10^{-2}	0.11	0.29	6.1×10^{-5}	0.20	0.48	3.1×10^{-6}
37.0	0.13	0.51	3.2×10^{-2}	0.08	0.29	7.9×10^{-5}	0.22	0.46	2.7×10^{-6}
37.3	0.12	0.52	3.6×10^{-2}	0.05	0.53	1.6×10^{-4}	0.12	0.51	1.9×10^{-6}
37.7	0.18	0.27	2.5×10^{-2}	0.13	0.67	1.9×10^{-4}	0.16	0.37	1.4×10^{-6}
38.0	0.17	0.35	2.7×10^{-2}	0.00	0.72	2.1×10^{-4}	0.24	0.25	1.2×10^{-6}
38.3	0.18	0.25	2.2×10^{-2}	0.00	0.57	1.7×10^{-4}	0.42	0.00	1.2×10^{-6}
38.7	0.18	0.28	2.4×10^{-2}	0.09	0.53	1.1×10^{-4}	0.38	0.00	8.2×10^{-7}
39.0	0.14	0.49	3.4×10^{-2}	0.10	0.19	7.0×10^{-5}	0.33	0.06	9.3×10^{-7}
39.3	0.26	0.31	2.4×10^{-2}	0.08	0.49	1.1×10^{-4}	0.36	0.00	8.9×10^{-7}
39.7	0.23	0.04	1.7×10^{-2}	0.15	0.29	7.9×10^{-5}	0.33	0.15	1.1×10^{-6}

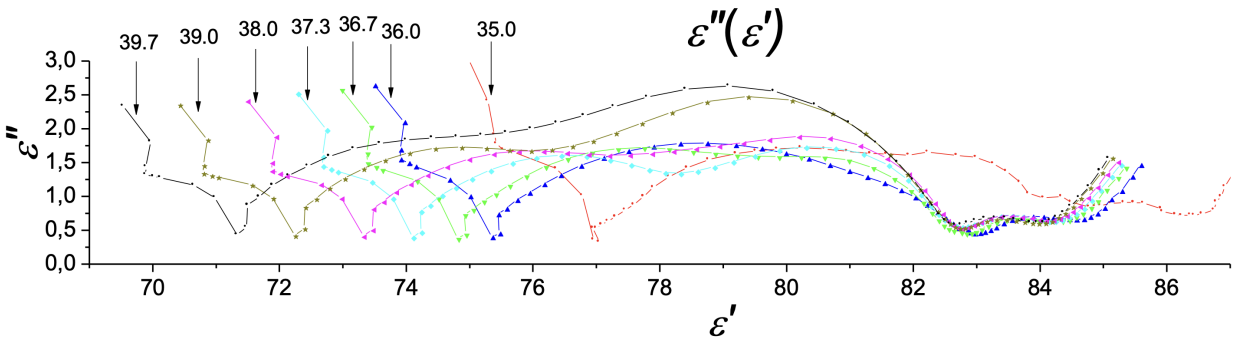

Fig. 10. $\varepsilon''(\varepsilon')$ at T = 35–39.7 °C

Figure 11 presents the function $G(\tau)$ at different temperatures. Three maxima corresponding to three overlapping relaxation processes are visible. The shape of $G(\tau)$ varies with temperature. The decomposition of $G(\tau)$ into components will be presented below (see Figs. 14, 16, 18).

Let us consider the IgG molecule in terms of potential kinetic units responsible for these relaxation processes.

Immunoglobulin G (Litman, Good 1978)

The immunoglobulin G (IgG) molecule is a Y-shaped, globular, water-soluble protein with a molecular weight of 150 kDa. It consists of four polypeptide chains: two light (L) chains (25 kDa each) and two heavy (H) chains (50 kDa each). These chains are covalently linked through interchain disulfide bonds to form a single structure. Figure 12 presents a schematic representation of the IgG molecule.

The quaternary structure of IgG comprises three globular regions: two Fab fragments and one Fc fragment. Each fragment contains four domains: the Fab fragments consist of V_L, V_H and C_L, and C_H1 domains, while the Fc fragment contains two C_H2 and two C_H3 domains. Within these domains, the polypeptide chains primarily adopt β-sheet conformations with parallel folds, while α-helices are essentially absent. The domain geometries shown in Figure 12, along with the dimensions of Fab and Fc fragments, were determined through X-ray diffraction analysis. Crystallographic and hydrodynamic

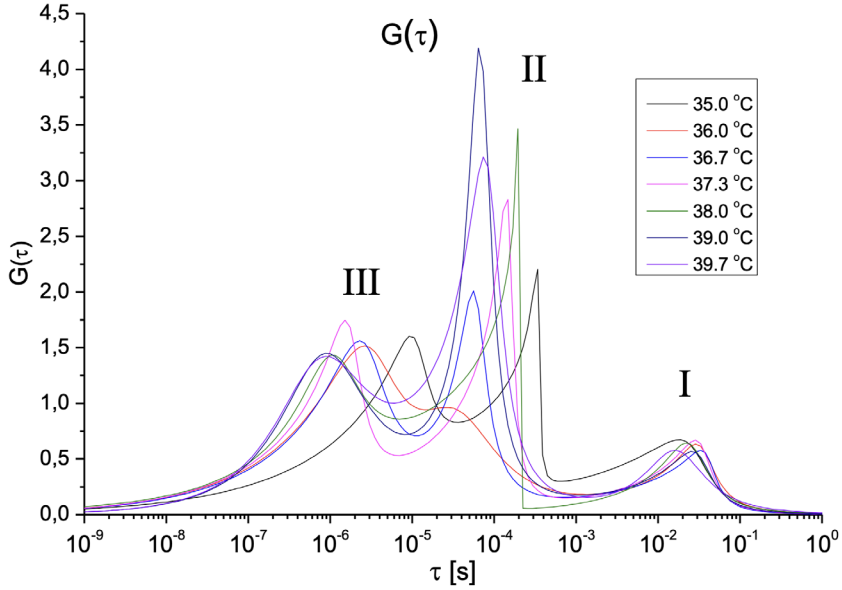

Fig. 11. *G(τ)* at *T* = 35–39.7 °C

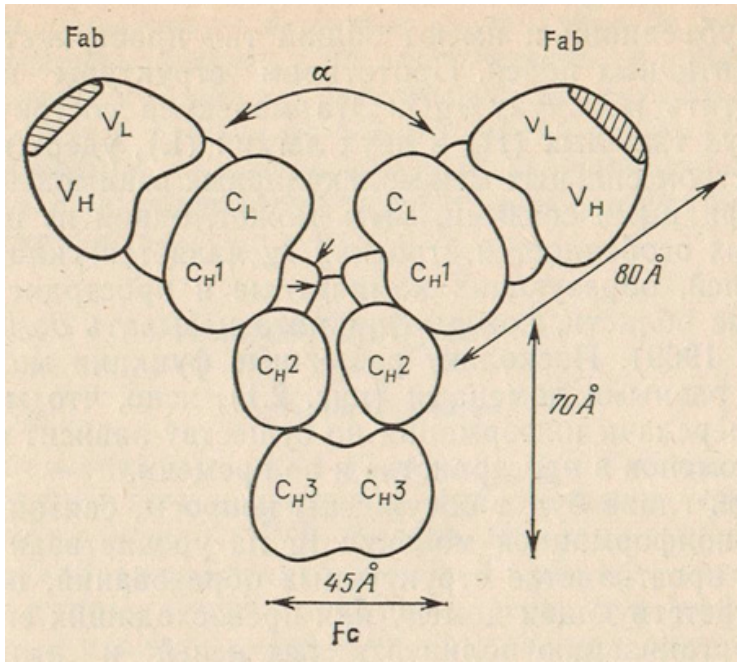

Fig. 12. Schematic representation of the IgG structure. Taken from (Litman, Good 1978, 59)

studies of Fab and Fc fragments reveal that they can be approximated as ellipsoids of revolution with an axial ratio of 2:1, with each Fab fragment exhibiting a relatively large free volume in its central region. Antigen-binding sites are located at the tips of the Fab fragments, indicated in Figure 12 by shaded areas. The Fc fragment contains a hinge region between the two C_H2 domains (indicated by arrows in Figure 12) that enables variation of the angle α between Fab fragments. Typically, this angle exceeds 90–100°. Antigen binding induces conformational changes in the α angle, triggering IgG's biological functions, i. e., the immune response against antigens.

The Fc fragment may adopt an asymmetric position relative to the Fab fragments and need not lie within their plane. This asymmetry can alter the IgG molecule's dipole moment. Within the Fab regions, the non-crystallographic symmetry axes of the V_L, V_H and C_L, and C_H1 domains may form varying angles, further modifying the molecular dipole moment.

 https://www.doi.org/10.33910/2687-153X-2025-6-2-69-86

These observations demonstrate that the IgG molecule exhibits multiple forms of intramolecular motion across its quaternary, tertiary, secondary, and primary structural elements. These dynamic modes can overlap, giving rise to a broad, composite relaxation process.

Identification of processes

According to established methodology (Gorokhovatskiy et al. 2013, 93), there exist three types of relaxation processes: α, β, and γ. The α-process corresponds to dipole-segmental motion, while β and γ processes represent dipole-group motions. The kinetic units differ for each process type. For the α-process, the kinetic units consist of whole molecules or large segments corresponding to tertiary structural elements. The β-processes involve large polar groups of molecules that vary in size and mass, such as α-helices or β-sheets. The γ-processes are characterized by small polar groups of molecules, including amino acid residues. When different processes possess kinetic units of similar characteristics, they may merge, leading to broadening of the dielectric spectrum. A broad relaxation process typically contains multiple subprocesses: α_1, α_2, α_3 and so on for the α-process and β_1, β_2, β_3 and so on for the β-process. Each subprocess exhibits its own characteristic relaxation time and contributes to the overall observed relaxation behavior (Bartenev, Barteneva, 1992).

In our case, we observe three processes with characteristic relaxation times: I-process $\tau_{0\_1} \approx 10^{-2}$ s., II-process $\tau_{0\_2} \approx 10^{-4}$ s., III-process $\tau_{0\_3} \approx 10^{-6}$ s. We propose that process I is an α-process, while process III corresponds to a β-process. This assignment is justified by their four-order-of-magnitude separation in relaxation times. Furthermore, we suggest that process II may also be classified as a β-process. This interpretation is supported by the temperature-frequency dependence of $tg\delta(f,T)$ shown in Figure 1, where processes II and III appear in close proximity, exhibiting mutual overlap and collectively forming local maxima and minima. Additional evidence comes from Figure 3, which shows increased ε'' values at both low (0.1–1 Hz) and high (5–15 MHz) frequency ranges. We attribute these features to the emergence of additional relaxation processes: potentially another α-process at low frequencies and an additional β-process at high frequencies.

The first relaxation process

The first relaxation process (I) appears in the temperature range T = 35–39.7 °C within the frequency domain f = 1–100 Hz (Figs. 4, 5). The maximum value of $\varepsilon''(f) \approx 0.7$ is observed at $f \approx 10$ Hz. Figure 13 presents the temperature evolution of relaxation parameters $\alpha_1(T)$ and $\beta_1(T)$ for this process. These dependencies likely reflect conformational changes occurring in the kinetic units responsible for process I.

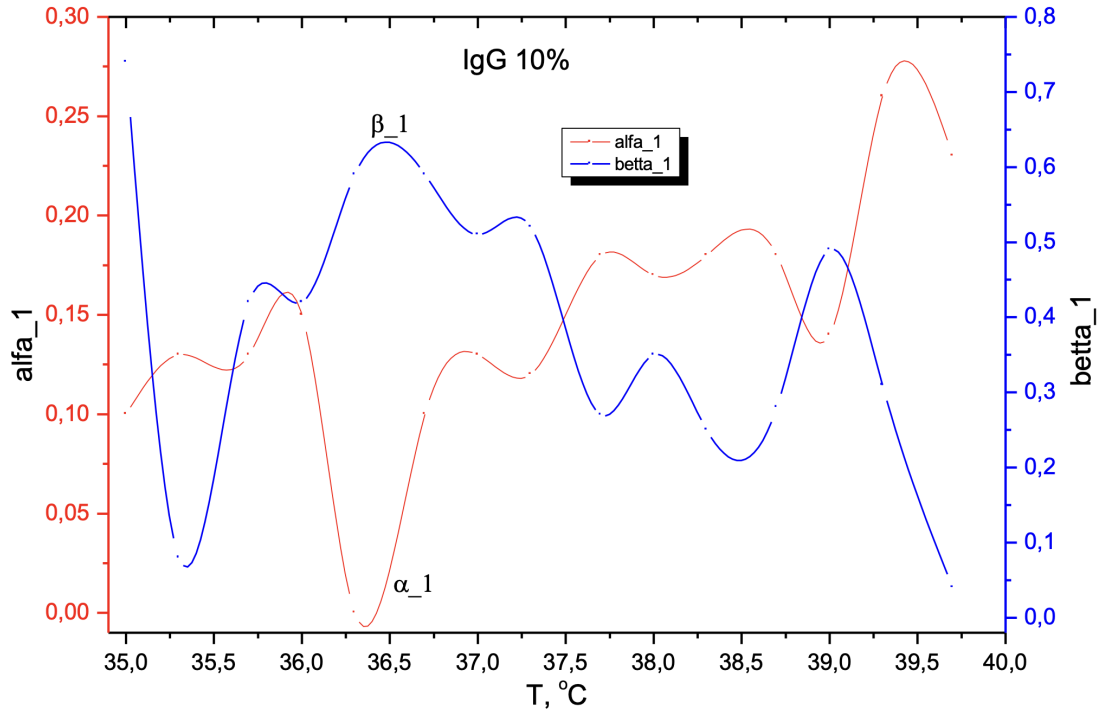

Fig. 13. Temperature dependences of relaxation parameters $\alpha_1(T)$ and $\beta_1(T)$ for the first relaxation process

It can be seen that the minima of $\alpha_1(T)$ correspond to the maxima of $\beta_1(T)$ and vice versa. This reciprocal relationship suggests a connection between these parameters. At T = 36.3 °C, this behavior is particularly evident, with α_1 reaching its minimum (α_1 = 0) and β_1 attaining its maximum (β_1 = 0.6). The decrease in α_1 reflects reduced heterogeneity in the sizes and shapes of kinetic units. Concurrently, the elevated β_1 value indicates highly pronounced cooperative motion, where the rotational probability of a kinetic unit becomes strongly dependent on neighboring unit orientations. This simultaneous minimization of α_1 and maximization of β_1 likely signify substantial conformational changes in the kinetic units associated with the first relaxation process. Such changes may potentially involve phase transitions, including globule-to-coil transformations.

The relatively long relaxation time ($<\tau_{01}> = 3.1 \times 10^{-2}$ s) indicates that the kinetic units of the first process must be either complete IgG molecules or substantial segments of the tertiary structure, particularly the Fab and Fc fragments. This would classify the first relaxation process as dipole-segmental motion (α-process). To identify the specific structural elements involved, we examine Figure 3, which reveals increased $\varepsilon''(f)$ in the 0.1–1 Hz range. This low-frequency enhancement likely represents an additional relaxation process rather than conductivity effects, suggesting that rotation of entire IgG molecules occurs at even lower frequencies. Consequently, complete IgG molecules cannot be the kinetic units for the first process. We therefore propose that Fab and Fc fragments serve as the kinetic units, with the observed conformational changes arising from modifications in their spatial configuration. The limited response of these fragments to alternating electric fields is evidenced by the modest dielectric loss peak $\varepsilon''(f) \approx 0.7$ (Fig. 3) and the slight polarization change $\Delta\varepsilon'(f) \approx 84 - 83 = 1$ (Fig. 2). This constrained mobility stems from several factors. Fab and Fc fragments approximate rotation ellipsoids (~80×40 Å) with restricted conformational freedom, their relative positions are stabilized by both quaternary structure maintenance forces and strong intermolecular interactions in aqueous environments, and their substantial size combined with extensive hydrogen bonding to surrounding water molecules severely limits rotational freedom.

The relaxation time distribution function $G(\tau)$ (Fig. 11) was decomposed into constituent processes, with the component corresponding to the first process displayed in Figure 14.

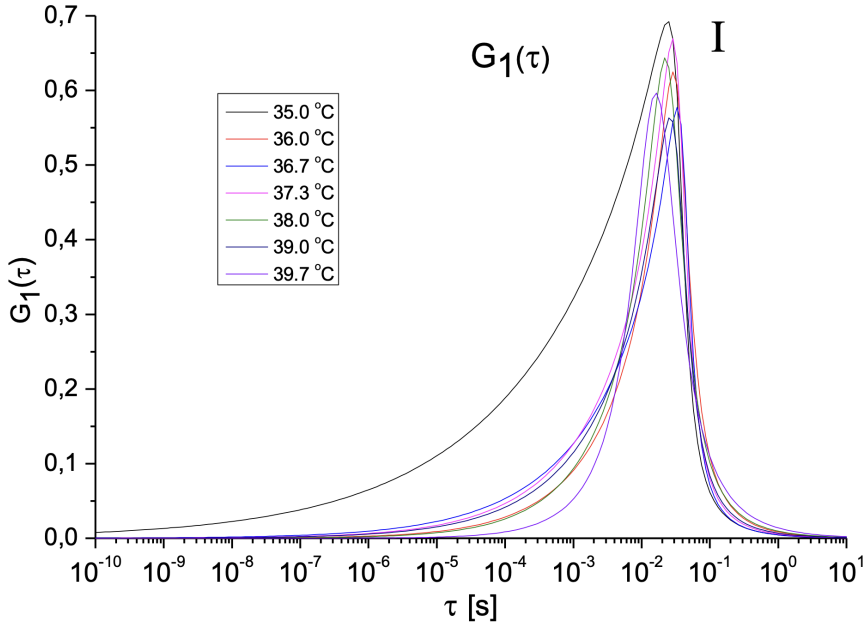

Fig. 14. Relaxation time distribution function $G(\tau)$ for the first relaxation process at various temperatures

The distribution function $G(\tau)$ for the first relaxation process exhibits pronounced asymmetry, as evidenced by β_1 = 0.25–0.74 The distribution spans six frequency decades (10^{-6} to 1 s), indicating considerable breadth. At 35 °C, $G(\tau)$ shows distinct behavior, which correlates with the exceptionally high β_1 = 0.74 observed at this temperature. This anomalous behavior may signal the onset of an additional relaxation process, though investigation of lower temperature data would be required for definitive analysis.

 https://www.doi.org/10.33910/2687-153X-2025-6-2-69-86

The second relaxation process

The second relaxation process (II) occurs in the temperature range T = 35–39.7 °C within the frequency domain f = 100 Hz–10 kHz (Figs. 6, 7). The maximum value of $\varepsilon''(f) \approx 2$–2.5 is observed at $f \approx 3$ kHz emerging at temperatures $T \geq 36.7$ °C. The peak magnitude shows temperature dependence, increasing from $\varepsilon'' = 1.5$ at $T = 36.7$ °C to $\varepsilon'' = 2.6$ at $T = 39.7$ °C. Figure 15 shows the temperature evolution of relaxation parameters $\alpha_2(T)$ and $\beta_2(T)$ for process II, which likely reflects conformational changes in the associated kinetic units.

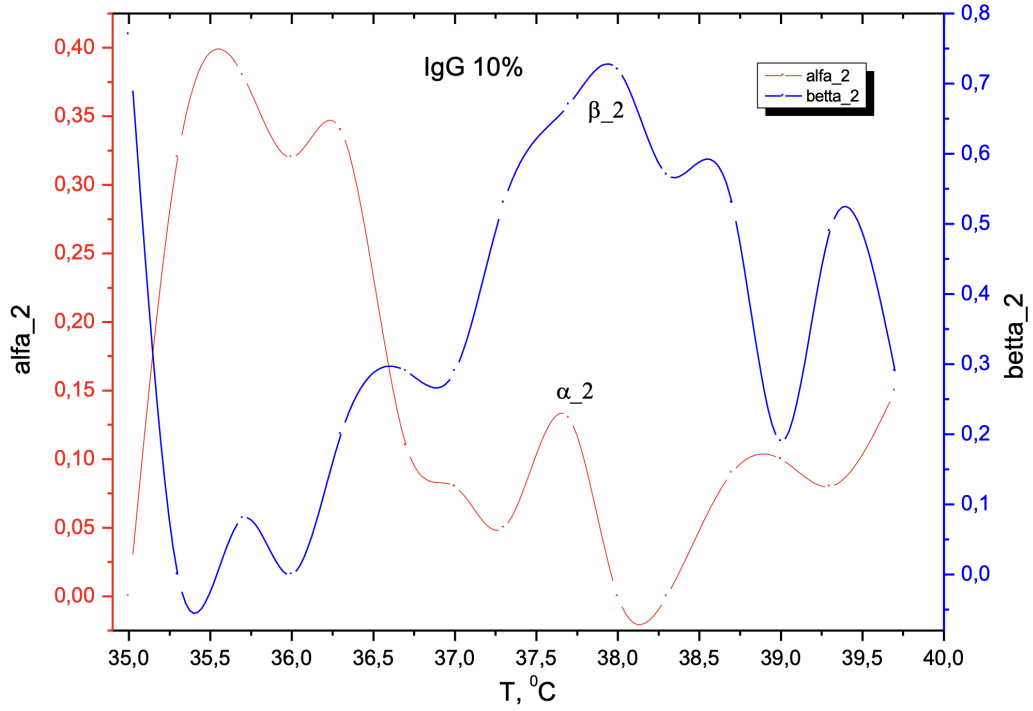

Fig. 15. Temperature dependences of relaxation parameters $\alpha_2(T)$ and $\beta_2(T)$ for the second relaxation process

In the temperature range T = 36.7–39.7 °C, this process has a very narrow ($\alpha_2 \approx 0.1$) and asymmetric ($\beta_2 \approx 0.3$–0.7) relaxation spectrum. A particularly notable behavior occurs at 38–38.3 °C, where α_2 reaches zero while β_2 peaks at 0.72, signaling substantial conformational changes in the kinetic units that may involve phase transitions. Figure 15 reveals another significant feature at $T \approx 36$ °C, where α_2 attains its maximum value ($\alpha_2 \approx 0.4$) while β_2 drops to its minimum ($\beta_2 = 0$). This relationship indicates independent rotation of kinetically distinct units. The co-occurrence of maximal α_2 and minimal β_2 values likely reflects another regime of pronounced conformational changes in the kinetic units. These observations suggest that the temperature dependence of $\alpha_2(T)$ and $\beta_2(T)$ reflects conformational dynamics in process II.

The function $G(\tau)$ for process II is shown in Figure 16.

The temperature-dependent evolution of the relaxation function $G(\tau)$ reveals significant conformational changes in the kinetic units of the second process, particularly evident at 35 and 38 °C where the distribution shifts markedly. Across the studied temperature range, $G(\tau)$ for this process spans four frequency decades (10^{-7}–10^{-3} s), notably narrower than the six-decade breadth observed for the first relaxation process (Fig. 14). The shorter characteristic relaxation times ($\langle\tau_{0\_2}\rangle \approx 10^{-4}$ s versus $\langle\tau_{0\_1}\rangle \approx 3 \times 10^{-2}$ s) suggest the second process involves smaller structural elements than the Fab and Fc fragments responsible for the first process. The close correlation between the second and third processes (Figs. 6, 7, 11), evidenced by the temperature-dependent transition of their spectral maxima, indicates they share a common physical origin. We propose these processes represent distinct subcomponents (β_1, β_2) of a unified β-process arising from the relative motion of individual IgG domains (Fig. 12). This intramolecular motion can be understood as internal rotation of structural units (Orville-Thomas 1974), where the β-sheet-rich domains (Finkelstein 2014) undergo dipole-group movements.

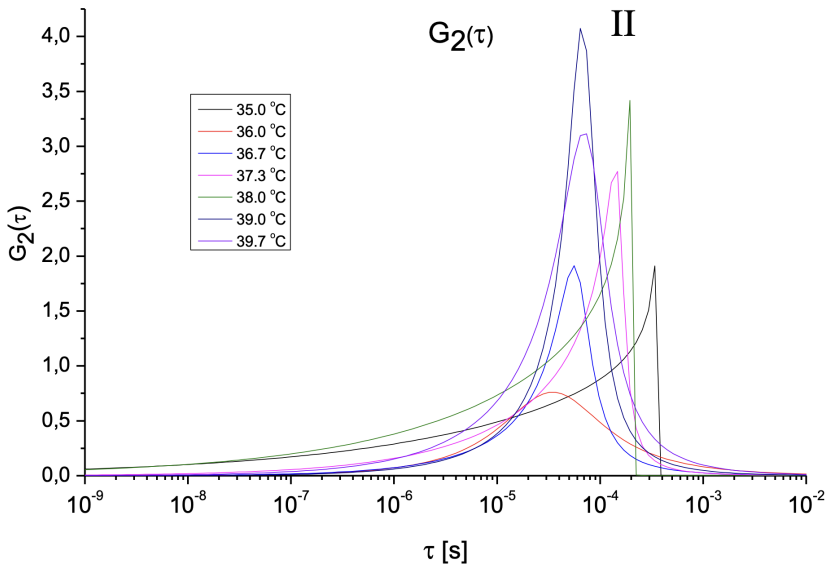

Fig. 16. The time distribution function of the relaxers $G(\tau)$ for the second relaxation process at different temperatures

The third relaxation process

The third relaxation process (III) appears in the temperature range T = 35–39.7 °C within the frequency domain f = 10 kHz–1 MHz (Figs. 6, 7). This process exhibits a dielectric loss peak $\varepsilon''(f) \approx 1.5$–$1.9$ between 35.0 and 38.0 °C, centered at $f \approx$ 30–100 kHz. At $T \geq$ 38.0 °C (excluding T = 39.0 °C), this peak transforms into an inflection point. The ε'' maximum displays complex temperature dependence: it initially increases (35.0 °C ≤ T ≤ 36.3 °C), then decreases (36.3 °C ≤ T ≤ 37.3 °C), before increasing again (37.3 °C ≤ T ≤ 39.7 °C).

Figure 17 shows the temperature evolution of relaxation parameters $\alpha_3(T)$ and $\beta_3(T)$ for process III.

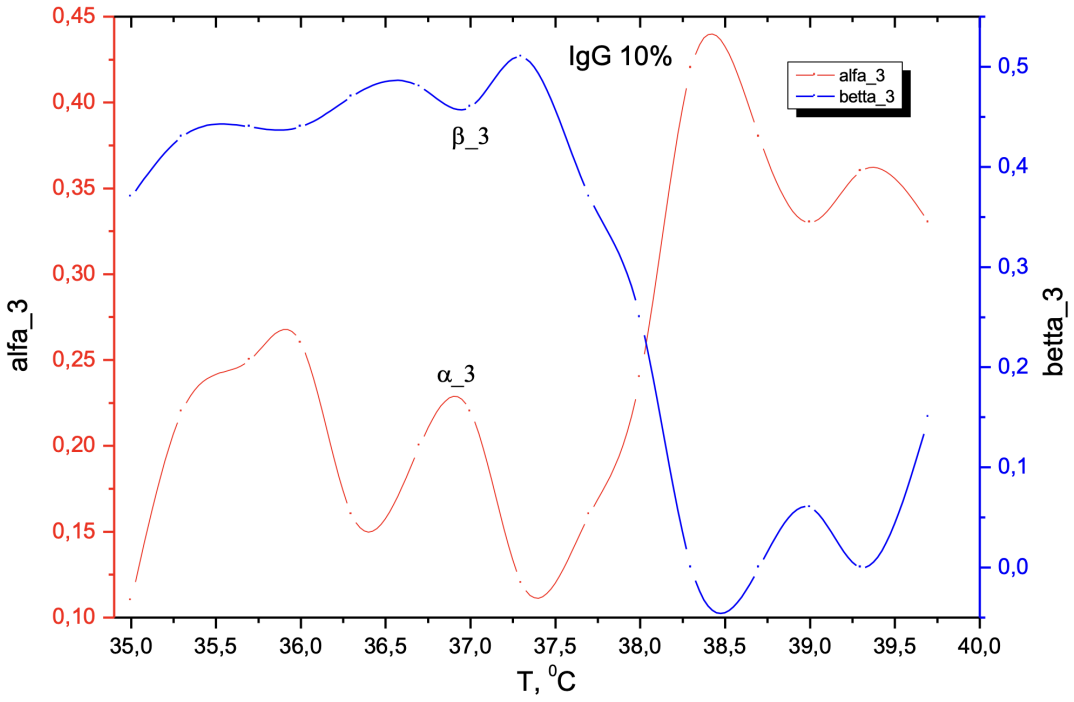

Fig. 17. Temperature dependences of relaxation parameters $\alpha_3(T)$ and $\beta_3(T)$ for the third relaxation process

https://www.doi.org/10.33910/2687-153X-2025-6-2-69-86

The parameter α_3 shows two distinct minima, α_3 = 0.16 at T = 36.3 °C and α_3 = 0.12 at T = 37.3 °C, corresponding to β_3 maxima of 0.47 and 0.51 respectively. A prominent α_3 maximum of $\alpha_3 \approx 0.44$ occurs at $T \approx$ 38.4 °C, accompanied by vanishing (β_3 = 0.0) at T = 38.3–38.7 °C. These parameter variations signify substantial conformational rearrangements in the kinetic units of process III within this temperature range.

The relaxation time distribution function $G(\tau)$ for process III is shown in Figure 18. The distribution spans five decades of frequency (10^{-9}–10^{-4} s), exhibiting greater breadth and symmetry compared to process II (Fig. 18).

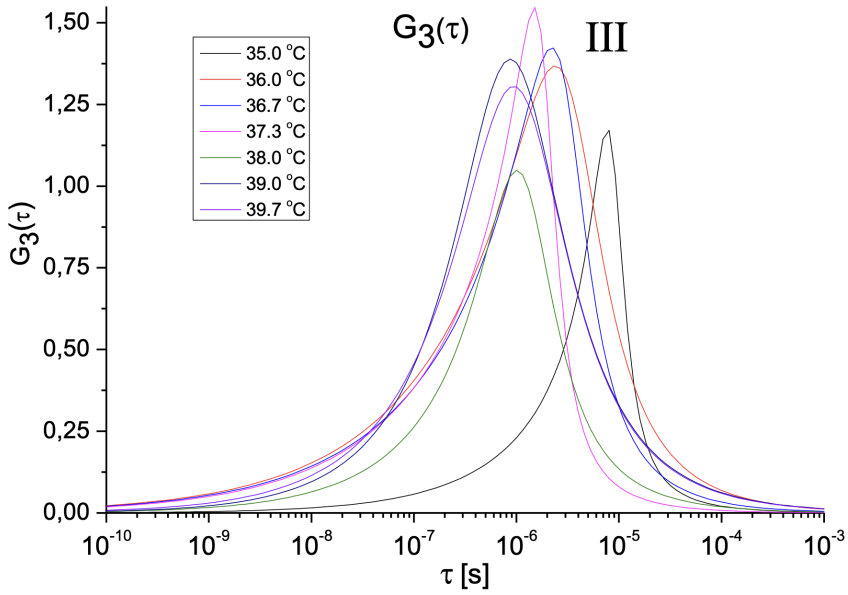

Fig. 18. The time distribution function of the relaxers $G(\tau)$ for the third relaxation process at different temperatures

As proposed, both the second and third relaxation processes originate from domain motions within the IgG molecule (Fig. 12). However, the third process exhibits significantly shorter relaxation times ($<\tau_{0\_3}> \approx 3 \times 10^{-6}$ s) compared to the second process ($<\tau_{0\_2}> \approx 10^{-4}$ s), reflecting differences in domain size, mass, and intramolecular interactions, as well as available free volume for movement. While Fab fragments contain free volume between the $V_L V_H$ and $C_L C_H 1$ domains enabling larger-scale motions (Fig. 12), the Fc fragment lacks comparable space between $C_H 2$ and $C_H 3$ domains. Thus, the second process involves more extensive domain movements, while the third process consists of restricted, smaller-scale motions. These differences manifest clearly in the relaxation spectra (Figs. 6, 7), with the second process appearing as a stronger, narrower peak compared to the broader, weaker third process. Quantitative analysis in Table 1 confirms this distinction, with the third process showing nearly double the α parameter ($<\alpha_3>$ = 0.25 vs $<\alpha_2>$ = 0.14) and reduced cooperativity ($<\beta_3>$ = 0.29 vs $<\beta_2>$ = 0.37).

The broad, asymmetric $G(\tau)$ distributions and large α and β values across all three processes reveal the IgG molecule's complex dynamics, featuring multiple motional scales with distinct activation barriers and characteristic times — a hallmark of protein behavior that can be described as a set of dielectric permittivity with discreet time constants each (Krishtalik 2012).

Possible phase transitions

The anomalous shapes of the relaxation time distribution functions $G(\tau)$ for all three processes (Figs. 19–21) show marked deviations from their typical forms at other temperatures (cf. Figs. 14, 16, 18).

These distinctive profiles, while all resembling the Cyrillic letter 'Л', demonstrate significant variations in their specific forms — particularly in how abruptly the functions terminate at longer τ values. The corresponding relaxation parameters α and β for these anomalous cases, extracted from Table 1, are presented in Table 2.

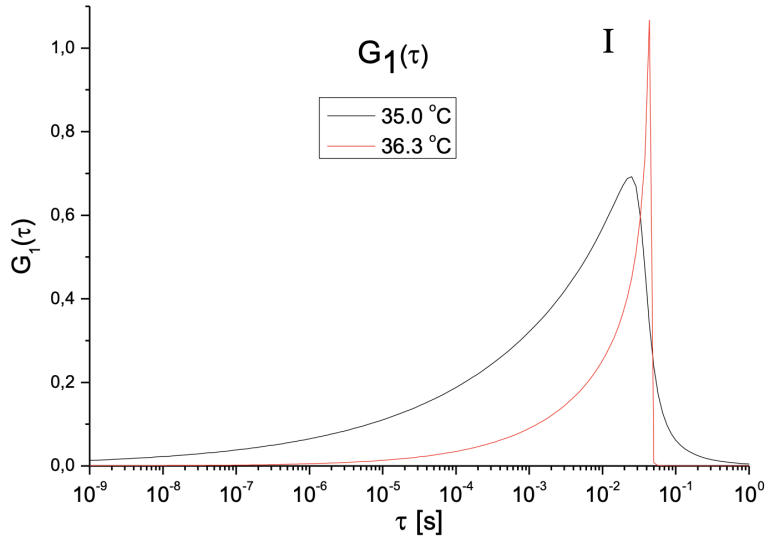

Fig. 19. $G_1(\tau)$ at T = 35.0, 36.3 °C

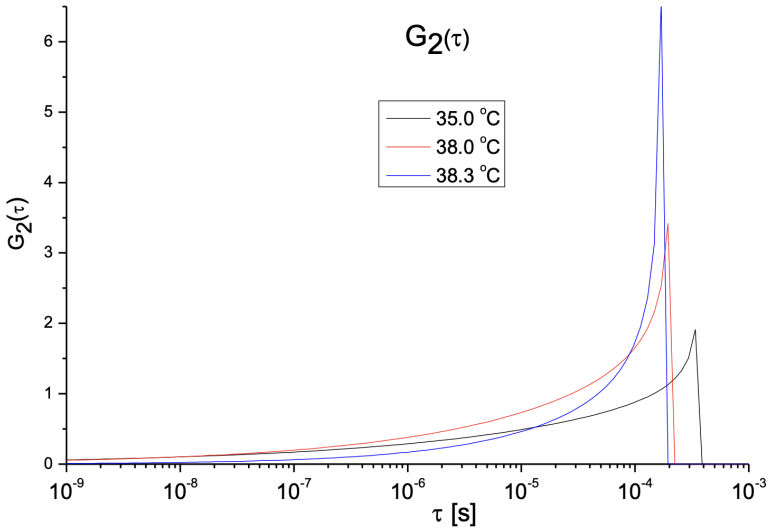

Fig. 20. $G_2(\tau)$ at T = 35.0, 38.0, 38.3 °C

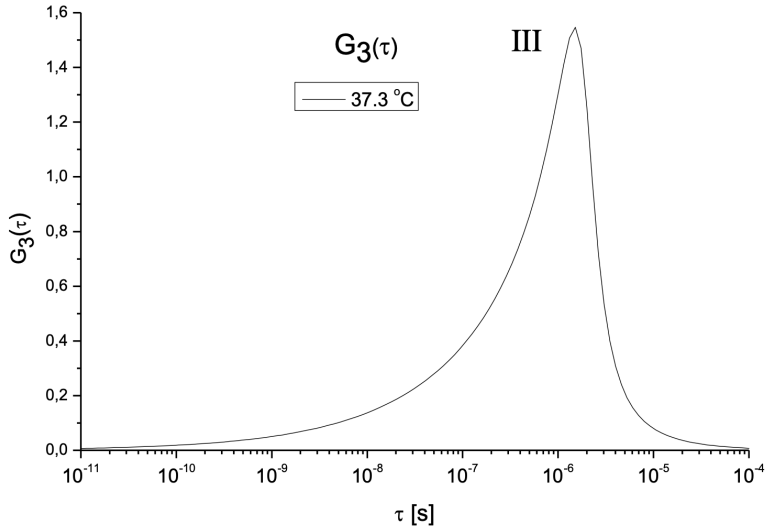

Fig. 21. $G_3(\tau)$ at T = 37.3 °C

https://www.doi.org/10.33910/2687-153X-2025-6-2-69-86

Table 2. Values of relaxation parameters α and β for Figs. 19–21

T, °C	The first relaxation process: f = 1–100Hz		The second relaxation process: f = 100 Hz–10 kHz		The third relaxation process: f = 10kHz–1 MHz	
	α_1	β_1	α_2	β_2	α_3	β_3
35.0	0.10	0.74	0.00	0.77		
36.3	0.00	0.59				
37.3					0.12	0.51
38.0			0.00	0.72		
38.3			0.00	0.57		

The abrupt termination of $G(\tau)$ functions, as observed in Figs. 19–21 ($G_1(\tau)$ at T = 36.3 °C, $G_2(\tau)$ at T = 35.0, 38.0, 38.3 °C), correlates with two key parameter changes: α approaches zero, while β reaches local maxima (Table 1). This behavior — manifested as a sharp cutoff resembling the Cyrillic 'Л' shape — suggests the occurrence of a broad phase transition within the T = 38.0–38.3 °C temperature range.

We propose that such truncated $G(\tau)$ profiles, accompanied by $\alpha \to 0$ and β maxima, serve as distinctive signatures of phase transitions, where the β magnitude and distribution width (e. g., full width at half maximum) may quantify transition parameters.

Other $G(\tau)$ shapes, like $G_1(\tau)$ at T = 35.0 °C (Fig. 19) or $G_3(\tau)$ at T = 37.3 °C (Fig. 21), likely reflect substantial conformational changes in kinetic units without constituting true phase transitions.

The theoretical framework for conformational changes and phase transitions in biopolymers has been extensively developed in several monographs (Birshtein, Ptitsyn 1964; Flory 1969; Dashevsky 1987; Grosberg, Khokhlov 1989). The complexity of characterizing these transitions is exemplified by the ongoing debate regarding the classification of the globule-coil transition — while rigid chains exhibit abrupt, first-order transition behavior, flexible chains demonstrate smoother, second-order transitions (Grosberg, Khokhlov 1989, 146).

Recent investigations have employed complementary approaches to study these phenomena: the Shadrin group at Ioffe Institute analyzed the globule-coil transition in albumin through critical exponents (Vonti et al. 2018), while our team (Salnikova et al., 2025) examined the same system via relaxation parameters (α, β) and $G(\tau)$ characteristics. Our studies of 20% aqueous albumin solutions revealed signature behavior during the first relaxation process at T = 37 °C — α_2=0, maximal β_2 (0.74), and abrupt termination of $G_2(\tau)$ (similar to Fig. 20) — which we interpret as markers of a molecular phase transition.

A qualitative explanation of the detected processes

The physical nature of these relaxation processes stems from temperature-dependent modifications in both intramolecular motions and solvent interactions within the IgG system. As temperature changes, conformational rearrangements occur in various structural elements of the IgG molecule while its interactions with the aqueous environment simultaneously evolve. These alter the dipole-dipole interaction energies, which scale with the squares of the constituent dipole moments (Kaplan 1982, 17). The modified interaction energies change the local electric fields experienced by each kinetic unit, thereby affecting their rotational response to external fields. This directly determines the characteristic temperature and frequency dependences observed in ε' and ε'' components.

Conclusions

Our dielectric spectroscopy study of a 10% aqueous human IgG solution at physiological temperatures identified three characteristic relaxation processes with well-defined parameters. The dominant relaxation (process I) corresponds to the rotational motion of Fab and Fc fragments under the applied alternating electric field, while processes II and III, sharing a common physical origin, reflect intramolecular domain movements within these structural elements.

The temperature-dependent behavior of the relaxation parameters α and β provides new insights into conformational changes of the kinetic units, with the characteristic combination of α approaching zero while β reaches maximum values serving as a potential indicator of phase transitions.

The dielectric spectroscopy approach proves particularly valuable for such investigations due to its inherent sensitivity to dipole moment variations, conformational changes in structural subunits, and modifications in intermolecular interactions within the aqueous environment. This methodology offers a powerful tool for probing relaxation mechanisms in complex fluids, including biological ones.

Conflict of Interest

The authors declare that they have no conflict of interest.

Author Contributions

All the authors discussed the final work and took their respective part in writing the article.

References

Annus, P., Min, M. (eds.). (2021) *Bioimpedance and Spectroscopy*. New York: Academic Press, 454 p. (In English)

Bartenev, G. M., Barteneva, A. G. (1992) *Relaksatsionnye svojstva polimerov [Relaxation properties of polymers]*. Moscow: Khimiya Publ., 384 p. (In Russian)

Birshtein, T. M., Ptitsyn, O. B. (1964) *Konformatsii makromolekul [Conformations of macromolecules]*. Moscow: Nauka Publ., 392 p. (In Russian)

Blythe, T., Bloor, D. (2005) *Electrical properties of polymers*. 2nd ed. Cambridge: Cambridge University Publ., 506 p. (In English)

Borisova, M. E., Kojkov, S. N. (1979) *Fizika dielektrikov [Physics of dielectrics]*. Leningrad: Leningrad State University Publ., 240 p. (In Russian)

Dashevsky, V. G. (1987) *Konformatsionnij analiz makromolekul [Conformational analysis of macromolecules]*. Moscow: Nauka Publ., 288 p. (In Russian)

Finkelstein, A. V. (2014) *Fizika belkovykh molekul [Physics of protein molecules]*. Moscow; Izhevsk: Institute of Computer Research Publ., 424 p. (In Russian)

Flory, P. J. (1969) *Statistical mechanics of chain molecules*. New York; London; Sydney; Toronto: John Wiley & Sons Publ., 440 p. (In English)

Fröhlich, H. (1958) *Theory of dielectrics. Dielectric constant and dielectric loss. 2nd ed*. Oxford: Clarendon Press, 194 p. (In English)

Gorokhovatskiy, Yu. A., Karulina, E. A., Temnov, D. E. (2013) *Fizika polimernikh dielektrikov [Physics of polymer dielectrics]*. Saint Petersburg: Herzen State Pedagogical University of Russia Publ., 124 p. (In Russian)

Gotlib, Y. I., Darinskj, A. A., Svetlov, Yu. E. (1986) *Fizicheskaya kinetika makromolekul [Physical kinetics of macromolecules]*. Leningrad: Khimiya Publ., 272 p. (In Russian)

Grosberg, A. Yu., Khokhlov, A. R. (1989) *Statisticheskaya fizika makromolekul [Statistical physics of macromolecules]*. Moscow: Nauka Publ., 344 p. (In Russian)

Kaplan, I. G. (1982) *Vvedenie v teoriyu mezhmolekularnykh vzaimodejstvij [Introduction to the theory of intermolecular interactions]*. Moscow: Nauka Publ., 312 p. (In Russian)

Kremer, F., Schönhals, A. (eds.). (2003) *Broadband dielectric spectroscopy*. Berlin; Heidelberg: Springer Publ., 729 p. https://doi.org/10.1007/978-3-642-56120-7 (In English)

Krishtalik, L. I. (2012) Belki kak spetsificheskaya polyarnaya sreda protsessov perenosa zaryada [Proteins as a specific polar medium of charge transfer processes]. *Uspexi Fizicheskix Nauk — Physics–Uspekhi*, 182 (12), 1275–1300. https://doi.org/10.3367/UFNr.0182.201212b.1275 (In Russian)

Litman, G. W., Good, R. A. (eds.) (1978) *Immunoglobulins*. New York; London: Plenum Medical Book Company Publ., 410 p. (In English)

Orville-Thomas, W. J. (ed.). (1974) *Internal rotation in molecules*. New York; London; Sydney; Toronto: John Wiley & Sons Publ., 606 p. (In English)

Raicu, V., Feldman, Y. (eds.). (2015) *Dielectric Relaxation in biological systems: Physical principles, methods, and applications*. Oxford: Oxford University Press, 388 p. (In English).

Salnikova, Zh. A., Kononov, A. A. (2020) Derivation of the Havriliak—Negami equation for the complex electrical modulus. *AIP Conference Proceedings*, 2308 (1), 030017. https://doi.org/10.1063/5.0034028 (In English)

Salnikova, Zh. A., Kononov, A. A., Smirnov, A. P., Castro, R. A. (2025) Shirokopolosnaya dielektricheskaya spektroskopiya rastvora albumina cheloveka pri fiziologicheskikh temperaturakh [Broadband dielectric spectroscopy of human albumin solution at physiological temperatures]. *Zhurnal Tekhnicheskoj fiziki — Technical Physics*, 95 (6), 1224–1233. https://doi.org/10.61011/JTF.2025.06.60474.427-24 (In Russian)

Sazhin, B. I. (1986) (ed.). *Elektricheskie svojstva polimerov [Electrical properties of polymers]*. 3rd ed. Leningrad: Khimiya Publ., 224 p. (In Russian)

Vonti, A. O., Ilyinsky, A. V., Kapralova, V. M., Shadrin, E. B. (2018) Kompleksnaya priroda termicheskikh fazovykh prevraschenij v rastvorakh al'bumina [The complex nature of thermal phase transformations in albumin solutions]. *Zhurnal Tekhnicheskoj fiziki — Technical Physics*, 88 (6), 934–942. (In Russian)

Physics of Semiconductors. Structure of solids

UDC 538.958

EDN QUWZMD
https://www.doi.org/10.33910/2687-153X-2025-6-2-87-92

Laser modification of PbSe chalcogenide films via LIPSS formation

A. D. Dolgopolov ✉[1], A. A. Olkhova [1], M. M. Sergeev [1], P. P. Omelchenko [1], B. G. Shulga [1], M. K. Moskvin [1], A. A. Patrikeeva [1], V. R. Gresko [1]

[1] National Research University ITMO, 49 Kronverksky Ave., Saint Petersburg 197101, Russia

Authors

Arthur D. Dolgopolov, ORCID: 0000-0002-9548-791X, e-mail: adddolgopolov@itmo.ru

Anastasiia A. Olkhova, ORCID: 0000-0001-9048-3031, e-mail: olkhova.a.a@mail.ru

Maksim M. Sergeev, ORCID: 0000-0003-2854-9954, e-mail: maxim.m.sergeev@gmail.com

Pavel P. Omelchenko, e-mail: 336882@niuitmo.ru

Bogdan G. Shulga, e-mail: swim-12@mail.ru

Mikhail K. Moskvin, ORCID: 0000-0001-7399-7022, e-mail: mkmoskvin@itmo.ru

Alina A. Patrikeeva, ORCID: 0000-0002-5274-9692, e-mail: patrikeeva17@gmail.com

Vladislav R. Gresko, ORCID: 0000-0003-3308-6034, e-mail: gresko.97@mail.ru

For citation: Dolgopolov, A. D., Olkhova, A. A., Sergeev, M. M., Omelchenko, P. P., Shulga, B. G., Moskvin, M. K., Patrikeeva, A. A., Gresko, V. R. (2025) Laser modification of PbSe chalcogenide films via LIPSS formation. *Physics of Complex Systems*, 6 (2), 87–92. https://www.doi.org/10.33910/2687-153X-2025-6-2-87-92 EDN QUWZMD

Received 22 November 2024; reviewed 29 March 2025; accepted 30 March 2025.

Funding: This research was funded by the Russian Science Foundation grant and a grant from the St. Petersburg Science Foundation (project no. 23-29-10081).

Abstract. The study investigates the laser modification of lead selenide (PbSe) chalcogenide films with the formation of laser-induced periodic surface structures (LIPSS). These modifications are crucial for enhancing the sensitivity of gas analyzers, particularly in detecting hazardous gases in various industries. The use of nanosecond laser pulses for film processing offers improved productivity, better reproducibility, and greater control over optical properties compared to conventional furnace annealing techniques. The formation of LIPSS under specific laser irradiation conditions leads to changes in the film's optical characteristics, including increased absorption in the infrared (IR) range. Additionally, the study examines the dependence of the periodicity of these structures on the power density of the applied laser radiation. The findings highlight the potential of laser modification for creating new optical properties and developing innovative photonics devices.

Keywords: PbSe films, laser modification, optical characteristics, nanosecond laser pulses, laser-induced periodic surface structures (LIPSS)

Introduction

Laser-induced periodic surface structures (LIPSS) have emerged as a powerful tool for modifying the surface properties of materials, enabling precise control over optical, mechanical, and chemical characteristics (Bonse 2020). These nanostructures, typically formed through the interaction of laser radiation with a material's surface, have found applications in a wide range of fields, including photonics, tribology, and biomedicine (Antipov et al. 2012; Bonse 2020). The ability to tailor surface properties at the micro- and nanoscale makes LIPSS particularly attractive for developing advanced optical devices, sensors, and functional coatings.

One of the key advantages of LIPSS is their ability to enhance optical properties of materials, such as increasing absorption in specific wavelength ranges or creating diffraction effects. This is especially relevant for materials like lead selenide (PbSe), which exhibit high photosensitivity in the infrared (IR) range (Tan, Mohseni 2018). PbSe films, widely used in photodetectors and gas sensors, can benefit significantly from laser-induced modifications (Nielsen et al. 2023; Peng et al. 2022). Conventional furnace annealing of PbSe films is hindered by high defect densities, elevated production costs, and poor process repeatability. These limitations have motivated the development of laser-based surface modification techniques as a promising alternative (Tan, Mohseni 2018).

The formation of LIPSS on PbSe films not only enhances their IR absorption, but also opens up new possibilities for creating innovative photonic devices, such as diffraction elements and sensors with tailored optical responses (Gupta et al. 2021). Compared to conventional furnace annealing, LIPSS formation can significantly improve reproducibility and offer more dynamic control over the material's optical properties (Nielsen et al. 2023; Olkhova et al. 2023).

In this study, we investigate the formation of LIPSS on PbSe chalcogenide films using nanosecond laser pulses. The focus is on understanding the mechanisms behind LIPSS formation and their impact on the optical properties of films. By exploring the relationship between laser parameters (e. g., power density, pulse duration) and the resulting surface structures, we aim to demonstrate the potential of laser modification for developing new optical materials and devices. This work highlights the broader applicability of LIPSS in material science and photonics, paving the way for future advancements in surface engineering and optical technology. The formation of LIPSS on the surface of PbSe films can allow more controlled modification of the material and obtain new optical properties (Nykyruy et al. 2019; Olkhova et al. 2022), as well as the creation of diffraction elements by direct laser writing, which represents the potential for the creation of new photonics devices.

Materials and methods

The 0.6 μm thick polycrystalline PbSe films used in this work were created by vacuum-thermal sputtering on a plane-parallel substrate made of 0.2 mm thick cover glass. The film samples were fabricated by Optosens LLC, Russia.

Laser modification of the structure and properties of the films was performed by nanosecond pulses of a fiber Yb laser based on the Minimarker-2 complex (Laser Center LLC, Russia) with a wavelength of 1064 nm and a Gaussian profile of energy distribution in the beam cross-section. Spot's movement was controlled using a two-mirror galvanometer scanner. After the scanner mirrors, the beam was focused by an F-theta lens with a processing field of 100x100 mm on the film surface, where the spot diameter was 50 μm. The polarization of the radiation incident on the sample was adjusted using a Glan-Taylor prism and a half-wave phase plate (Fig. 1). The following parameters were used to determine the modes of LIPPS formation: pulse duration (from 14 to 100 ns), average power (from 100 to 500 mW), and pulse repetition rate (from 30 to 140 kHz). At the same time, the laser spot scanning speed remained unchanged and equal to 15 mm/s, which provided an overlap of more than 0.99. The modes of sample modification using laser radiation are presented in Table 1.

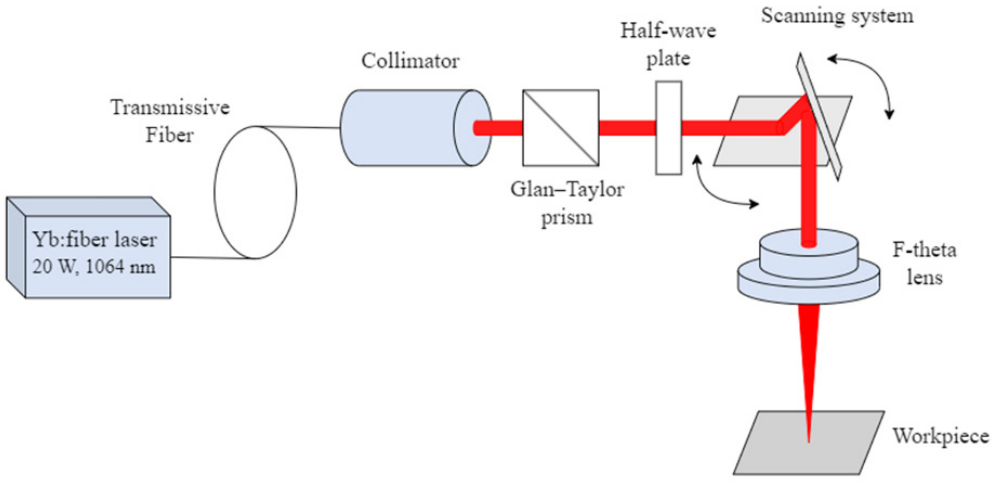

Fig. 1. Schematic diagram of the experimental setup for laser processing of chalcogenide films with LIPPS formation

 https://www.doi.org/10.33910/2687-153X-2025-6-2-87-92

Table 1. Modification modes of chalcogenide film using a pulsed laser source with a wavelength of 1064 nm

No	Pulse duration, ns	Frequency, kHz	Average power, W	Power density, kW/cm²
1	100	60	0.271	11.81
2	50	90	0.299	13.52
3	20	90	0.29	16.77

The structures obtained on the sample were investigated by optical microscopy in the light and dark fields of transmitted and reflected light using a Carl Zeiss Axio Imager microscope (Germany). Spectral reflection and transmittance of periodic structures in linearly polarized light at different angles of sample rotation were measured using a spectrophotometer MSFU-K Yu-30.54.072, LOMO (Russia) in the wavelength range between 380 and 900 nm. The period of the structures was determined via the analysis of optical microscopy data by two-dimensional fast Fourier transform (2D-FFT) using the open-source software Gwyddion (Version 2.62).

Scanning electron microscopy (SEM) was performed using a Merlin Zeiss high-resolution electron microscope (Germany) to evaluate the modification of the film structure after laser exposure.

Results and Discussion

Structure modification

In contrast to the traditional heat treatment in the furnace, the method of laser modification of the film structure is characterized by the localization of thermal influence with a high temperature gradient in the center and at the edges of the irradiation zone. During laser exposure, darkening of the film was observed due to changes in the intermolecular bonds of PbSe in the area of exposure (Olkhova et al. 2023). The darkening of the film led to an increase in the absorption capacity and thus to an increase in the fraction of the absorbed incident radiation energy, which influenced the temperature change in the laser-modified region.

Obtained LIPSS were investigated by optical microscopy and 2D-FFT. The formation of periodic structures, classified as Low Spatial-Frequency LIPSS (LSFL) (Bonse 2020), with a period of 0.7 ± 0.1 μm and with a period of 1.2 ± 0.2 μm (Fig. 2), occurred during laser exposure of the film.

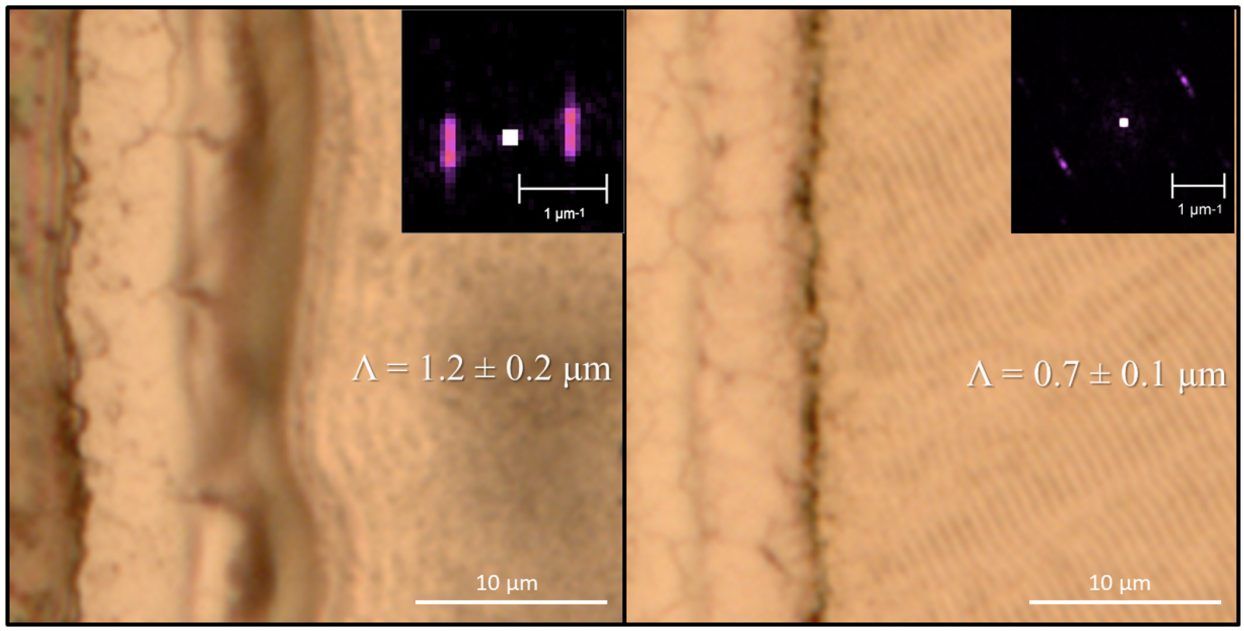

Fig. 2. Optical microscopy and 2D-FFT results of tracks exhibiting LIPSS with periods of 0.7 (power density of 16.77 kW/cm²) and 1.2 μm (power density of 11.81 kW/cm²)

The periodic structures with 0.7 μm spacing were formed in power density ranges of 14 kW/cm^2 and higher. At lower power densities in the range of 10 kW/cm^2 to 12 kW/cm^2, the structure period increased to 1.2 μm (Fig. 3)

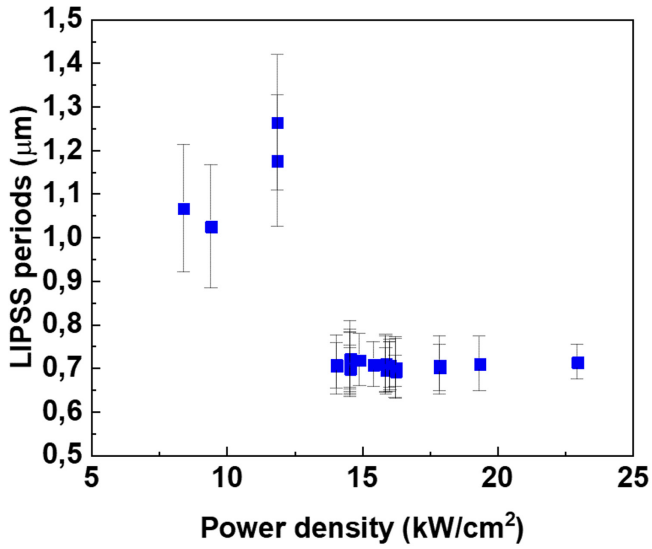

Fig. 3. Power density dependence of LIPSS periodicity

The formation of laser-induced periodic structures (LIPSS) on PbSe films under nanosecond exposure is associated with thermal and hydrodynamic processes depending on the laser power density. In the 'non-through oxidation' regime (7.5–12.5 kW/cm^2), the structures were formed predominantly at the edges of the laser exposure track, repeating its contour, with a period of 1.2 ± 0.2 μm. This is explained by local softening of the material, formation of a melt bath, and subsequent formation of a 'border' due to thermocapillary flows (Marangoni effect). Diffraction of laser radiation on edge rolls led to the formation of periodic structures parallel to the roll.

With increasing power density ('through oxidation' mode), the structures appeared across the entire track width, aligning with the laser radiation polarization and demonstrating a smaller period — 0.7 μm. This value agrees with the dependence $\Lambda \approx \lambda/n_{substr}$ (Bonse 2020), where n_{substr} = 1.5 for a glass substrate λ = 1064 nm, $\Lambda \approx$ 710 nm.

'Non-through oxidation' is characterized by the use of shorter nanosecond pulses and lower power density, at which LSFLs of a larger period are predominantly formed (Olkhova et al. 2023). Increasing the pulse duration as well as increasing the power density leads to a decrease in the LSFL period as a result of reaching 'through oxidation' (Olkhova et al. 2023).

Figure 4 shows photographs of the modified region. The structures have a period of 0.7 μm throughout the scanning track, which was confirmed by the 2D-FFT spectrum (Fig. 4a). When viewed in transmitted light, LSFLs formed on the initially opaque PbSe film can be seen, which confirms the assumption that 'through oxidation' was achieved during processing (Fig 4b). SEM results (Fig 4c) confirm inhomogeneous character of surface oxidation (Fig 4d).

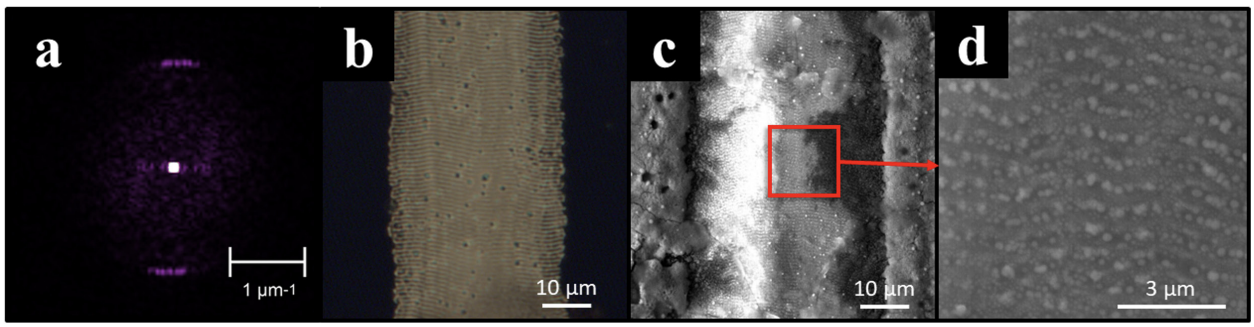

Fig. 4. (a) FFT spectrum of the LSFLs with Λ = 0.7 μm and their microphotographs obtained (b) by transmitted light optical microscopy and (c, d) by SEM (pulse duration 20 ns, frequency 90 kHz, power density 16.77 kW/cm^2)

https://www.doi.org/10.33910/2687-153X-2025-6-2-87-92

Optical properties

Following laser recording, the optical properties of the periodic structures were examined. Transmission and specular reflection spectra of linearly polarized light were measured at varying rotation angles of the structures.

The most significant angles were 0° and 90°, corresponding to orientations where the periodic structure lines were aligned parallel and perpendicular to the light polarization direction, respectively.

Reflectance spectra of the film before and after laser irradiation show that the reflectance of the modified region decreases due to laser exposure (Fig. 5). The spectra of modified LSFL regions with a period of 0.7 μm exhibit a rise in the 780–810 nm range and a dip in the short-wavelength region. When the period increases to 1.2 μm, the rise in the IR region vanishes, while reflection in the short-wavelength region increases. In all cases, reflection is higher when the polarization vector is aligned with the LSFL lines; rotating the polarization vector by 90° leads to a slight decrease in reflection across the entire measured spectrum. This spectral dependence arises from two factors: (1) the presence of submicron surface relief in the form of periodic structures and (2) a reduction in the refractive index of the near-surface PbSe film layer due to oxidation (Olkhova et al. 2023). The observed artificial anisotropy is a notable phenomenon, more commonly associated with femtosecond laser surface modification (Kolchin et al. 2022). Its occurrence after nanosecond pulsed treatment may suggest the induction of phase transitions.

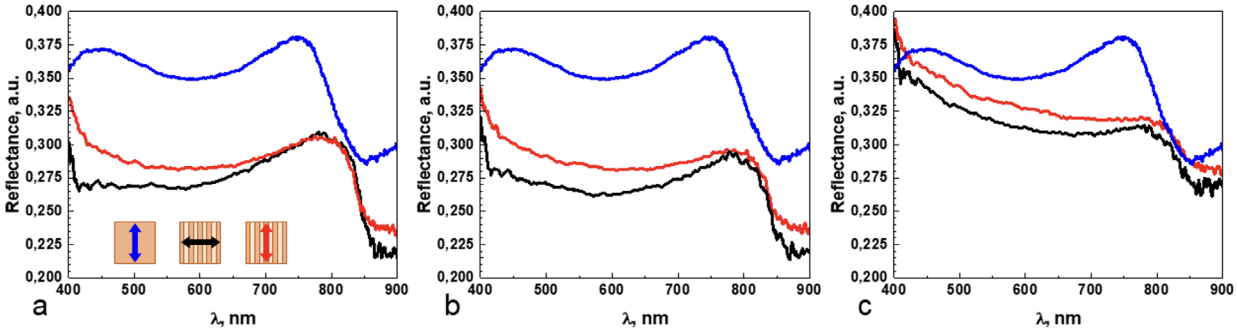

Fig. 5. Reflectance spectra of PbSe films obtained for samples treated with different pulse durations: (a) 20 ns (16.77 kW/cm^2), (b) 50 ns (13.52 kW/cm^2), (c) 100 ns (11.81 kW/cm^2), for different rotation angles of periodic structures in polarized light

The reflection maximum near 750 nm, characteristic of the unmodified PbSe film, redshifts and broadens into the 780–810 nm range after laser exposure. Varying degrees of film oxidation may alter the refractive indices and introduce optical quenching, consequently reducing the film's reflectance. The observed redshift of the maximum into the infrared region results from diffraction effects of waves reflected from the periodic structure (Chourasia et al. 2024).

Following laser modification, the film's transmittance in the visible spectrum increased to 23–25% (Fig. 6), attributed to film oxidation and thickness reduction (Olkhova et al. 2023). Notably, the pristine PbSe film exhibits no transparency in the visible spectral range. Rotation of the polarization vector relative to the LSFL lines showed negligible impact on transmitted light intensity, with only minor variations observed in the 780–810 nm region. These effects are likewise associated with film oxidation (Chourasia et al. 2024).

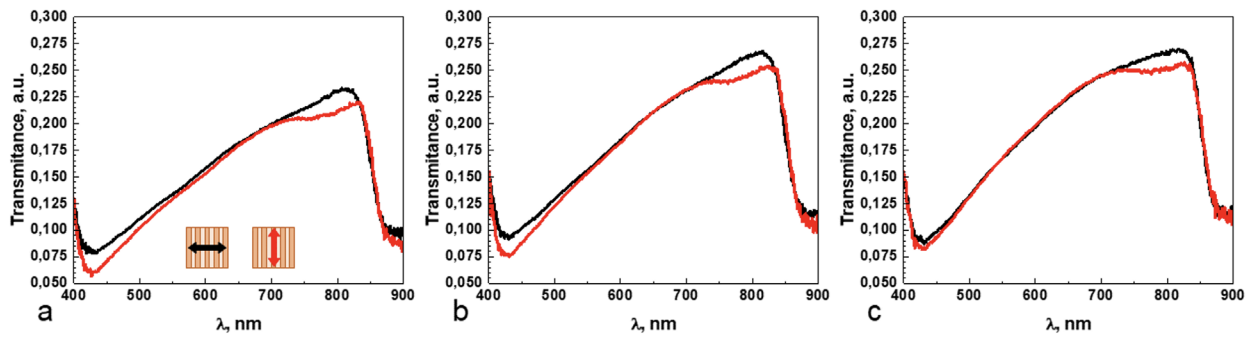

Fig. 6. Transmission spectra of PbSe films obtained for samples treated with different pulse durations: (a) 20 ns, (b) 50 ns, (c) 100 ns for different rotation angles of periodic structures in polarized light

Conclusions

The study has identified the formation modes of LIPSS on thin PbSe films under nanosecond laser irradiation. We observed a dependence of the structure periodicity on irradiation parameters. Large-period structures exhibit surface modification resulting from localized material softening and the Marangoni effect, consistent with a 'non-through oxidation' mode.

Notably, we detected a redshift of the local reflection maximum from 750 nm to 780–810 nm in samples with 0.7 μm period structures. Spectral analysis revealed that variations in transmission and reflection spectra for different polarization orientations relative to the lattice lines remain within 2%. Furthermore, treated PbSe films showed increased reflectance up to 25% in the modified regions, attributable to both film thinning and oxide layer formation.

Conflict of Interest

The authors declare that there is no conflict of interest, either existing or potential.

Author Contributions

All the authors discussed the final work and took their respective part in writing the article.

References

Antipov, A. A., Arakelian, S. M., Zimin, S. P. et al. (2012) Laser formation of semiconductor coatings using droplet technology. *Physics Procedia*, 39, 401–408. https://doi.org/10.1016/j.phpro.2012.10.054 (In English)

Bonse, J. (2020) Quo vadis LIPSS? — recent and future trends on laser-induced periodic surface structures. *Nanomaterials*, 10 (10), article 1950. https://doi.org/10.3390/nano10101950 (In English)

Chourasia, R. K., Katti, A. (2024) Optical properties of symmetrical Bragg Fiber: Periodic structures. *In: Bragg Fibers: From optical properties to applications*. Cham: Springer Nature Publ., pp. 61–84. https://doi.org/10.1007/978-3-031-65164-9_4 (In English)

Gupta, M. C., Harrison, J. T., Islam, M. T. (2021) Photoconductive PbSe thin films for infrared imaging. *Materials Advances*, 2 (10), 3133–3160. https://doi.org/10.1039/D0MA00965B (In English)

Kolchin, A. et al. (2022) Artificial anisotropy in Ge2Sb2Te5 thin films after femtosecond laser irradiation. *Materials*, 15 (10), article 3499. https://doi.org/10.3390/ma15103499 (In English)

Nielsen, R., Hemmingsen, T. H., Bonczyk, T. G. et al. (2023) Laser-annealing and solid-phase epitaxy of selenium thin-film solar cells. *ACS Applied Energy Materials*, 6 (17), 8849–8856. https://doi.org/10.1021/acsaem.3c01464 (In English)

Nykyruy, L. I., Naidych, B. P., Voznyak, O. M. et al. (2019) Account of surface contribution to thermodynamic properties of lead selenide films. *Semiconductor physics, quantum electronics & optoelectronics*, 22 (2), 156–164. https://doi.org/10.15407/spqeo22.02.156 (In English)

Olkhova, A. A., Patrikeeva, A. A., Chapalda, E. N., Sergeev, M. M. (2022) Chalcogenide films optical modification by laser influence. *Research Square.* https://doi.org/10.21203/rs.3.rs-1718096/v1 (In English)

Olkhova, A. A., Patrikeeva, A. A., Dubkova, M. A. et al. (2023) Comparison of CW NUV and Pulse NIR laser on PbSe films photosensitivity. *Applied Sciences*, 13 (4), article 2396. https://doi.org/10.3390/app13042396 (In English)

Peng, S., Li, H., Zhang, C. et al. (2022) Promoted mid-infrared photodetection of PbSe film by iodine sensitization based on chemical bath deposition. *Nanomaterials*, 12 (9), article 1391. https://doi.org/10.3390/nano12091391 (In English)

Tan, C. L., Mohseni, H. (2018) Emerging technologies for high performance infrared detectors. *Nanophotonics*, 7 (1), 169–197. https://doi.org/10.1515/nanoph-2017-0061 (In English)

Physics of Semiconductors. Semiconductors

UDC 661.691, 546.22/.24

EDN MBYUNH
https://www.doi.org/10.33910/2687-153X-2025-6-2-93-103

Thermal and laser crystallization of InSe thin films formed by vacuum thermal evaporation

M. E. Fedyanina ✉[1], V. B. Pestova [1, 2], D. V. Pepelyaev [1, 3], Ya. S. Lebedeva [1, 2], A. V. Babich [1], M. P. Smayev [1, 4], A. V. Romashkin [1], S. I. Nesterov [5], S. A. Kozyukhin [1, 3]

[1] National Research University of Electronic Technology, 1 Shokina Sq., Zelenograd 124498, Russia
[2] Herzen State Pedagogical University of Russia, 48 Moika Emb., Saint Petersburg 191186, Russia
[3] Kurnakov Institute of General and Inorganic Chemistry, 31 Leninsky Ave., Moscow 119991, Russia
[4] Lebedev Physical Institute of the Russian Academy of Sciences, 53 Leninsky Ave., Moscow 119991, Russia
[5] Ioffe Physical-Technical Institute, 26 Polytekhnicheskaya Str., Saint Petersburg 194021, Russia

Authors

Mariya E. Fedyanina, ORCID: 0000-0001-9779-2574, e-mail: mahamaha1996@gmail.com

Victoria B. Pestova, ORCID: 0000-0003-0781-0375, e-mail: kapakycek2009@yandex.ru

Dmitry V. Pepelyaev, ORCID: 0000-0002-9281-484X, e-mail: pepelyaev-dima@mail.ru

Yana S. Lebedeva, ORCID: 0000-0002-8128-1080, e-mail: generalova97@gmail.com

Alexey V. Babich, ORCID: 0000-0003-2999-8049, e-mail: drent@yandex.ru

Mikhail P. Smayev, ORCID: 0000-0003-1351-5209, e-mail: smayev@lebedev.ru

Alexey V. Romashkin, ORCID: 0000-0002-0101-6122, e-mail: romaleval@gmail.com

Sergey I. Nesterov, ORCID: 0000-0003-1166-9087, e-mail: nesterovru@mail.ru

Sergey A. Kozyukhin, ORCID: 0000-0002-7405-551X, e-mail: sergkoz@igic.ras.ru

For citation: Fedyanina, M. E., Pestova, V. B., Pepelyaev, D. V., Lebedeva, Ya. S., Babich, A. V., Smayev, M. P., Romashkin, A. V., Nesterov, S. I., Kozyukhin, S. A. (2025) Thermal and laser crystallization of InSe thin films formed by vacuum thermal evaporation. *Physics of Complex Systems*, 6 (2), 93–103. https://www.doi.org/10.33910/2687-153X-2025-6-2-93-103
EDN MBYUNH

Received 1 December 2024; reviewed 19 March 2025; accepted 19 March 2025.

Funding: Sample fabrication and experimental work were supported by the Russian Science Foundation (project No. 22-19-00766) with contributions from the Research Laboratory of Active Photonic Materials and Devices. Raman spectroscopy and AFM measurements were supported by the Ministry of Science and Higher Education of the Russian Federation in the framework of state task (FSMR-2023-0002).

Abstract. Binary chalcogenides have found a wide range of applications due to the possibility of fast and reversible phase transitions, tunable band gap, and high charge carrier mobility. This paper presents the results of thermal and laser crystallization of InSe thin films deposited by vacuum thermal evaporation of synthesized material and covered with a protective SiO_2 layer. The amorphous state of as-deposited InSe thin films was confirmed by Raman spectroscopy. Thermal and laser crystallization processes were studied using electrical resistivity measurements and optical microscopy respectively. The temperature and laser power ranges required for the crystallization of the InSe thin film were determined. The Raman spectroscopy showed that the degree of crystallinity of modified regions of InSe thin films can be tuned by varying the power of laser irradiation.

Keywords: chalcogenide materials, binary compounds, InSe, optical properties, structural properties, laser crystallization

Introduction

In recent decades, thin chalcogenide films have attracted considerable attention due to their unique electrical and optical properties, which make it possible to implement various devices for storing and processing data, and for the modulation and conversion of optical radiation. Of special interest is the control of the properties of materials through changing the phase state or van der Waals gap reconfiguration — for example, through the application of uniaxial compression (Stepanov 2024). Numerous applications of chalcogenide materials and greater attention to two-dimensional chalcogenide structures have fostered the study of $A^{III}B^{VI}$ system. It includes InSe, which is an n-type layered semiconductor with a band gap of 1.2–1.3 eV (Darwish et al. 2013; Kovalyuk et al. 2005). InSe structures with a small number of layers allow an adjustment of the optical band gap in the range of 1.4–2.6 eV and are characterized by an extremely high mobility of charge carriers (Bandurin et al. 2017).

Currently, the possibility of creating InSe-based photosensitive elements is widely discussed (Song et al. 2020). The formation of photodetectors with different architectures, including photodetectors with simultaneous use of 1D and 2D objects (Dai et al. 2018), has been described in previous studies (Feng et al. 2015; Wang et al. 2020). Besides, the use of InSe in flexible electronics (Zhao et al. 2019), optical fibers and for the implementation of photoinduced structural transformations (Xin et al. 2024) opens up significant prospects.

Featuring prominently among the main methods for obtaining InSe film samples are the electrodeposition technique (Gopal et al. 2004), molecular beam epitaxy (Emery et al. 1989; Voigt et al. 2024b), chemical vapor deposition (Chang et al. 2018; Park et al. 2003), and thermal evaporation (El-Nahass et al. 2012; Kobbi, Kesri 2004). Depending on the method, growth conditions, and parameters, InSe films can be also obtained as either amorphous or crystalline. In (Mustafa et al. 2010) In_xSe_{1-x} thin films were prepared using the thermal evaporation technique, while the XRD analysis confirmed the amorphous structure of the deposited films. This film formation method enables the study of the crystallization process, which, in phase-change materials, is a lower-temperature and longer process compared to amorphization.

Unlike other chalcogenide materials, such as materials of the Ge–Sb–Te system (Prikryl et al. 2022; Rybin et al. 2021; Smayev et al. 2024), Sb_2Se_3 (Lebedeva et al. 2023), or MoS_2 (Rani et al. 2017; Tran-Khac et al. 2019), phase transformation study by laser modification in InSe film samples has not produced many results so far. Laser irradiation with millisecond pulses of amorphous In_2Se_3 films prepared by thermal evaporation crystallizes thin film samples into a monoclinic phase (Khusayfan et al. 2024). At the same time, change in optical and electrical properties is attractive for optoelectronic devices and terahertz technology. The development of technology for creating a single-crystal InSe optical fiber was described in (Xin et al. 2024), where a polycrystalline fiber core was formed by stretching the molten InSe powder and re-crystallization of InSe induced by a CO_2 laser was used to obtain the desired fiber characteristics.

This work studies the formation of InSe amorphous thin-film samples by vacuum thermal evaporation and their optical, electrical, Raman spectra characteristics, and thermal and laser crystallization features.

Methods and materials

A quartz ampoule containing semiconductor grade (5N) starting components, taken in stoichiometric proportions, was vacuum-sealed to a residual pressure of $P = 10^{-2}$ Pa. Synthesis was performed by melting elements directly in a vacuumized quartz ampoule in a resistive heating furnace equipped with a rotation system for melt homogenization. The mixture was heated from room temperature to 660 °C at a heating rate of 1.5 °C/min. The melt was maintained for two hours at a temperature of 250 °C, which is above the melting point of selenium.

X-ray diffraction (XRD) patterns of the synthesized samples were studied using a D8 ADVANCE (Bruker) diffractometer to investigate the structure of the bulk InSe compound. Elemental analysis of the sample was performed using X-ray fluorescence (XRF) spectroscopy (M1 Mistral spectrometer).

Thermal analysis of the synthesized material was conducted using a TA Instruments Q600 SDT device, which enables simultaneous measurements of differential scanning calorimetry (DSC) and thermogravimetry (TGA). The analyses were performed in an argon atmosphere with heating and cooling rates of 10 °C/min and the maximum heating temperature of 700 °C.

 https://www.doi.org/10.33910/2687-153X-2025-6-2-93-103

The diffuse reflectance of the bulk InSe compound was determined using Cary 5000 (Agilent) spectrophotometer equipped with an integrating sphere of 150 mm in diameter with a wavelength step of 1 nm.

The formation of amorphous films of the studied chalcogenide semiconductor was ensured by the vacuum thermal evaporation method using the UVN-2M setup. The film deposition process employed a molybdenum boat as a resistive evaporator. The pressure in the chamber was 4×10^{-3} Pa, with the distance of 15.5 cm between the substrate and the evaporator and the sample weight of ~ 5 mg. The samples were coated with a 20 nm thick SiO_2 layer using the electron beam method to minimize material degradation and oxidation during subsequent heat treatment. Corning glass 1737F was used as sample substrates for laser irradiation and recording of Raman spectra, silicon substrates for determining thickness, phase and elemental composition, and oxidized silicon substrates for studying the temperature dependence of specific resistivity.

The elemental composition of the thin films was analyzed using a Tescan Amber scanning electron microscope equipped with an energy-dispersive X-ray (EDX) spectrometer. The thickness of the InSe thin films was determined using atomic force microscopy (AFM, scanning probe microscope Solver PRO", NT-MDT) in the semi-contact mode. The thickness of the SiO_2 layer was estimated using an Ellips-1881A ellipsometer. The temperature dependence of the resistivity of the thin films was measured in the range from room temperature to 300 °C. Measurements were carried out in an argon atmosphere with heating/cooling rates of 5 °C/min.

The structure of the synthesized bulk material and thin films before and after thermal or laser treatment was identified using Raman spectroscopy. The Raman spectra were measured at room temperature using a Centaur U HR spectrometer (λ = 532 nm, edge filter from 50 cm^{-1}, monochromator with a dispersion of 1.3 nm/mm and spectral resolution of at least 1 cm^{-1}). The spectrum accumulation time was 1 min, and the laser radiation power, 0.4 mW.

The irradiation of amorphous InSe films was carried out using a continuous wave Nd^{3+}:YAG laser with a wavelength of 532 nm. The laser radiation (TEM_{00} mode) was focused using a lens with a focal length of 100 mm, resulting in a spot with a diameter of about 50 μm on the film surface. The exposure time was 100 ms. The laser exposure was studied at light beam powers in the range from 10 to 330 mW. Since the crystalline phase of InSe is characterized by a higher reflection coefficient in the visible range than the amorphous one (El-Nahass et al. 2012), the results of the laser radiation on thin films were analyzed using an optical microscope (Altami MET 3T).

Results and discussions

InSe bulk samples

The X-ray fluorescence analysis of the elemental composition of the bulk InSe sample revealed a spectrum containing only the analytical peaks corresponding to selenium (Se) and indium (In). No impurities were detected above the detection limit of the device. An assessment of the elemental composition led to concentration values of $C_{wt.\%In}$ = 59.2 ± 0.8% and $C_{wt.\%Se}$ = 40.8 ± 1.1%, which are close to the expected ones.

The phase analysis of the InSe compound was performed using XRD and was followed by the Rietveld method applied in the TOPAS 4.2 software package. We established that the material crystallizes into a hexagonal structure. The refined unit cell parameters are a = 4.005 Å, b = 4.005 Å, and c = 16.400 Å. These parameters are consistent with literature data (Alieva et al. 2020).

The DSC and TGA measurements are presented in Fig. 1. The DSC curves exhibit two distinct endothermic peaks, one at 602 °C and the other at 620 °C. The melting temperature of the material, established as 602 °C, agrees with literature data (Bergeron et al. 2020). According to (Tedenac et al. 1997; Vassilev et al. 1998), the higher-temperature endothermic peak at 620 °C corresponds to the liquidus temperature of the InSe compound. After this peak, a sharp decrease in mass is observed in the TGA data, which is attributed to the evaporation of the material.

Fig. 2 shows the Raman spectrum obtained for the bulk material. Due to the crystalline nature of the material, the spectrum was decomposed into a set of peaks using the Lorentz function (Strubbe et al. 2015; Yuan, Mayanovic 2017). The positions of the peak maxima for the polycrystalline material are recorded near 111, 173, and 224 cm^{-1}, which corresponds to the vibrations of the A^1_{1g}, E^1_{2g}, and A^2_{1g} modes of InSe structural units (Wu et al. 2019; Xie et al. 2021). The signal in the region of 120–145 cm^{-1} can be attributed to a small number of chains of Se atoms between InSe clusters, which can be more significant in the amorphous state, while the signal around 245 cm^{-1} may be associated with two-phonon scattering (Weszka et al. 2000).

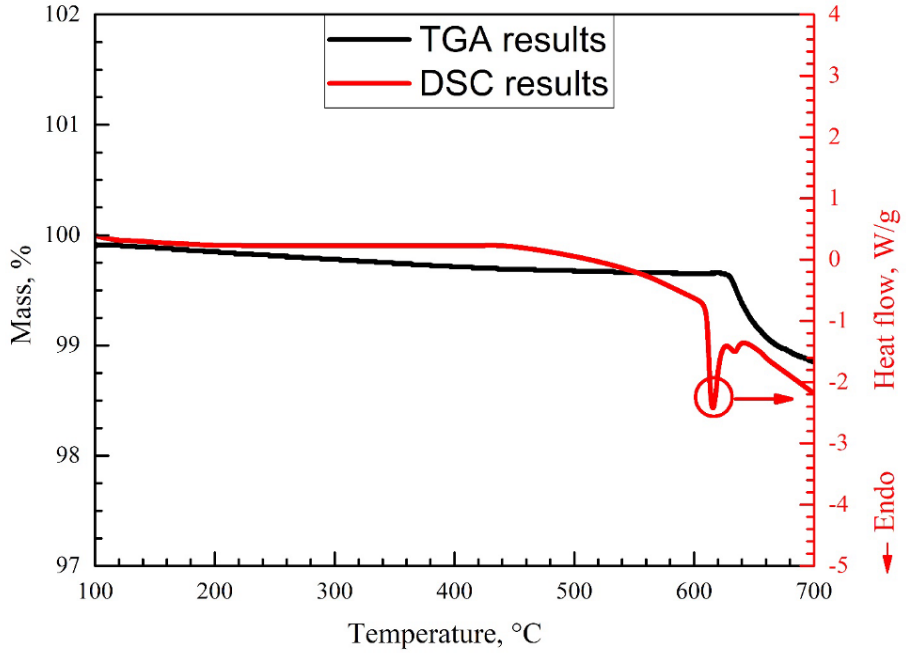

Fig. 1. DSC and TGA measurements of synthesized polycrystalline InSe

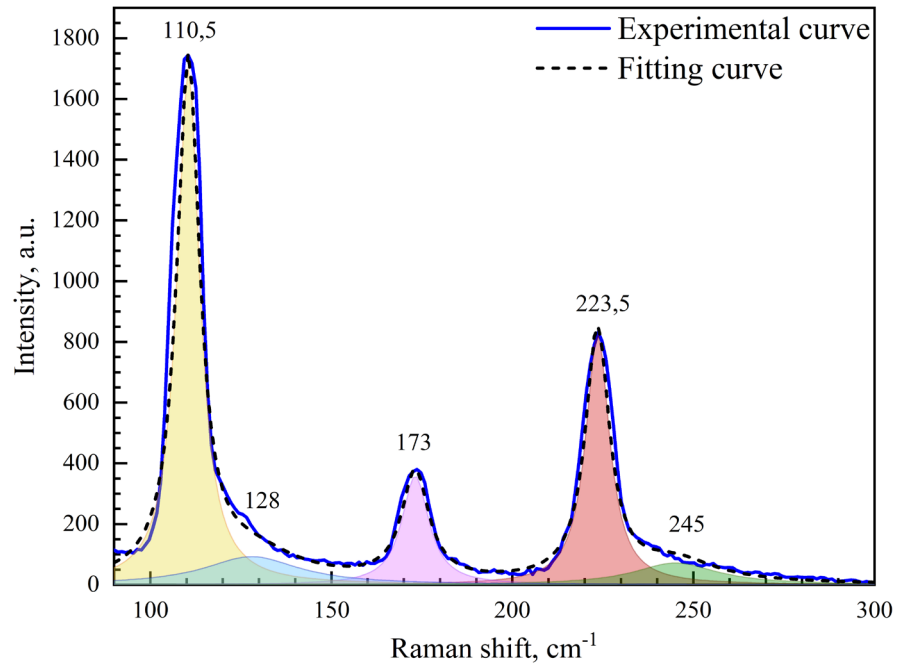

Fig. 2. Raman spectrum of bulk InSe

The results of the diffuse reflectance spectra measurements for the milled synthesized InSe are presented in Fig. 3. These data were processed using the Kubelka–Munk equation, which enabled the determination of the optical absorption edge (Kortüm et al. 1963)

$$F\left(R_d\right)=\frac{\left(1-R_d\right)^2}{2\cdot R_d}, \quad (1)$$

where R_d is diffuse reflection and $F(R_d)$ is a parameter proportional to the absorption coefficient.

 https://www.doi.org/10.33910/2687-153X-2025-6-2-93-103

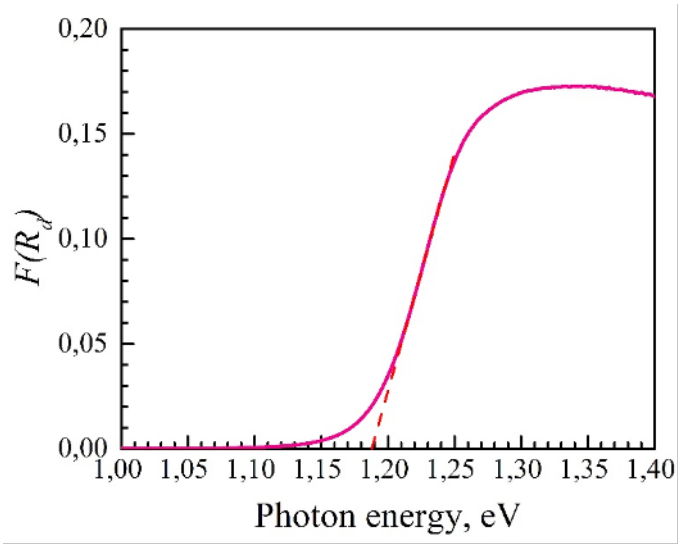

Fig. 3. Spectral dependence of the diffuse reflection of bulk InSe and estimation of the optical band gap (inset)

The optical band gap of the synthesized InSe material was determined from the intersection point of the tangent with the abscissa axis in the $F(R_d)$ energy dependence (Tarasov et al. 2023) as illustrated in Fig. 3 (inset). The obtained value of the optical band gap is 1.2 eV, which is in agreement with literature data (Olguín et al. 2003).

InSe thin-film samples

EDX microanalysis of the InSe thin films revealed spectrograms presented in Fig. 4, which clearly exhibit pronounced reflections corresponding to indium and selenium. Additionally, the spectra show peaks associated with a low carbon content. The study of areas of 200×200 mkm^2, shown in the upper images in Fig. 4, confirm the uniformity of In and Se distribution over the surface of the studied sample.

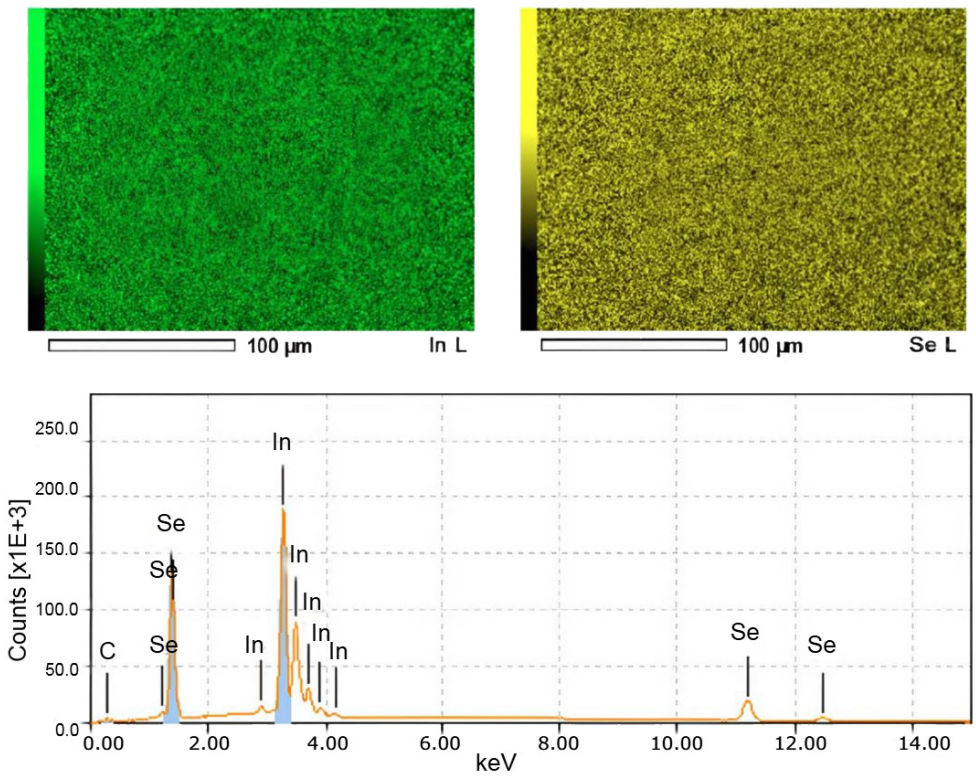

Fig. 4. EDX results of InSe thin film deposited by vacuum thermal evaporation. The upper images show the distribution of In and Se elements over the film surface, while the lower graph shows the elemental composition of the studied area

According to the atomic force microscopy measurements, the thickness of the deposited films was 16 nm with a surface roughness not above 1 nm. Ellipsometry made it possible to obtain the thickness of the protective SiO_2 layer, which was approximately 20 nm.

The temperature dependence of the resistivity of the InSe thin film is presented in Fig. 5. The sample was heated from room temperature to 300 °C. A notable feature in this dependence is a sharp decrease of resistivity from 5×10^3 to 1×10^{-1} Ohm×cm, observed in the temperature range from 210 to 235 °C. This significant drop is attributed to the crystallization of the thin film.

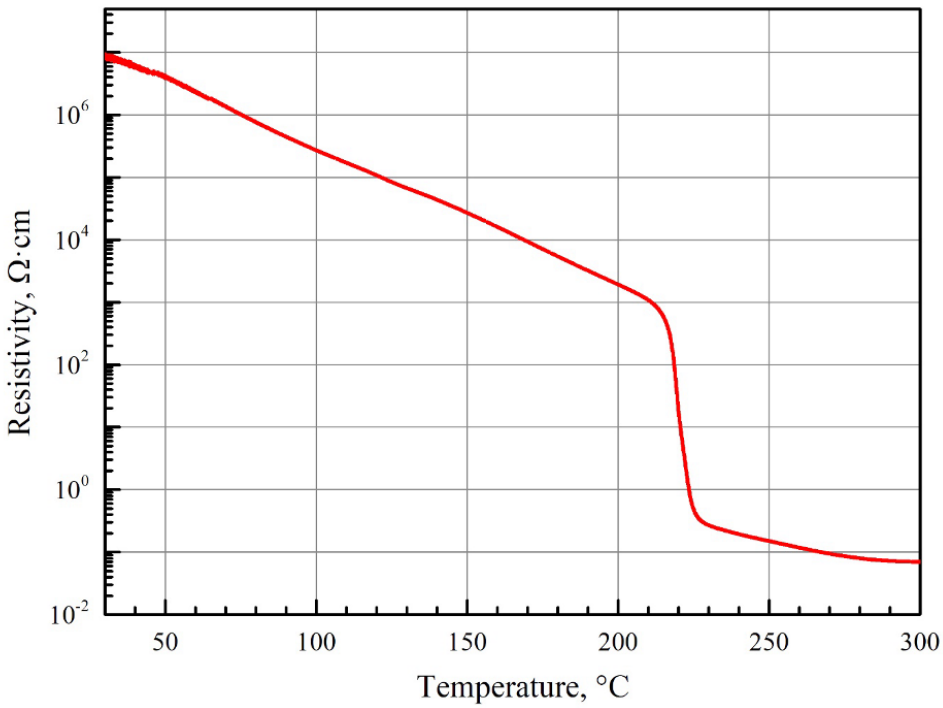

Fig. 5. Temperature dependence of the resistivity of the InSe thin film

To identify the expected structural changes, Raman spectra were measured for the as-deposited InSe film and the film annealed in an argon atmosphere for 20 minutes at 250 °C. The results are shown in Fig. 6.

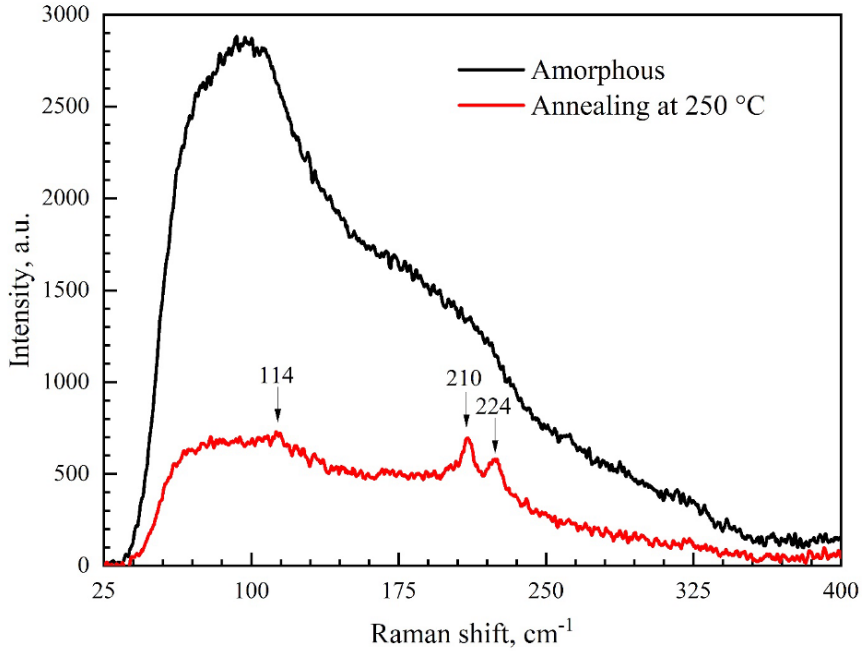

Fig. 6. Raman spectra for the as-deposited amorphous film and the film annealed at 250 °C

https://www.doi.org/10.33910/2687-153X-2025-6-2-93-103

The Raman spectroscopy showed that the shape of the spectra of the InSe films thermally treated at 250 °C and coated with a protective SiO_2 layer differs significantly from the spectra obtained from the initial amorphous films. As a result of the thermal treatment, peaks near 114, 210, and 224 cm^{-1} appear in the spectrum; the last two peaks are quite narrow. Comparison of the positions of these peaks with the peaks in the spectrum obtained from the polycrystalline bulk material (Fig. 2) showed that these peaks correspond to the A^1_{1g} and A^2_{1g} (114 and 224 cm^{-1}) vibrational modes of InSe structural units, characteristic of the crystalline state (Wu et al. 2019; Xie et al. 2021). Additionally, a narrow peak at about 210 cm^{-1}, which appears relative to the spectrum of the polycrystalline bulk material, can be attributed to E'(LO) vibrations, which appear along with the A^1_{1g} and A^2_{1g} peaks for polycrystalline InSe in the form of hexagonal sheets (Choi et al. 2003). A similar peak was observed for hexagonal InSe film synthesized on a graphite (HOPG) substrate (Voigt et al. 2024a).

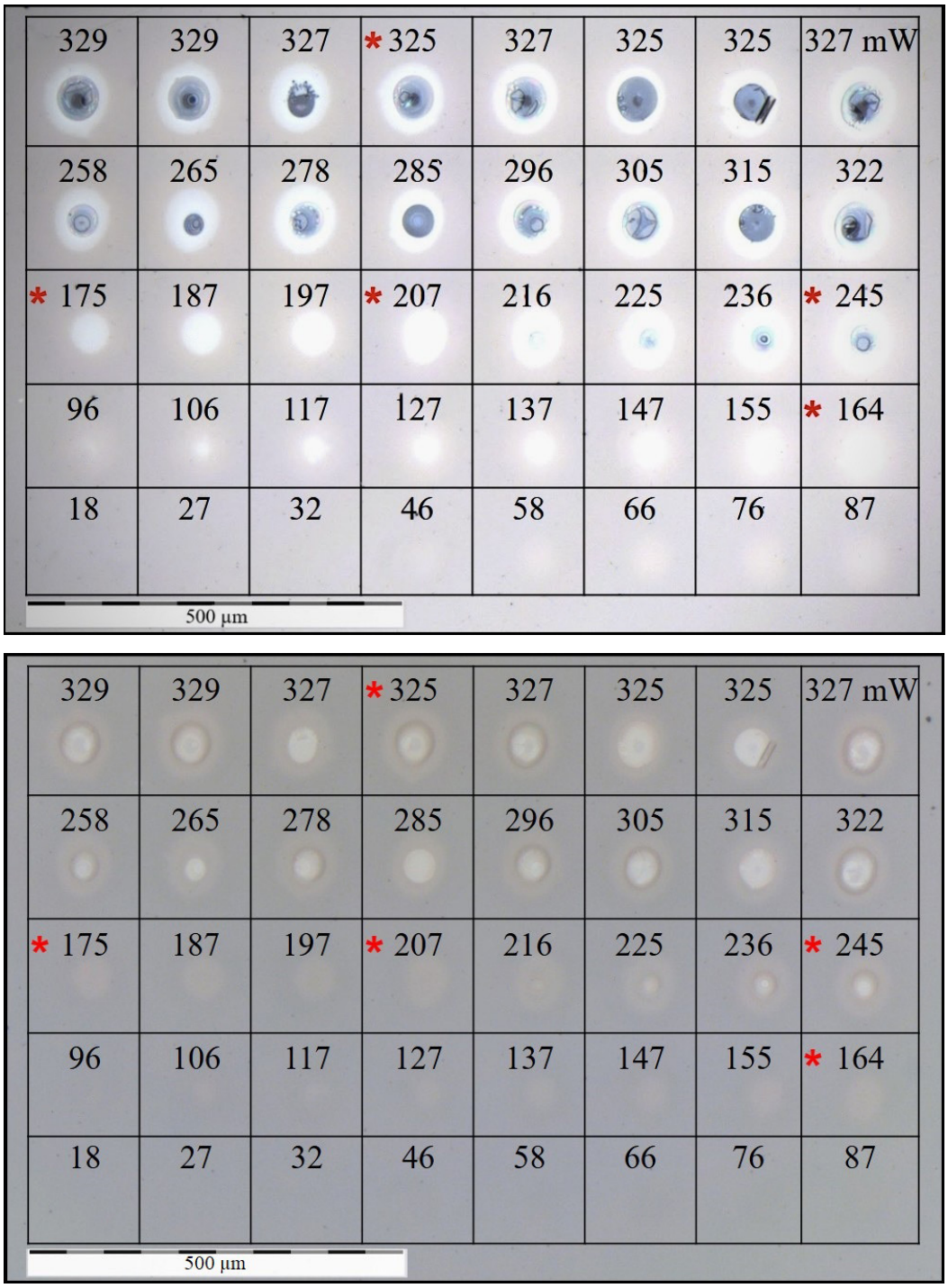

Fig. 7. Optical microscope images of a laser-irradiated InSe thin film in reflected (a) and transmitted (b) backlight modes (the regions where Raman spectra were measured are marked with the * symbol)

The optical microscopy images of the InSe films illuminated by a cw-laser were obtained in reflected (Fig. 7a) and transmitted (Fig. 7b) backlight regimes. It is evident from the figures that all illuminated areas can be divided into three groups. The first group consists of areas resulting from irradiation with laser powers ranging from 18 to 96 mW. The reflectivity of the film remains unchanged or undergoes only minor changes. An analysis of the Raman spectra reveals that in this case laser exposure does not induce any phase transformation of InSe. Corresponding Raman spectra are identical to those obtained from the original as-deposited (non-irradiated) film, as illustrated by the black and green curves in Fig. 8.

The second group comprises areas formed as a result of laser exposure with powers from 96 to 207 mW. The reflectivity of these areas is significantly higher than that of the as-deposited amorphous film. The Raman spectra exhibit peaks with maxima near 112, 210, and 225 cm^{-1}, which are characteristic of a crystalline phase of InSe. As the radiation energy goes up from 164 to 207 mW, the intensity of these peaks also increases, indicating a rise in the degree of crystallinity of the modified InSe areas. This suggests that higher laser powers enhance the crystallization process.

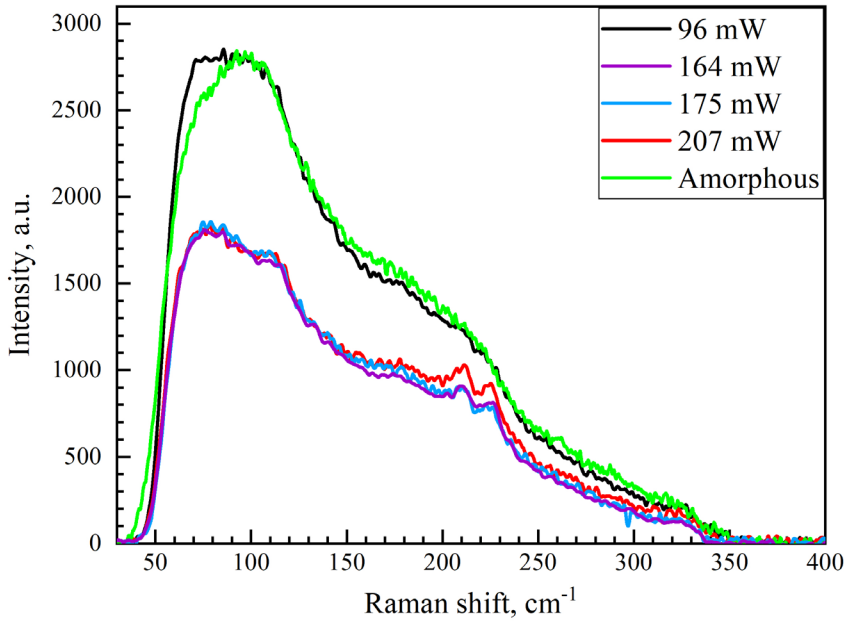

Fig. 8. Raman spectra of the InSe thin film coated with SiO_2 in areas after laser exposure with a different power

The third group comprises areas resulting from irradiation with a laser power exceeding 207 mW. As follows from Fig. 7, the central part of the irradiated area, where the laser radiation energy is maximal due to Gaussian intensity distribution, shows material ablation or degradation. That is clearly confirmed by the fact that the irradiated areas of the film (at powers above 216 mW) become bright in the optical microscope transmission mode (Fig. 7b), i. e. the transparency of the samples increases with the destruction of InSe, tending to the transmission of the glass substrate. The higher the radiation energy, the larger the ablation or degradation area. At the periphery of the irradiation area, corresponding to the tails of the Gaussian radiation intensity distribution, regions with increased reflectivity are observed. These regions are similar to those in group 2 but display a lower intensity in both the specific peaks and the overall Raman spectrum compared to areas modified by laser powers between 117 and 207 mW. This reduction in intensity is attributed to the partial evaporation of the material due to the small thickness of the InSe film and the SiO_2 protective film. This is also confirmed by the fact that the ablation threshold of SiO_2 is obviously not exceeded by the laser action used in present work (Mangersnes et al. 2010; Rublack et al. 2011).

Conclusions

Studies of InSe bulk samples showed that the synthesized material is close to the declared stoichiometric composition, with the melting point of 602 °C and the optical band gap of 1.2 eV. The use of vacuum thermal evaporation enabled the production of thin amorphous films, opening up opportunities

 https://www.doi.org/10.33910/2687-153X-2025-6-2-93-103

for studying phase transformations in InSe upon heating or as a result of laser irradiation. Thin-film InSe samples were passivated with a SiO_2 film for protection against oxidation and mechanical damage.

The temperature dependence of film resistivity showed that phase transition from the amorphous to the crystalline state is in the range from 210 to 235 °C. Raman studies performed for the film annealed at 250 °C confirmed its crystallization by the presence of characteristic peaks. Laser irradiation of thin films was carried out in the power range from 10 to 330 mW. At low optical powers (up to 96 mW), film crystallization is practically not observed, either with an optical microscope or by Raman spectroscopy. At powers from 96 to 207 mW, film crystallization occurs partially, and with an increasing power, the intensity of the Raman scattering peaks corresponding to the crystalline phase rises. Above 207 mW, film ablation begins, and InSe destruction is observed within the irradiated areas. Thus, threshold values of temperatures and laser powers necessary for the crystallization of amorphous InSe thin films formed by vacuum thermal evaporation were determined.

Conflict of Interest

The authors declare that there is no conflict of interest, either existing or potential.

Author Contributions

Optical and electrophysical measurements, writing — original draft preparation: M. E. Fedyanina; AFM and Raman measurements: V. B. Pestova, A. V. Romashkin; synthesis and deposition of films: D. V. Pepelyaev; laser irradiation of thin films: Ya. S. Lebedeva, M. P. Smayev; DSC measurements: A. V. Babich, supervision: S. A. Kozyukhin, S. I. Nesterov.

References

Alieva, I. I., Mamedova, N. A., Sadygov, F. M. et al. (2020) Investigation of chemical interactions in the Sb_2Te_3-InSe system and properties of the obtained phases. *Russian Journal of Inorganic Chemistry*, 65 (10), 1585–1590. http://dx.doi.org/10.1134/S0036023620100010 (In English)

Bandurin, D. A., Tyurnina, A. V., Yu, G. L. et al. (2017) High electron mobility, quantum Hall effect and anomalous optical response in atomically thin InSe. *Nature Nanotech*, 12, 223–227. https://doi.org/10.1038/nnano.2016.242 (In English)

Bergeron, H., Guiney, L. M., Beck, M. E. et al. (2020) Large-area optoelectronic-grade InSe thin films via controlled phase evolution. *Applied Physics Reviews*, 7, article 041402. https://doi.org/10.1063/5.0023080 (In English)

Chang, H-C., Tu, C-L., Lin, K. et al. (2018) Synthesis of Large-Area InSe Monolayers by Chemical Vapor Deposition. *Small*, 14 (39), article 1802351. https://doi.org/10.1002/smll.201802351 (In English)

Choi, I. H., Yu, P. Y. (2003) Properties of phase-pure InSe films prepared by metalorganic chemical vapor deposition with a single-source precursor. *Journal of Applied Physics*, 93 (8), 4673–4677. https://doi.org/10.1063/1.1561584 (In English)

Dai, M., Chen, H., Feng, R. et al. (2018) A dual-band multilayer InSe self-powered photodetector with high performance induced by surface Plasmon resonance and asymmetric Schottky junction. *ACS Nano*, 12 (8), 8739–8747. https://doi.org/10.1021/acsnano.8b04931 (In English)

Darwish, A. A. A., El-Nahass, M. M., Bahlol, M. H. (2013) Structural and electrical studies on nanostructured InSe thin films. *Applied Surface Science*, 276, 210–216. https://doi.org/10.1016/j.apsusc.2013.03.068 (In English)

El-Nahass, M. M., Saleh, A-B. A., Darwish, A. A. A. Bahlol, M. H. (2012) Optical properties of nanostructured InSe thin films. *Optics Communications*, 285 (6), 1221–1224. https://doi.org/10.1016/j.optcom.2011.11.031 (In English)

Emery, J. Y., Brahim-Otsmane, L., Jouanne, M. et al. (1989) Growth conditions of In_xSe_y films by molecular beam deposition. *Materials Science and Engineering: B*, 3 (1-2), 13–17. https://doi.org/10.1016/0921-5107(89)90172-4 (In English)

Feng, W., Wu, J., Li, X. et al. (2015) Ultrahigh photo-responsivity and detectivity in multilayer InSe nanosheets phototransistors with broadband response. *Journal of Materials Chemistry C*, 3, 7022–7028. https://doi.org/10.1039/C5TC01208B (In English)

Gopal, S., Viswanathan, C., Thamilselvan, M. et al. (2004) Conduction studies on electrodeposited indium selenide thin films. *Ionics*, 10, 300–303. https://doi.org/10.1007/BF02382835 (In English)

Khusayfan, N. M., Qasrawi, A. F., Khanfar, H. K., Alharbi, S. R. (2024) Fast crystallization of InSe thin films via pulsed laser welding technique and effect of crystallinity on the optical and dielectric properties. *Physica Scripta*, 99 (2), article 025988. https://doi.org/10.1088/1402-4896/ad2040 (In English)

Kobbi, B., Kesri, N. (2004) Physico-chemical and electrical properties of InSe films. *Vacuum*, 75 (2), 177–182. https://doi.org/10.1016/j.vacuum.2004.02.003 (In English)

Kortüm, G., Braun, W. Herzog, G. (1963) Principles and techniques of diffuse-reflectance spectroscopy. *Angewandte Chemie*, 2 (7), 333–341. https://doi.org/10.1002/anie.196303331 (In English)

Kovalyuk, Z. D., Katerynchuk, V. M., Mintyanskii, I. V. et al. (2005). γ-Radiation influence on the photoelectrical properties of oxide–p-InSe heterostructure. *Materials Science and Engineering: B*, 118 (1-3), 147–149. https://doi.org/10.1016/j.mseb.2004.12.024

Lebedeva, Y. S., Smayev, M. P., Budagovsky, I. A. et al. (2023) Photoinduced Crystallization of Sb_2Se_3 and $Ge_2Sb_2Te_5$ Chalcogenide Films. *Journal of Surface Investigation*, 17, 339–348. https://doi.org/10.1134/S1027451023070297 (In English)

Mangersnes, K., Foss, S. E., Thogersen, A. (2010) Damage free laser ablation of SiO_2 for local contact opening on silicon solar cells using an a-Si:H buffer layer. *Journal of Applied Physics,* 107 (4), article 043518. http://dx.doi.org/10.1063/1.3309382 (In English)

Mustafa, F. I., Gupta, S., Goyal, N., Tripathi, S. K. (2010) Effect of indium concentration on the electrical properties of InSe alloy. *Physica B: Condensed Matter*, 405 (19), 4087–4091. https://doi.org/10.1016/j.physb.2010.06.006 (In English)

Olguín, D., Cantarero, A., Ulrich, C., Syassen, K. (2003) Effect of pressure on structural properties and energy band gaps of γ-InSe. *Physica Status Solidi (b)*, 235 (2), 456–463. https://doi.org/10.1002/pssb.200301602 (In English)

Park, J-H., Afzaal, M., Helliwell, M. et al. (2003) Chemical vapor deposition of indium selenide and gallium selenide thin films from mixed Alkyl/Dialkylselenophosphorylamides. *Chemistry of Materials*, 15 (22), 4205–4210. https://doi.org/10.1021/cm0310420 (In English)

Prikryl, J., Mistrik, J., Krbal, M. (2022) Optical properties of as-deposited, annealed and laser-treated $Ge_2Sb_2Te_5$ thin films. *Optical Materials Express*, 12, 2927–2937. https://doi.org/10.1364/OME.462278 (In English)

Rani, R., Dimple, D., Jena, N. et al. (2017) Controlled formation of nanostructures on MoS_2 layers by focused laser irradiation. *Applied Physics Letters*, 110, article 083101. https://doi.org/10.1063/1.4976692 (In English)

Rublack, T., Hartnauer, S., Kappe, P. et al. (2011) Selective ablation of thin SiO_2 layers on silicon substrates by femto- and picosecond laser pulses. *Applied Physics A*, 103, 43–50. http://dx.doi.org/10.1007/s00339-011-6352-x (In English)

Rybin, M. V., Sinelnik, A. D., Tajik, M. et al. (2021) Optically reconfigurable spherical Ge-Sb-Te nanoparticles with reversible switching. *Laser & Photonics Reviews*, 16 (2), article 2100253. https://doi.org/10.1002/lpor.202100253 (In English)

Smayev, M. P., Smirnov, P. A., Budagovsky, I. A. et al. (2024) Cylindrical laser beams for a-$Ge_2Sb_2Te_5$ thin film modification. *Journal of Non-Crystalline Solids*, 633, article 122952. https://doi.org/10.1016/j.jnoncrysol.2024.122952 (In English)

Song, Ch., Huang, Sh., Wang, Ch. et al. (2020) The optical properties of few-layer InSe. *Journal of Applied Physics*, 128, article 060901. https://doi.org/10.1063/5.0018480 (In English)

Stepanov, R. S. (2024) Uniaxial pressure modulation of two-dimensional materials: Insights into the structure and electronic properties of $MoTe_2$ and Sb_2Te_3. *Physics of Complex Systems*, 5, 30–38. https://doi.org/10.33910/2687-153X-2024-5-1-30-38 (In English)

Strubbe, D. A., Johlin, E. C., Kirkpatrick, T. R. et al. (2015) Stress effects on the Raman spectrum of an amorphous material: Theory and experiment on a -Si:H. *Physical Review B*, 92, article 241202. https://doi.org/10.1103/PhysRevB.92.241202 (In English)

Tarasov, A., Dubkov, S., Vigdrovich, E. et al. (2023) Photocatalytic reduction of CO_2 over TiO_2 nanowires catalyst. *MATEC Web of Confere*nces, 376, article 01011. https://doi.org/10.1051/matecconf/202337601011 (In English)

Tedenac, P. J.-C., Vassilev, D. G. P., Daouchi, B. et al. (1997) Low-temperature Region of the In–Se System. *Crystal Research and Technology*, 32 (4), 605–616. https://doi.org/10.1002/crat.2170320417 (In English)

Tran-Khac, B-C., White, R., DelRio, F. Chung, K-H. (2019) Layer-by-layer thinning of MoS_2 via laser irradiation. *Nanotechnology*, 30, article 275302. http://dx.doi.org/10.1088/1361-6528/ab11ad (In English)

Vassilev, G. P., Daouchi, B., Record, M., Tedenac, J. (1998) Thermodynamic studies of the In–Se system. *Journal of Alloys and Compounds*, 269, 107–115. https://doi.org/10.1016/S0925-8388(98)00007-3 (In English)

Voigt, C. A., Reingold, M., Dube, A. et al. (2024a) Molecular beam epitaxy synthesis of In_2Se_3 films. *Journal of Vacuum Science & Technology A*, 42 (3), article 032707. https://doi.org/10.1116/6.0003508 (In English)

Voigt, C. A., Tian, M., Peacock, R. et al. (2024b) Quantitative Raman and x-ray photoelectron spectroscopy of mixed-phase indium selenide films. *Journal of Applied Physics*, 135 (21), article 215301. http://dx.doi.org/10.1063/5.0202596 (In English)

Wang, Y., Gao, J., Wei, B. et al. (2020) Reduction of the ambient effect in multilayer InSe transistors and a strategy toward stable 2D-based optoelectronic application. *Nanoscale*, 12, 18356–18362. https://doi.org/10.1039/D0NR04120C (In English)

Weszka, J., Daniel, P., Burian, A. M. (2000) Raman Spectra of $In_{0.30}Se_{0.70}$ Amorphous Films. *Acta Physica Polonica A*, 98 (5), 619–623. (In English)

Wu, M., Xie, Q., Wu, Y. et al. (2019) Crystal structure and optical performance in bulk γ-InSe single crystals. *AIP Advances*, 9 (2), article 025013. https://doi.org/10.1063/1.5086492 (In English)

Xie, Q., Hu, C., Xu, L. et al. (2021) Stability studies of few-layer InSe nanosheets by Raman spectroscopy. *Solid State Communications*, 336, article 114417. https://doi.org/10.1016/j.ssc.2021.114417 (In English)

Xin, L., He, H., Wang, X. et al. (2024) Single-crystalline indium selenide fibers by laser-induced recrystallization and their tunable whispering-gallery-mode lasing by pressure-modulating. *Journal of the American Ceramic Society*, 107 (9), 5801–5809. https://doi.org/10.1111/jace.19916 (In English)

Yuan, X., Mayanovic, R. A. (2017) An empirical study on Raman peak fitting and its application to Raman quantitative research. *Applied Spectroscopy*, 71 (10), 2325–2338. http://dx.doi.org/10.1177/0003702817721527 (In English)

Zhao, O., Frisenda, R., Wang, T., Castellanos-Gomez, A. (2019) InSe: A two-dimensional semiconductor with superior flexibility. *Nanoscale*, 11, 9845–9850. https://doi.org/10.1039/C9NR02172H (In English)

Physics of Semiconductors.
Computational materials science

UDC 538.9

EDN WANXEA
https://www.doi.org/10.33910/2687-153X-2025-6-2-104-109

The effect of uniaxial compression on micro- and macro-parameters of CdSe quantum dots of different sizes

Yu. A. Melchakova [1,2] ✉, A. I. Solomonov [1]

[1] National Research University ITMO, 49 Kronverksky Ave., Saint Petersburg 197101, Russia
[2] Tomsk State University, 36 Lenin Ave., Tomsk 634050, Russia

Authors

Yulia A. Melchakova, ORCID: 0000-0003-4694-2995, e-mail: iuliia.melchakova@metalab.ifmo.ru

Alexander I. Solomonov, ORCID: 0000-0003-1348-5951

For citation: Melchakova, Yu. A., Solomonov, A. I. (2025) The effect of uniaxial compression on micro- and macro-parameters of CdSe quantum dots of different sizes. *Physics of Complex Systems*, 6 (2), 104–109. https://www.doi.org/10.33910/2687-153X-2025-6-2-104-109 EDN WANXEA

Received 21 February 2025; reviewed 1 April 2025; accepted 1 April 2025.

Funding: This work was supported by the Ministry of Education and Science of the Russian Federation under the state assignment (No. FSWM-2025-0007).

Abstract. In this paper, we analyze and discuss DFT calculations for zinc blende and wurtzite CdSe quantum dots (QDs). We found QDs with a size of 1.6 Å to be stable and relaxed using the PBE exchange-correlation functional. The behavior of frontier orbitals (HOMO, LUMO) was examined for an unrelaxed structure to include symmetry and degeneracy. The results of the Purcell factor of the zinc blende and wurtzite QDs with a size of 1.6 Å were found to be stable under axial compression. The designed quantum dots demonstrate mechanical and optical stability, their properties retained under uniaxial compression.

Keywords: DFT, FDTD, quantum dots, cadmium selenide, wurtzite, zinc blende, electronic properties, Purcell factor

Introduction

CdSe quantum dots are semiconductor nanocrystals that exhibit unique optical and electronic properties due to their small size and quantum confinement effects (Alnemrat et al. 2014; Huang et al. 2024; Kolobkova et al. 2024; Zhang et al. 2024a; 2024b). These quantum dots possess a wide range of properties, including size-dependent optical ones such as a size-dependent band gap (Alsalme et al. 2025; Askirka et al. 2025; Memon et al. 2025). As their size goes down, the band gap increases, which induces a shift in the absorption and emission spectra (Alnemrat et al. 2014). This results in the emission of light at different wavelengths (colors) based on the quantum dot size. The electronic and optical properties of CdSe quantum dots are governed by the quantum confinement effect, where the motion of electrons and holes is restricted in all three spatial dimensions, leading to discrete energy levels (Shabaev et al. 2012). This gives rise to unique optical phenomena like fluorescence and tunable emission, which can be adjusted by altering the size of the dots.

CdSe quantum dots often have a high quantum yield and photoluminescence efficiency, which makes them excellent for light-emitting applications such as displays and sensors (Magaryan et al. 2016; Silva 2014; Zhang et al. 2024a). CdSe quantum dots exhibit tunable absorption and emission spectra, which can be fine-tuned by adjusting their size during synthesis. This makes them versatile for various applications.

Tuning the optical properties of CdSe QDs through uniaxial compression is a fascinating approach that leverages mechanical stress to induce changes in the electronic and optical behavior of these nanomaterials (Gong et al. 2016; Pisheh et al. 2017; Rodríguez-Magdaleno et al. 2022). Size-dependent band

gap behavior means that applying strain can effectively tune the frontier states of the quantum dots, leading to changes in their absorption and emission spectra. Strain can alter the electronic band structure, i. e. degeneracy, polarization, and band gap value by affecting the overlap of electron and hole wavefunctions in the QDs. This modification changes the exciton binding energy, which is the energy required to separate the electron–hole pair.

Compressive strain can also induce changes in the valence band and conduction band alignment and localization, modifying the optical absorption spectrum (Rodríguez-Magdaleno et al. 2022). The application of uniaxial strain can shift the absorption edge (onset of absorption) to different energies based on strain direction, magnitude, and quantum dot shape. This will result in a change in the wavelengths at which QDs absorb light. The fluorescence emission spectrum may be red-shifted or blue-shifted depending on the specific strain applied. Compressing QDs along a certain axis, for example, might reduce the band gap, causing a red shift in the emission.

Computational section

The electronic structure calculations of low-dimensional crystalline lattices were performed using Vienna Ab-initio Simulation Package (VASP) (Kresse, Furthmüller 1996; Kresse, Hafner 1993; 1994; Kresse, Joubert 1999) within Density Functional Theory (DFT) (Kohn, Sham 1965). A plane-wave basis set coupled with the projector augmented wave (PAW) method (Blöchl 1994; Kresse et al. 1999), GGA-PBE (Perdew et al. 1996) functional, and Grimme D3 correction (Grimme 2006) for van-der-Waals interaction were used in the study. Optimization and single point calculations were made only at Γ point due to an absence of periodicity. For all elements involved in the electronic structure calculations, PAW potentials were used. Twelve and six outer electrons were treated as valence electrons for cadmium and selenium respectively. A vacuum interval of 20 Å was set along 3 axes to avoid artificial interactions between adjacent unit cell images. In all calculations, the cut-off energy was equal to 500 eV. During optimization, the maximum force acting on atoms less than 0.001 eV/Å was used as a stopping criterion for structural minimization.

The Purcell factor calculations were performed using the Finite Difference Time Domain (FDTD) method. Three independent orthogonally-oriented dipole sources were placed at the center of the nanoparticle. For each dipole, the Purcell factor was calculated as the ratio between the power radiated in the environment with a nanoparticle and the power radiated in free space. After three independent calculations for orthogonal sources, the final Purcell factor was averaged.

Results

The optimization procedure involved refining the atomic positions to minimize residual forces. Bulk CdSe crystals in both the wurtzite and zinc blende phases were obtained from the Crystallography Open Database and optimized using periodic boundary conditions (PBC) within Density Functional Theory (DFT). Subsequently, spherical regions with a radius of 8 Å were extracted from the bulk (see Fig. 1). These regions were then further optimized to adjust the atomic coordinates and correct for any dangling bonds at the surface.

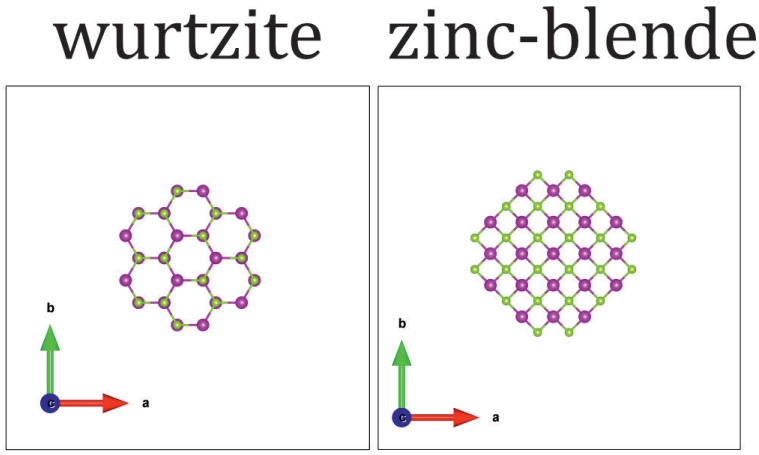

Fig. 1. Structure of wurtzite and zinc-blende CdSe quantum dots. Cd and Se atoms are shown in purple and green respectively

The optimized structure of the wurtzite CdSe quantum dot is illustrated in Fig. 2. The outer shell, which consisted of both Cd and Se atoms, was subjected to relaxation during the optimization procedure. Thus, reduction of symmetry to the C1 point group is an expected result due to the formation of dangling bonds with the following outer shell relaxation; nevertheless, the quantum dot retains its spherical shape, thereby confirming its structural stability.

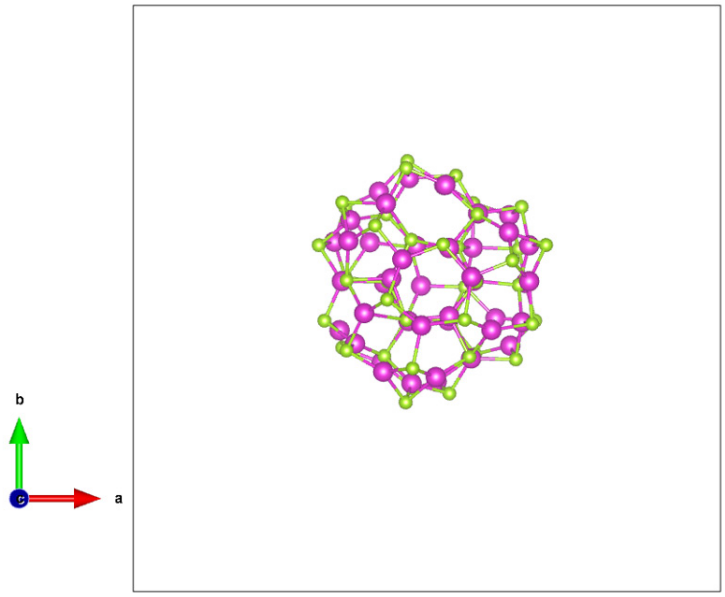

Fig. 2. Structure of the optimized wurtzite CdSe quantum dots. Cd and Se atoms are shown in purple and green respectively

The electronic properties of spherical wurtzite CdSe were investigated using both pure and hybrid functionals, specifically PBE and HSE06 (Fig. 3). Both computational approaches indicated the semiconducting nature of the material; however, the HSE06 calculations predicted a band gap approximately twice as large (2.17 eV) as the value obtained from the PBE functional (1.15 eV). While pure functionals are known to generally underestimate band gap values, the shapes of the density of states (DOS) peaks were found to be accurately reproduced, making them suitable for tracking general patterns in the system.

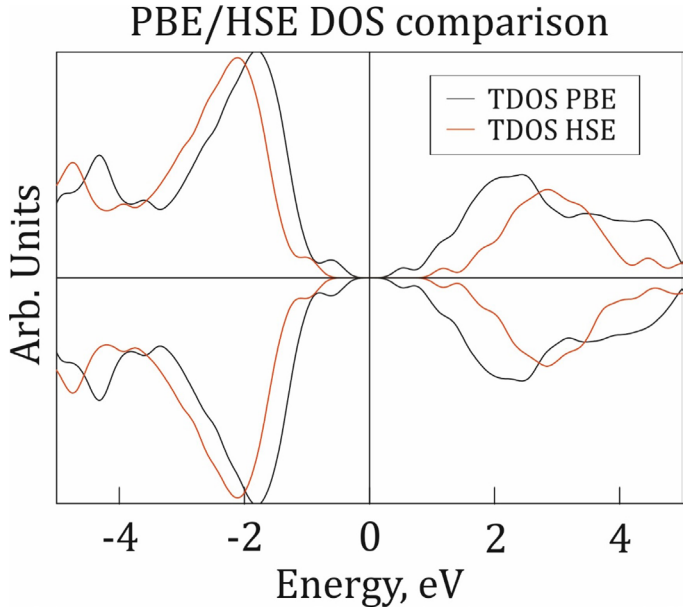

Fig. 3. Density of the states of wurtzite CdSe quantum dots calculated by PBE (black lines) and HSE06 (red lines) functionals. Fermi level assigned to 0 eV

 https://www.doi.org/10.33910/2687-153X-2025-6-2-104-109

Axial compression and extension were then examined. Two additional structures, each with a 10% deformation, were created and optimized, as shown in Fig. 4. The extended CdSe quantum dot was generated by extension along the *xy*-plane, while the compressed CdSe quantum dot was formed by compression in the *xy*-plane. Despite these deformations, the symmetry of the quantum dots remained C1 and was preserved throughout the optimization process.

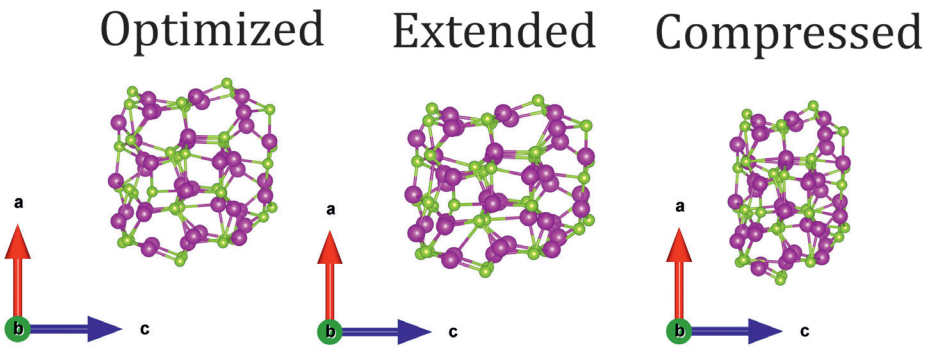

Fig. 4. Optimized, extended and compressed wurtzite CdSe quantum dots. Cd and Se atoms are shown in purple and green respectively

The impact of axial deformations of DOS was examined further. DOS calculations (Fig. 5) demonstrated the shift of the occupied states closer to the Fermi level and no change in the band gap value. The QD extension would lead to a shift of vacant states lower to the Fermi level contrary to the compression case. The distorted structure can be characterized by diffuse localization of states around –2 and 2 eV in comparison with the pristine model.

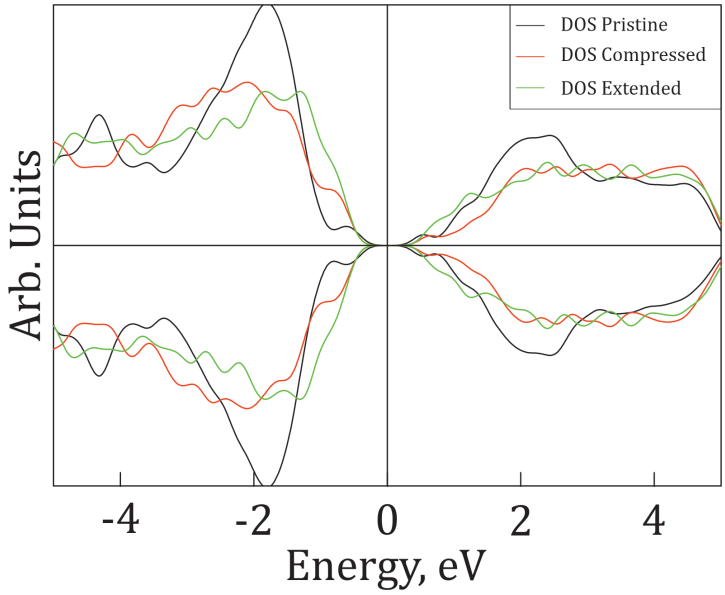

Fig. 5. Total density of states (TDOS) of pristine, compressed, and extended CdSe QDs. TDOS of the pristine lattice is shown with black curves, with TDOS of compressed and extended CdSe QDs marked with red and green curves respectively

To proceed further, we evaluate the Purcell effect spectra under the deformation parameter. In the Finite Difference Time Domain, we simulate an ellipsoid particle with a major axis radius R_{major} = 8 Å and a different minor axis R_{minor} changing from $0.9R_{major}$ to R_{major}. We placed at the center three orthogonal dipole sources and the average final factor and calculated the average final factor.

Fig. 6 shows the average Purcell effect for zinc-blende (left) and wurtzite (right) phases of the CdSe. For the wurtzite phase, we observe a monotonically increased Purcell factor with an increased wavelength. A similar pattern can be also observed in the zinc-blende phase. Besides, the cubic phase shows a narrow

peak at a wavelength of 580 nm. The impact of axial deformation was examined. The Purcell factor for both phases showed stability of the properties under a 10% deformation.

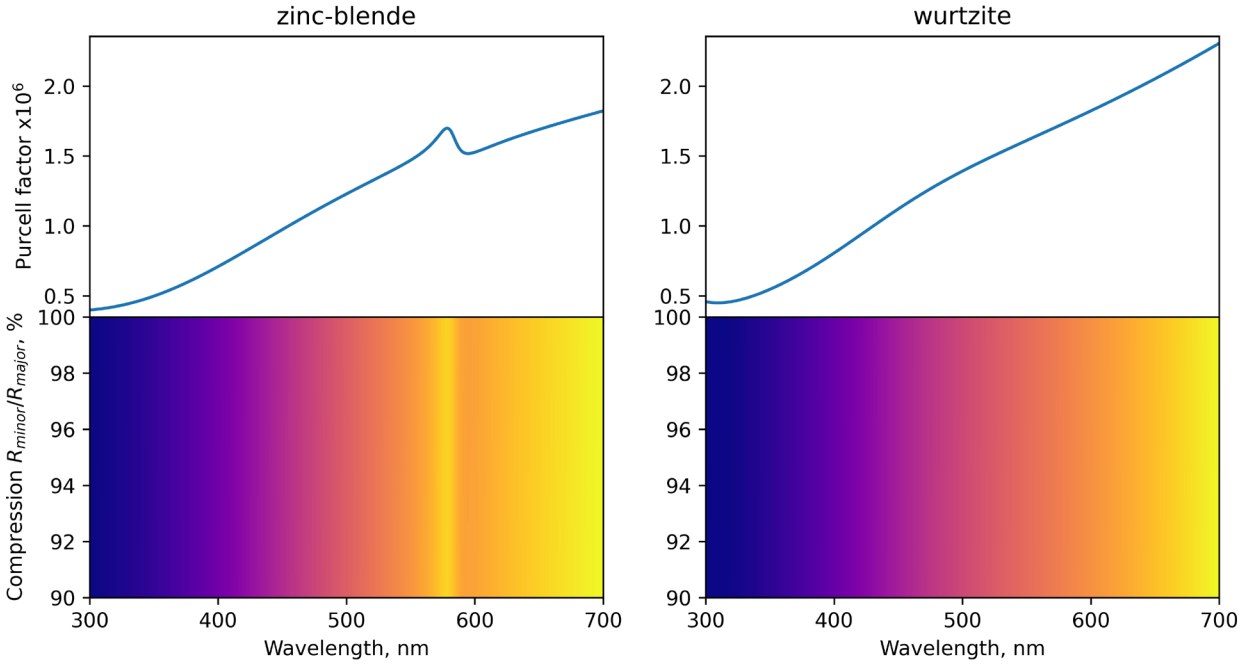

Fig. 6. Purcell factor of CdSe QDs with compression dependence

Conclusions

This paper analyzed and discussed the impact of extension and compression of the CdSe quantum dot of zinc blende and wurtzite phases. We found that for small-sized CdSe QDs, the strain and compression effect do not lead to conductivity properties and a band gap decrease. Theoretical modelling predicts the stability of the 1.6 Angstrom QD and its semiconductor properties with a band gap of about 2eV. Designed quantum dots demonstrate mechanical and optical stability, their properties retained under uniaxial compression.

Conflict of Interest

The authors declare that there is no conflict of interest, either existing or potential.

Author Contributions

Yu. Melchakova: DFT calculations and modelling, manuscript writing, conceptualization.
A. Solomonov: FDTD calculations and modelling, manuscript writing.

Acknowledgements

The authors would like to extend their gratitude to Professor Anna Rodina for her significant contribution to the conceptualization of the manuscript and fruitful discussions throughout the research.

Yu. M. expresses gratitude to Information Technology Centre, Novosibirsk State University, for providing access to a supercomputer and expresses gratitude to ITMO Fellowship program for the financial support.

References

Alnemrat, S., Park, Y. H., Vasiliev, I. (2014) Ab initio study of ZnSe and CdTe semiconductor quantum dots. *Physica E: Low-dimensional Systems and Nanostructures*, 57, 96–102. https://doi.org/10.1016/j.physe.2013.10.037 (In English)

Alsalme, A., Eltawil, M. A., Alsaeedi, H. et al. (2025) Enhancing the photocatalytic efficiency of g-C3N4 by sonochemical dispersion of CdSe quantum dots for photocatalytic degradation of industrial organic pollutants under commercial light source. *Materials Chemistry and Physics*, 334, article 130367. https://doi.org/10.1016/j.matchemphys.2025.130367 (In English)

Askirka, V., Stsiapura, V., Miluski, P. (2025) Efficient FRET in new co-doped Tb(tmhd)3-CdSe/ZnS quantum dots-poly (methyl methacrylate) polymer nanocomposites for optoelectronic and sensor applications. *Journal of Luminescence*, 279, article 121047. https://doi.org/10.1016/j.jlumin.2024.121047 (In English)

Blöchl, P. E. (1994) Projector augmented-wave method. *Physical Review B*, 50 (4), 17953–17979. https://doi.org/10.1103/PhysRevB.50.17953 (In English)

Gong, K., Beane, G., Kelley, D. F. (2016) Strain release in metastable CdSe/CdS quantum dots. *Chemical Physics*, 471, 18–23. https://doi.org/10.1016/j.chemphys.2015.09.009 (In English)

Grimme, S. (2006) Semiempirical GGA-type density functional constructed with a long-range dispersion correction. *Journal of Computational Chemistry*, 27 (15), 1787–1799. https://doi.org/10.1002/jcc.20495 (In English)

Huang, X., Li, N., Kim, K-H., Chang, Q. et al. (2024) Enhancing luminescence efficiency of CdSe quantum dots through the amine-assisted Z-type ligand. *Cell Reports Physical Science*, 5 (11), article 102268. https://doi.org/10.1016/j.xcrp.2024.102268 (In English)

Kohn, W., Sham, L. J. (1965) Self-consistent equations including exchange and correlation effects. *Physical Review B*, 140 (4A), A1133–A1138. https://doi.org/10.1103/PhysRev.140.A1133 (In English)

Kolobkova, E. V., Nikonorov, N. V., Kuznetsova, M. S., Bataev, M. N. (2024) Controlling the luminescence of CdSe quantum dots in the fluorinephosphate glass. *Journal of Non-Crystalline Solids*, 646, article 123248. https://doi.org/10.1016/j.jnoncrysol.2024.123248 (In English)

Kresse, G., Furthmüller, J. (1996) Efficient iterative schemes for ab initio total-energy calculations using a plane-wave basis set. *Physical Review B*, 54 (16), 11169–11186. https://doi.org/10.1103/PhysRevB.54.11169 (In English)

Kresse, G., Hafner, J. (1993) Ab initio molecular dynamics for liquid metals. *Physical Review B*, 47 (1), 558–561. https://doi.org/10.1103/PhysRevB.47.558 (In English)

Kresse, G., Hafner, J. (1994) Ab initio molecular-dynamics simulation of the liquid-metal–amorphous-semiconductor transition in germanium. *Physical Review B*, 49 (20), 14251–14269. https://doi.org/10.1103/PhysRevB.49.14251 (In English)

Kresse, G., Joubert, D. (1999) From ultrasoft pseudopotentials to the projector augmented-wave method. *Physical Review B*, 59 (3), 1758–1775. https://doi.org/10.1103/PhysRevB.59.1758 (In English)

Magaryan, K. A. Mikhailov, M. A., Karimullin, K. R. et al. (2016) Spatially-resolved luminescence spectroscopy of CdSe quantum dots synthesized in ionic liquid crystal matrices. *Journal of Luminescence*, 169, 799–803. https://doi.org/10.1016/j.jlumin.2015.08.064 (In English)

Memon, R., Shaheen, I., Qureshi, A., Niazi, J. H. (2024) Enhanced detection of cardiac troponin-I using CdSe/CdS/ZnS core-shell quantum dot/TiO2 heterostructure photoelectrochemical sensor. *Journal of Alloys and Compounds*, 1008, article 176592. https://doi.org/10.1016/j.jallcom.2024.176592 (In English)

Perdew, J. P., Burke, K., Ernzerhof, M. (1996) Generalized gradient approximation made simple. *Physical Review Letters*, 77 (18), 3865–3868. https://doi.org/10.1103/PhysRevLett.77.3865 (In English)

Pisheh, H. S., Gheshlaghi, N., Ünlü, H. (2017) The effects of strain and spacer layer in CdSe/CdS/ZnS and CdSe/ZnS/CdS core/shell quantum dots. *Physica E: Low-dimensional Systems and Nanostructures*, 85, 334–339. https://doi.org/10.1016/j.physe.2016.07.007 (In English)

Rodríguez-Magdaleno, K. A., Pérez-Álvarez, R., Ungan, F., Martínez-Orozco, J. C. (2022) Strain effect on the intraband absorption coefficient for spherical CdSe/CdS/ZnSe core–shell–shell quantum dots. *Materials Science in Semiconductor Processing*, 141, article 106400. https://doi.org/10.1016/j.mssp.2021.106400 (In English)

Shabaev, A., Rodina, A. V., Efros, A. L. (2012) Fine structure of the band-edge excitons and trions in CdSe/CdS core/shell nanocrystals. *Physical Review B*, 86 (20), article 205311. https://doi.org/10.1103/PhysRevB.86.205311 (In English)

Silva, A. C. A., Vieira de Deus, S. L., Silva, M. J. B, Dantas, N. O. (2014) Highly stable luminescence of CdSe magic-sized quantum dots in HeLa cells. *Sensors and Actuators B: Chemical*, 191, 108–114. https://doi.org/10.1016/j.snb.2013.09.063 (In English)

Zhang, Y., Shida, L., Yanshen, Z. et al. (2024b) Promoting photoelectric performance through extraction of hot electron from Cu-doped CdSe quantum dots. *Journal of Alloys and Compounds*, 1005, article 176037. https://doi.org/10.1016/j.jallcom.2024.176037 (In English)

Zhang, Y., Wenchao, L., Like, L. (2024a) Optical fiber fluorescence Cu2+ sensing technology based on CdSe/ZnS quantum dots: Large detection range, low detection limit. *Analytica Chimica Acta*, 1331, article 343300. https://doi.org/10.1016/j.aca.2024.343300 (In English)

Theoretical physics.
Theory of magnetic properties of solids

UDC 537.611.2

EDN WCYYUP
https://www.doi.org/10.33910/2687-153X-2025-6-2-110-115

Theoretical and experimental discovery of the magnetic monopole and magnetic charge

I. P. Popov ✉[1]

[1] Kurgan State University, 63/4 Sovetskaya Str., Kurgan 640020, Russia

Author

Igor P. Popov, ORCID: 0000-0001-8683-0387, e-mail: ip.popow@yandex.ru

For citation: Popov, I. P. (2025) Theoretical and experimental discovery of the magnetic monopole and magnetic charge. *Physics of Complex Systems*, 6 (2), 110–115. https://www.doi.org/10.33910/2687-153X-2025-6-2-110-115 EDN WCYYUP

Received 9 March 2025; reviewed 19 March 2025; accepted 19 March 2025.

Funding: The study did not receive any external funding.

Abstract. This paper shows that magnetic monopoles and charges exist, inter alia, in solids and cosmic rays, which include electric charges. The magnetic charge, like the electric and the gravitational one, is located in the numerator of the formula for the force of magnetic interaction. Thus, the magnetic charge is equal to $I\mathbf{dl}$. It is this value that creates the force (magnetic) field, interacts with other similar values and, therefore, in accordance with the definition given above, is the magnetic charge. Universal representation is $q\mathbf{v}$. Its universality lies in the fact that it is suitable for individual particles, including cosmic rays, which include electric charges.

Keywords: magnetic monopole, magnetic charge, electric charge, gravitational charge, electron

Introduction

Attempts to obtain a magnetic monopole by cutting a magnet into two parts have failed so far. Magnetic monopoles have not been found in space, ores, meteorites, lunar soil, experiments at the Large Hadron Collider, or anywhere at all.

Abstract models of the magnetic monopole of Dirac, Hooft — Polyakov, Urutskoev, and others have remained such and have not been found in nature.

At the same time, magnetic monopoles and charges exist, among other things, in solid bodies and cosmic rays, which include electric charges.

The purpose of this work is to detect them.

To do this, we just need to take a look at other charges.

Preliminary remarks on relationship between the magnetic charge and the electric charge

Theorem. The magnetic charge is proportional to the electric charge and the speed of its movement.

Proof.

1). The electric charge q is INSEPARABLY connected with the electric field.

2). The electric field strength $\mathbf{E}$ is proportional to the magnitude of the electric charge q, i. e. $E = k_1 q$.

3). The magnetic charge μ is INSEPARABLY connected with the magnetic field.

4). The magnetic field strength $\mathbf{H}$ is proportional to the magnitude of the magnetic charge μ, i. e. $H = k_2 \mu$.

When an electric charge moves at a speed **v**, a magnetic field arises, the strength of which is equal to

$$\mathbf{H} = \varepsilon_0[\mathbf{v}, \mathbf{E}] \ ,$$

where e_0 is the electric constant.

In accordance with 2) and 4),

$$\frac{\mathbf{H}}{H} k_2 \mu = \varepsilon_0 \left[\mathbf{v}, \frac{\mathbf{E}}{E} k_1 q \right] .$$

The theorem is proved.

Corollary 1. The velocity **v** depends on the choice of the reference frame. Therefore, both the magnetic field and the magnetic charge also depend on the choice of the reference frame (they are not invariant).

Corollary 2. At **v** = 0, the magnetic field cannot exist. Therefore, in accordance with 3), the magnetic charge cannot exist either.

Remark 1. The idea that the magnetic charge is a fundamental characteristic of a particle and does not depend on the choice of the reference frame in accordance with 3) is equivalent to the idea that the magnetic field does not depend on the choice of the reference frame (unreliable idea).

Remark 2. The common view of a permanent magnet (magnetic dipole) as a static object ignores the motion of electrons in it. If these motions, including spin ones, are hypothetically stopped, the magnetic dipole will cease to exist.

Remark 3. A magnetic monopole is not the only physical object that cannot exist at zero velocity. Another one is the photon, the existence of which is unquestioned.

Remark 4: Opponents may point out that the dependence of the magnetic charge on velocity may indicate that it is not a conserved quantity. However, this argument does not discredit the idea of the magnetic charge, since the electric charge is not always conserved either — for example, in the annihilation of an electron and a positron.

A note on Dirac's magnetic charge

It is equal to the following:

$$g = \frac{n\hbar c}{2e} \ .$$

The fine structure constant is

$$\alpha = \frac{e^2}{4\pi\hbar}\sqrt{\frac{\mu_0}{\varepsilon_0}} \ .$$

$$\hbar = \frac{e^2}{4\pi\alpha}\sqrt{\frac{\mu_0}{\varepsilon_0}} \ .$$

$$g = \frac{n\hbar c}{2e} = \frac{nc}{2e}\frac{e^2}{4\pi\alpha}\sqrt{\frac{\mu_0}{\varepsilon_0}} = \frac{nce}{8\pi\alpha} Z_0 \ .$$

Z_0 is the impedance of free space.

The dimension of the Dirac magnetic charge includes the electric charge and velocity, which does not contradict the theorem proved above.

Finding a magnetic charge

A charge is a physical object that creates a force field and interacts with other charges of the same physical nature (Demidov 2022; Gorokhovatsky et al. 2022; Kononov et al. 2020).

The electric charge (q_1, q_2) (Aslyamova, Gavrilov 2020; Pronin, Khinich 2020) is located in the numerator of the formula for the force of interaction of electric charges

$$\mathbf{F}_{12} = \pm \frac{1}{4\pi\varepsilon_0 \varepsilon} \frac{q_1 q_2}{r_{12}^3} \mathbf{r}_{12} ,$$

where e is relative permittivity and $\mathbf{r}_{12}$ is the radius vector.

The gravitational charge (m_1, m_2) (Vertogradov 2023) is located in the numerator of the formula for the force of gravitational interaction

$$\mathbf{F}_{12} = -G \frac{m_1 m_2}{r_{12}^3} \mathbf{r}_{12} ,$$

where G is the gravitational constant.

The magnetic charge, like the electric and the gravitational one, is located in the numerator of the formula for the force of magnetic interaction (Popov 2024)

$$d\mathbf{F}_{12} = -\frac{\mu_0 \mu}{4\pi} \frac{\left(I_1 d\mathbf{l}_1, I_2 d\mathbf{l}_2\right)}{r_{12}^3} \mathbf{r}_{12} , \quad (1)$$

where μ_0 is the magnetic constant, μ is relative magnetic permeability, I_1, I_2 are the electric currents in the conductors, and $d\mathbf{l}_1$, $d\mathbf{l}_2$ are the elements of the interacting conductors with the currents.

A similar formula was obtained by Ampere (Ampere 1954).

Thus, the magnetic charge is equal to

$$d\boldsymbol{\mu} = Id\mathbf{l} . \quad (2)$$

It is this quantity that creates a force (magnetic) field, interacts with other similar quantities, and, therefore, is a magnetic charge according to the definition given above.

Universal representation is

$$d\boldsymbol{\mu} = Id\mathbf{l} = \frac{dq}{dt} d\mathbf{l} = \frac{d\mathbf{l}}{dt} dq = \mathbf{v} dq .$$

$$\boldsymbol{\mu} = q\mathbf{v} , \quad (3)$$

where $\mathbf{v}$ is the velocity of the electric charge.

Its versatility lies in the fact that it is suitable for individual particles (Pavlov 2024; Pavlov 2025), including cosmic rays, which include electric charges.

For an electron:

$$\boldsymbol{\mu}_e = -e\mathbf{v} , \quad (4)$$

where e is the charge of the electron.

As a consequence, the Lorentz force is equal to

$$\mathbf{F}_L = \left[\boldsymbol{\mu}, \mathbf{B}\right] ,$$

where $\mathbf{B}$ is magnetic induction.

 https://www.doi.org/10.33910/2687-153X-2025-6-2-110-115

Qualitative representation of the magnetic interaction force

A rigorous derivation of formula (1) is beyond the scope of this discussion, but its fundamental structure can be verified by the following reasoning.

There are two parallel elements of conductors with currents (magnetic monopoles with charges $I_1 d\mathbf{l}_1$ and $I_2 d\mathbf{l}_2$) (Fig. 1).

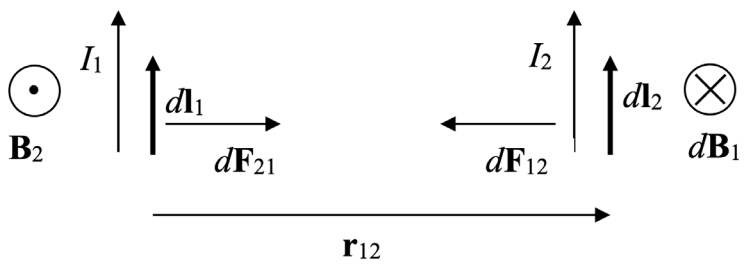

Fig. 1. Interaction of magnetic monopoles

The magnetic charge $I_1 d\mathbf{l}_1$ creates a magnetic field with induction at the location of the magnetic charge $I_2 d\mathbf{l}_2$

$$d\mathbf{B}_1 = \frac{\mu_0 \mu}{4\pi r_{12}^3} I_1 \left[d\mathbf{l}_1, \mathbf{r}_{12} \right] .$$

The force acting on the second charge from the magnetic field is equal to

$$d\mathbf{F}_{12} = I_2 \left[d\mathbf{l}_2, d\mathbf{B}_1 \right] =$$

$$= \frac{\mu_0 \mu I_1 I_2}{4\pi r_{12}^3} \left[d\mathbf{l}_2, \left[d\mathbf{l}_1, \mathbf{r}_{12} \right] \right] = -\frac{\mu_0 \mu}{4\pi} \frac{\left(I_1 d\mathbf{l}_1, I_2 d\mathbf{l}_2 \right)}{r_{12}^3} \mathbf{r}_{12} . \tag{5}$$

On Newton's third law and Ampere's law

Theoretical magnetostatics does not satisfy Newton's third law (Fig. 2).

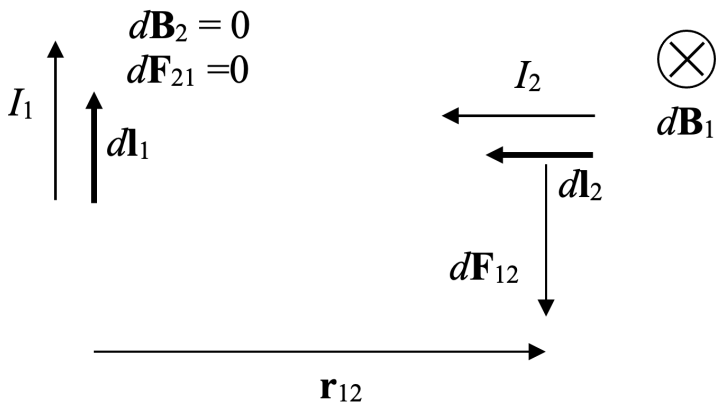

Fig. 2. Violation of Newton's third law

Indeed,

$$d\mathbf{F}_{12} = I_2\left[d\mathbf{l}_2, d\mathbf{B}_1\right] = \frac{\mu_0\mu I_1 I_2}{4\pi r_{12}^3}\left[d\mathbf{l}_2, \left[d\mathbf{l}_1, \mathbf{r}_{12}\right]\right] \neq 0 \ ,$$

$$d\mathbf{F}_{21} = I_1\left[d\mathbf{l}_1, d\mathbf{B}_2\right] = \frac{\mu_0\mu I_1 I_2}{4\pi r_{12}^3}\left[d\mathbf{l}_1, \left[d\mathbf{l}_2, \mathbf{r}_{12}\right]\right] = 0 \ .$$

Here

$$\left[d\mathbf{l}_2, \mathbf{r}_{12}\right] = 0 \ ,$$

since the vectors are collinear.

The contradiction with Newton's third law has the following justification: current elements are not independent objects, while Newton's third law is observed for closed electric circuits.

However, such justification is not convincing, since not all electric currents are closed. Among the examples of such currents are cosmic rays, which include electric charges.

Based on expression (1), magnetostatics is completely consistent with Newton's third law, which it unconditionally satisfies. (Popov 2024).

Remark 1. Ampere constructed magnetostatics on the basis of an expression similar to (1) (his formula differed only in the dimensionless coefficient) and declared the necessity of fulfilling Newton's third law (Ampere 1954).

Remark 2. Expression (5) is not Ampere's law. He does not have a single expression resembling this formula (Ampere 1954).

Conclusion

The discovered magnetic monopoles (2)–(4) have nothing in common with the monopoles of Dirac, Hooft–Polyakov, Urutskoev, etc. At the same time, the monopoles of Dirac, Hooft–Polyakov, Urutskoev, etc. do not exist in nature. However, monopoles (2)–(4) exist wherever there are moving electric charges, i. e., practically everywhere. They particularly determine the magnetic properties of solids and are present in cosmic rays, which include electric charges.

The theoretical value of this work lies in that the discovery of magnetic monopoles and magnetic charges improves the formal symmetry of electrodynamics, the violation of which has often concerned many specialists.

The practical contribution of the study is that the overwhelming majority of processes in electrical systems are determined by magnetic charges.

Conflict of Interest

The author declares that there is no conflict of interest, either existing or potential.

References

Ampere, A. M. (1954) *Elektrodinamika [Electrodynamics]*. Moscow: USSR Academy of Sciences Publ., 492 p. (In Russian)

Aslyamova, I. N., Gavrilov, S. P. (2020) Characteristics of high-frequency emission of an electron in graphene in a constant electric field. *Physics of Complex Systems*, 1 (2), 78–84. https://doi.org/10.33910/2687-153X-2020-1-2-78-84 (In English)

Demidov, E. V. (2022) Extrema positions of charge carrier band spectrum in thin bismuth films. *Physics of Complex Systems*, 3 (4), 154–158. https://doi.org/10.33910/2687-153X-2022-3-4-154-158 (In English)

Gorokhovatsky, Yu. A., Sotova, Yu. I., Temnov, D. E. (2022) A study of charge relaxation in corona electrets based on P(VDF-TFE) copolymer. *Physics of Complex Systems*, 3 (3), 104–108. https://doi.org/10.33910/2687-153X-2022-3-3-104-108 (In English)

Kononov, A. A., Castro Arata, R. A., Nikonorova, N. N. (2020) Effect of quasi-stationary electric field on charge transfer in poly(phenylene oxide) based composites. *Physics of Complex Systems*, 1 (2), 52–55. https://doi.org/10.33910/2687-153X-2020-1-2-52-55 (In English)

Pavlov, V. D (2024) O momente impul'sa kuperovskoj pary elektronov i kvante magnitnogo potoka [On the angular momentum of a Cooper pair of electrons and a quantum of magnetic flux]. *Prikladnaya fizika i matematika — Applied Physics and Mathematics*, 4, 12–16. http://dx.doi.org/10.25791/pfim.04.2024.1301 (In Russian)

Pavlov, V. D. (2025) On the electronic quantum structures of conductors. *Physics of Complex Systems*, 6 (1), 49–53. https://www.doi.org/10.33910/2687-153X-2025-6-1-49-53 (In English)

Popov, I. P. (2024) Combined vectors and magnetic charge. *Technical Physics*, 69 (8), 2397–2405. https://doi.org/10.1134/S1063784224700415 (In English)

Pronin, V. P., Khinich, I. I. (2020) Characteristic energy loss of electrons in mg with angle resolution. *Physics of Complex Systems*, 1 (1), 4–9. https://doi.org/10.33910/2687-153X-2020-1-1-4-9 (In English)

Vertogradov, V. D. (2023) On particle collisions during gravitational collapse of vaidya spacetimes. *Physics of Complex Systems*, 4 (1), 17–23. https://doi.org/10.33910/2687-153X-2022-4-1-17-23 (In English)

Summaries in Russian / Информация о статьях на русском языке

Физика конденсированного состояния

ВЛИЯНИЕ КАЛЬЦИЯ НА КОЭФФИЦИЕНТ НЕРНСТА — ЭТТИНГСГАУЗЕНА В СИСТЕМЕ $Y_{1-x}Ca_xBa_2Cu_{2.8}Zn_{0.2}O_y$ С ДВОЙНЫМИ ЗАМЕЩЕНИЯМИ

Чжан Суньпэн, Виталий Эдуардович Гасумянц

Аннотация. Представлены экспериментальные результаты по температурным зависимостям коэффициента Нернста в нормальном состоянии в системе $Y_{1-x}Ca_xBa_2Cu_{2.8}Zn_{0.2}O_y$, которые количественно проанализированы в рамках модели узкой зоны совместно с температурными зависимостями коэффициента термоЭДС. На основе проведенного анализа получены данные о подвижности носителей заряда во всех исследованных образцах, а затем проанализировано изменение ее значения с увеличением содержания кальция. Показано, что все экспериментальные и расчетные результаты можно объяснить, если учесть, что как кальций, так и цинк непосредственно воздействуют на структуру зоны, ответственной за проводимость в системе $YBa_2Cu_3O_y$. Введенный в решетку кальций компенсирует локальные нарушения электронной структуры, возникшие в результате легирования цинком, в результате чего параметры нормального состояния при $x \geq 0.125$ становятся близкими к значениям, характерным для нелегированного $YBa_2Cu_3O_y$.

Ключевые слова: иттриевые ВТСП, легирование, коэффициент Нернста — Эттингсгаузена, модель узкой зоны, энергетический спектр, подвижность носителей заряда

Для цитирования: Xunpeng, Zh., Gasumyants, V. E. (2025) Calcium effect on the Nernst coefficient in double-substituted $Y_{1-x}Ca_xBa_2Cu_{2.8}Zn_{0.2}O_y$. *Physics of Complex Systems*, 6 (2), 59–68. https://www.doi.org/10.33910/2687-153X-2025-6-2-59-68 EDN VPUHLM

ДИЭЛЕКТРИЧЕСКАЯ СПЕКТРОСКОПИЯ 10-ПРОЦЕНТНОГО РАСТВОРА ИММУНОГЛОБУЛИНА G ЧЕЛОВЕКА ПРИ ФИЗИОЛОГИЧЕСКИХ ТЕМПЕРАТУРАХ. ЧАСТЬ 1

Жанна Андреевна Сальникова, Александр Павлович Смирнов, Рене Алехандро Кастро Арата

Аннотация. Исследованы диэлектрические и релаксационные свойства 10-процентного водного раствора иммуноглобулина человека в частотном диапазоне 0.1 Гц – 15 МГц при температурах 35–39,7 °С. На частотных зависимостях фактора диэлектрических потерь ε" обнаружено три максимума в областях дисперсии ε', которые были аппроксимированы уравнением Гаврильяка — Негами. Для каждого процесса рассчитаны релаксационные параметры α, β, τ_0 при различных температурах и построены функции распределения времен релаксаторов G(τ). В работе сделаны предположения о возможных кинетических единицах данных процессов и возможных фазовых переходах в них.

Ключевые слова: диэлектрическая проницаемость иммуноглобулина G, диэлектрические потери IgG, релаксационные параметры IgG, уравнение Гаврильяка — Негами, фазовые переходы, глобула-клубок, иммуноглобулины

Для цитирования: Salnikova, Zh. A., Smirnov, A. P., Castro Arata, R. A. (2025) Dielectric spectroscopy of a 10% solution of human immunoglobulin G at physiological temperatures. Part 1. *Physics of Complex Systems*, 6 (2), 69–86. https://www.doi.org/10.33910/2687-153X-2025-6-2-69-86 EDN VSUTSU

Физика полупроводников

ЛАЗЕРНАЯ МОДИФИКАЦИЯ ХАЛЬКОГЕНИДНЫХ ПЛЕНОК PbSe С ФОРМИРОВАНИЕМ ЛИППС

Артур Джуракулович Долгополов, Анастасия Александровна Ольхова, Максим Михайлович Сергеев, Павел Петрович Омельченко, Богдан Геннадьевич Шульга, Михаил Константинович Москвин, Алина Александровна Патрикеева, Владислав Романович Гресько

Аннотация. Исследуется лазерная модификация халькогенидных пленок селенида свинца (PbSe) с формированием лазерно-индуцированных периодических поверхностных структур (ЛИППС). Такие модификации важны для повышения чувствительности газоанализаторов,

для обнаружения опасных газов в различных отраслях промышленности. Использование наносекундных лазерных импульсов для обработки пленок обеспечивает более высокую производительность, лучшую воспроизводимость и больший контроль над оптическими свойствами по сравнению с традиционными методами печного отжига. Формирование ЛИППС при определенных условиях лазерного облучения приводит к изменению оптических характеристик пленки, в том числе к увеличению поглощения в инфракрасном (ИК) диапазоне. Кроме того, изучена зависимость периодичности структур от плотности мощности лазерного излучения. Полученные результаты подчеркивают потенциал лазерной модификации для создания новых оптических свойств и разработки инновационных устройств фотоники.

Ключевые слова: Пленки PbSe, лазерная модификация, оптические характеристики, наносекундные лазерные импульсы, лазерно-индуцированные периодические поверхностные структуры (ЛИППС)

Для цитирования: Dolgopolov, A. D., Olkhova, A. A., Sergeev, M. M., Omelchenko, P. P., Shulga, B. G., Moskvin, M. K., Patrikeeva, A. A., Gresko, V. R. (2025) Laser modification of PbSe chalcogenide films via LIPSS formation. *Physics of Complex Systems*, 6 (2), 87–92. https://www.doi.org/10.33910/2687-153X-2025-6-2-87-92 EDN QUWZMD

ТЕРМИЧЕСКАЯ И ЛАЗЕРНАЯ КРИСТАЛЛИЗАЦИЯ ТОНКИХ ПЛЕНОК InSe, СФОРМИРОВАННЫХ МЕТОДОМ ВАКУУМНО-ТЕРМИЧЕСКОГО ИСПАРЕНИЯ

Мария Евгеньевна Федянина, Виктория Борисовна Пестова, Дмитрий Валерьевич Пепеляев, Яна Сергеевна Лебедева, Алексей Вальтерович Бабич, Михаил Петрович Смаев, Алексей Валентинович Ромашкин, Сергей Иванович Нестеров, Сергей Александрович Козюхин

Аннотация. Бинарные халькогенидные соединения нашли широкий спектр применения благодаря возможности быстрого и обратимого фазового перехода, перестраиваемой ширины запрещенной зоны, высокой подвижности носителей заряда. Рассматриваются результаты термической и лазерной кристаллизации тонких пленок InSe, сформированных методом вакуумно-термического испарения синтезированного материала и покрытых защитным слоем SiO_2. Аморфное состояние тонких пленок InSe было подтверждено спектроскопией комбинационного рассеяния света. Процессы термической и лазерной кристаллизации были изучены путем измерения электрического сопротивления и с применением оптической микроскопии соответственно. Были получены диапазоны температур и мощностей лазерного воздействия, необходимые для кристаллизации тонкой пленки InSe. Результаты спектроскопии комбинационного рассеяния показали, что степень кристалличности тонких пленок InSe можно подстраивать, варьируя мощность лазерного излучения.

Ключевые слова: халькогенидные материалы, бинарные соединения, InSe, оптические свойства, структурные свойства, лазерная кристаллизация

Для цитирования: Fedyanina, M. E., Pestova, V. B., Pepelyaev, D. V., Lebedeva, Ya. S., Babich, A. V., Smayev, M. P., Romashkin, A. V., Nesterov, S. I., Kozyukhin, S. A. (2025) Thermal and laser crystallization of InSe thin films formed by vacuum thermal evaporation. *Physics of Complex Systems*, 6 (2), 93–103. https://www.doi.org/10.33910/2687-153X-2025-6-2-93-103 EDN MBYUNH

ВЛИЯНИЕ ОДНООСНОГО СЖАТИЯ НА МИКРО- И МАКРОПАРАМЕТРЫ КВАНТОВЫХ ТОЧЕК CdSe РАЗНОГО РАЗМЕРА

Юлия Антоновна Мельчакова, Александр Иванович Соломонов

Аннотация. Смоделированы CdSe квантовые точки в двух фазах: цинковая обманка и вюрцит, а также проанализированы данные DFT расчетов и расчетов фактора Парселла. Квантовые точки с размером 1.6 Å оказались стабильными и были оптимизированы с помощью обменно-корреляционного функционала PBE. Поведение пограничных орбиталей (HOMO, LUMO) исследовано для нерелаксированной структуры с учетом симметрии и вырождения. Результаты определения фактора Парселла квантовых точек в фазах цинковая обманка и вюрцит размером 1,6 Å показали, что они стабильны при одноосном сжатии. Разработанные квантовые точки демонстрируют механическую и оптическую стабильность, а их свойства сохраняются.

Ключевые слова: теория функционала плотности, частная разность во временном домене, квантовые точки, селенид кадмия, вюрцит, сфалерит, электронные свойства, фактор Парселла

Для цитирования: Melchakova, Yu. A., Solomonov, A. I. (2025) The effect of uniaxial compression on micro- and macro-parameters of CdSe quantum dots of different sizes. *Physics of Complex Systems*, 6 (2), 104–109. https://www.doi.org/10.33910/2687-153X-2025-6-2-104-109 EDN WANXEA

Теоретическая физика

ТЕОРЕТИЧЕСКОЕ И ЭКСПЕРИМЕНТАЛЬНОЕ ОТКРЫТИЕ МАГНИТНОГО МОНОПОЛЯ И МАГНИТНОГО ЗАРЯДА

Игорь Павлович Попов

Аннотация. Показано, что магнитные монополи и заряды существуют в том числе и в твердых телах, и в космических лучах, включающих электрические заряды. Магнитный заряд, подобно электрическому и гравитационному, располагается в числителе формулы для силы магнитного взаимодействия. Таким образом, магнитный заряд равен Id**l**. Именно эта величина создает силовое (магнитное) поле и взаимодействует с другими подобными величинами. Таким образом, в соответствии с приведенным выше определением, эта величина является магнитным зарядом. Универсальное представление имеет вид q**v**. Его универсальность состоит в том, что оно подходит, помимо прочего, и для отдельных частиц, в том числе и для космических лучей, включающих электрические заряды.

Ключевые слова: магнитный монополь, магнитный заряд, электрический заряд, гравитационный заряд, электрон

Для цитирования: Popov, I. P. (2025) Theoretical and experimental discovery of the magnetic monopole and magnetic charge. *Physics of Complex Systems*, 6 (2), 110–115. https://www.doi.org/10.33910/2687-153X-2025-6-2-110-115 EDN WCYYUP